Design and Application of Damped Machine Elements

by

Samir A. Nayfeh

B.S., Engineering Science and Mechanics, 1991
M.S., Engineering Mechanics, 1993
Virginia Tech

submitted to the Department of Mechanical Engineering
in partial fulfillment of the requirements for the degree of
Doctor of Philosophy in Mechanical Engineering

at the

Massachusetts Institute of Technology
June 1998

signature of author _____
Department of Mechanical Engineering
29 May 1998

certified by _____
Alexander H. Slocum
Alex & Brit d'Arbeloff Professor of Mechanical Engineering

accepted by _____
Ain A. Sonin
Chairman, Department Committee on Graduate Students

Design and Application of Damped Machine Elements

by

Samir A. Nayfeh

submitted to the Department of Mechanical Engineering
on May 29, 1998 in partial fulfillment of the requirements for the
degree of Doctor of Philosophy in Mechanical Engineering

ABSTRACT

As traverse rates in machine tools have increased, slideways have been largely replaced by rolling-element bearings. Whereas machines with slideways typically exhibit between three and four per cent of critical damping in their lowest few modes of vibration, those with rolling-element bearings typically exhibit less than three per cent. But as rates of operation are pushed ever higher, resonant conditions in machine structures become increasingly difficult to avoid and damping plays a central role in limiting resonant response.

In the present work, basic guidelines for the analysis and design of damping treatments are set forth. Then new mehtods are presented for transverse vibration of linear bearings, longitudinal vibration of leadscrews, and three-dimensional flexural and torsional vibration of beams. Finally, it is shown how the methods developed in this thesis can be used to increase the damping of the lowest two modes of vibration of a wafer-handling robot by roughly four per cent of critical.

Thesis Supervisor: Alexander H. Slocum
Title: Alex and Brit d'Arbeloff Professor of Mechanical Engineering

ACKNOWLEDGMENT

This research was supported by Gary Vrsek, Rodney Tobazinski, and Zafar Shaikh of the Ford Motor Company; Dr. Larry Schuette and David Armoza of the Naval Research Laboratory; Alex d'Arbeloff and George Chamillard of Teradyne; and Papken Der Torossian of Silicon Valley Group.

I could not have completed this work without help from a number of talented members of the MIT community. Among the faculty, I would like to thank Prof. Alexander Slocum for instructing, guiding, aiding, and abetting me in this work; Prof. Sanjay Sarma for urging me on and carefully reading the manuscript; Profs. David Trumper and Stephen Crandall for acutely assessing my progress; and Prof. Haruhiko Asada for advising and supporting me during completion of the chapters on sensitivity analysis. I would also like to thank my colleagues Daniel Braunstein, Mark West, Sepehr Kiani, Ryan Vallance, Stephen Ludwick, Pradeep Subrahmanyan, and Mark Williams for helping to sharpen my knowledge of mechanical design; and Ammar Al-Nahwi, Osameh Rifai, Ghassan Al-Kibsi, and Jalal Khan for their instruction in the dynamics and control of machines, markets, and *kurat al-qadam.*

Most of all, I would like to thank my parents, Ali and Inam Nayfeh, who are my original and most persistent teachers; my brothers, Mahir, Tariq, and Nader, for inspiration and companionship; and my wife, Sherin, for making the present better than the past.

CONTENTS

CHAPTER 1
Introduction

1.1 Background

Among the definitions of "machine" listed in the Webster's Dictionary (1983) is "a device that transmits or modifies force or motion, as a lever or pulley." At first glance, this seems a hopelessly narrow delimitation, but it points to the essential ingredients of anything we would like to think of as a machine: force and motion. Even the most sophisticated CNC milling machine is, at heart, a lever that pushes a cutting tool through a workpiece, and its performance is determined by how well it can impose prescribed motions and forces on the workpiece.

Why Study Damping?

Few machines operate so slowly that the forces involved can be regarded as static, and even such machines are subject to dynamic external disturbances. Even small dynamic forces, if they resonate with a machine, can cause large oscillations or instability. Hence designers have long focused on the avoidance of resonance by manipulation of the stiffness and inertia so as to move the resonant frequencies of a machine away from the frequencies of forces acting upon or within a machine. It is, however, often impractical or impossible to avoid resonance entirely, and if resonance occurs, the damping plays a critical role in maintaining machine performance.

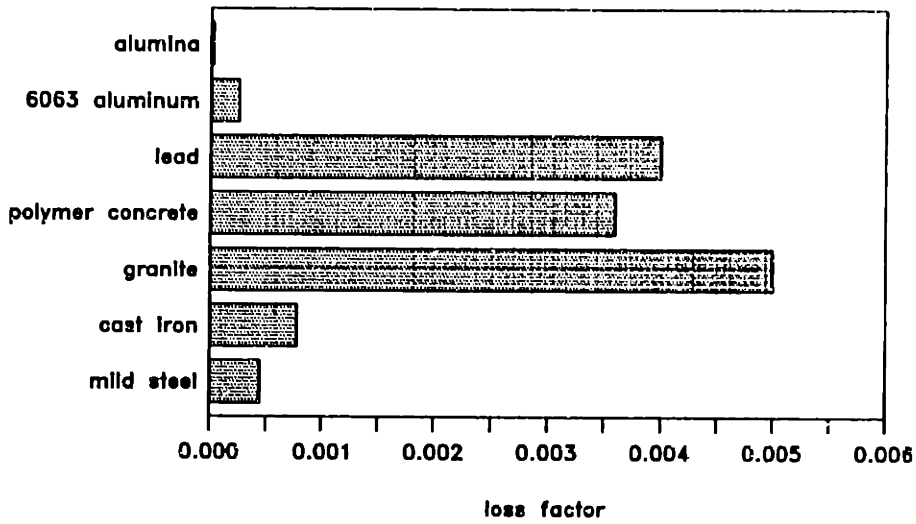

Figure 1.1 Loss factors typical of various structural materials (Lazan, 1968).

Why Add Damping?

Damping in machine structures can arise from a number of physical mechanisms, principally: coupling to viscous flow, transduction to electrical or magnetic fields, material hysteresis, and microslip at material interfaces. Unless introduced deliberately, fluid, electrical, and magnetic dissipation contribute almost nothing to the damping in a machine. Material hysteresis is negligible for most structural materials unless they are deformed beyond the elastic limit (see Fig. 1.1).

Careful measurement of components and assemblies shows that the damping in machines arises almost entirely from rubbing at material interfaces and coupling to ground. An example of such measurements carried out for a lathe in various stages of assembly is shown in Fig. 1.2. The first measurement was taken on the lathe bed alone, and the loss factor of approximately one per cent is mostly due to vibration transmitted to ground through the supports. Successive measurements show that the loss factor increases progressively to about eight per cent as the carriage, spindle stock, and tail stock are assembled to the machine. Most of this damping arises from relative motion in the lubricated slideways.

The damping is usually considerably lighter in machines where rolling-element bearings are used in lieu of slideways. Experience tells us to expect

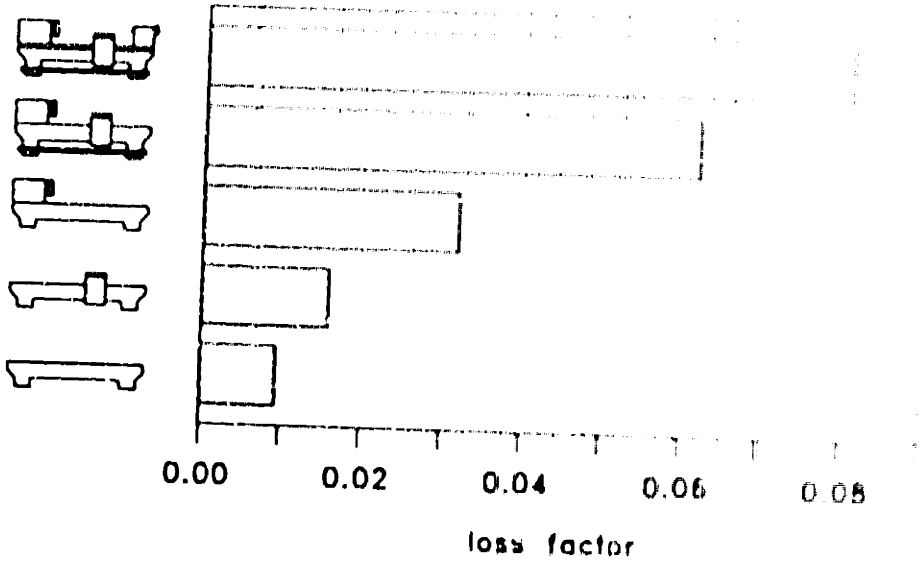

Figure 1.2 Damping in a lathe during various stages of assembly (reported [illegible] as reproduced by Koenigsberger and Tlusty (1970)

loss factors anywhere from 0.5 to 4.0 per cent for the lowest [illegible] machine tool with rolling-element bearings, and that the loss factor [illegible] if the machine is reassembled. While some work has been done to predict the damping at material interfaces (e.g., Crawley *et al.* 1988), it has been found experimentally that the damping depends sensitively on the surface [illegible] and assembly tolerances in a particular machine.

The designer trying to meet a dynamics related specification needs to [illegible] how much damping to expect, but most of the damping occurs at the material interfaces and cannot be predicted. Moreover, considerable performance gains can often be obtained by increasing the damping, especially [illegible] with feedback control (e.g., Book, 1988). Hence we seek in the present study to develop methods to economically, predictably, and robustly augment the damping in machines.

1.2 Overview

Consider the problem of designing the Cartesian wafer handling [illegible] in Fig. 1.3 for rapid motion. The first two mode shapes of such a machine [illegible]

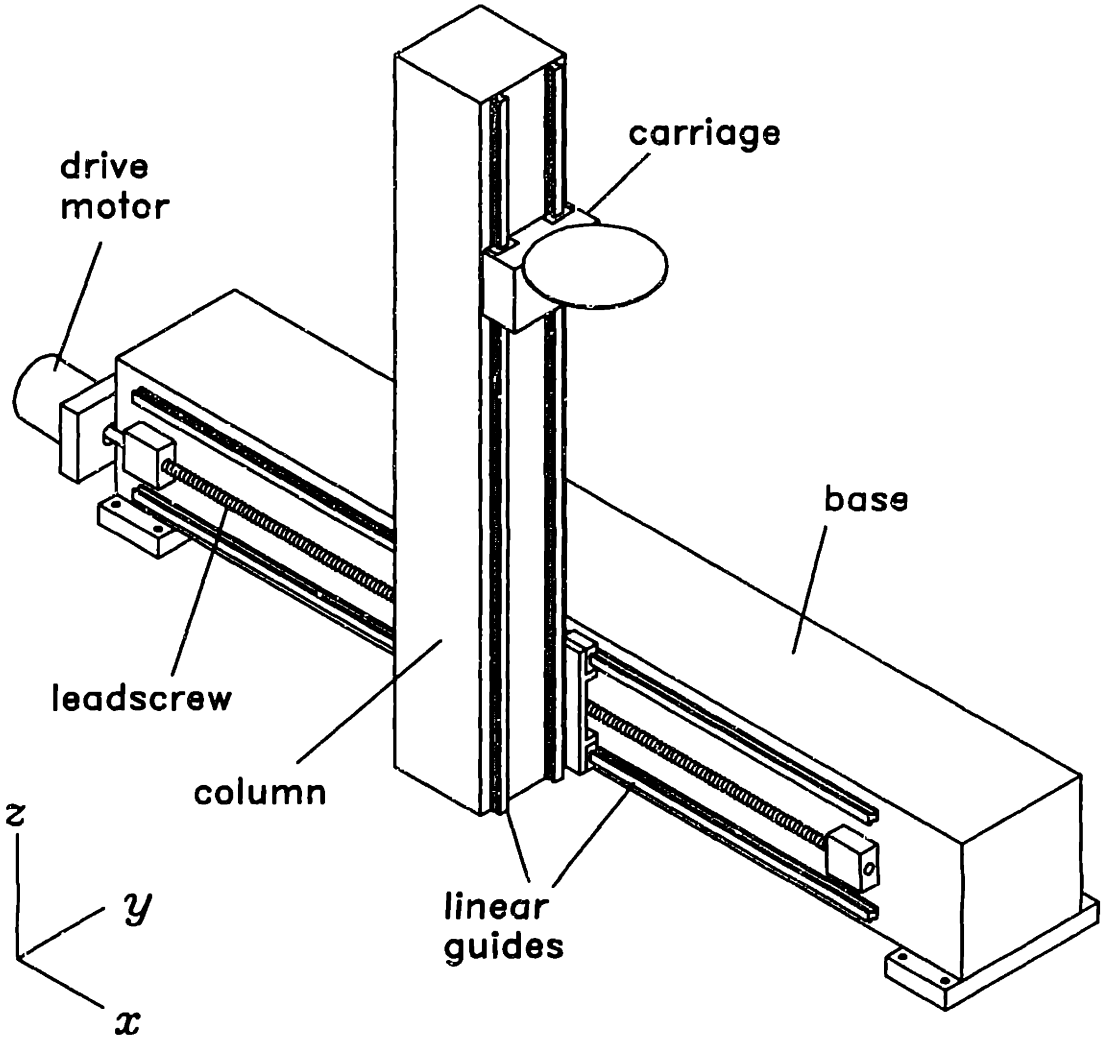

Figure 1.3 Isometric of a wafer-handling robot.

(depending on the details of the design) appear something like those shown in Fig. 1.4. The first mode involves significant twist and flexure of the base, transverse deformation of the linear bearings, and flexure of the column in the y direction; the second mode involves flexure of the column in the x direction, transverse deformation of the linear bearings, and longitudinal deformation of the x-axis drive. Upon review of the literature, we find that tools for the design of damping treatments for these modes of vibration do not exist. The development of such tools is the goal of the present work.

The Design of Damping Treatments

Before introducing damped elements into a machine, it is important to understand how the dynamics of the machine will be affected. In Chapter 2, we examine the behavior of systems with damped elements and develop some guidelines for placement and sizing of dampers in machines. As we shall see, the distribution of stiffness and inertia in a machine determines to a large extent where dampers should be placed.

There are many physical mechanisms of damping, any of which could be employed to augment the damping in a given machine element. The choice is constrained by a number of factors, and a successful damper is often the result of considerable ingenuity on the part of the designer. Among the most effective, robust, and economical methods of dissipating energy in structures is the inducement of strain in viscoelastic materials. Hence we focus on their application in this work.

Damping Flexural and Torsional Vibration

Often, stiffness against flexure and torsion in slender beam-like elements can be obtained only at the cost of a considerable increase in mass. This places a severe limitation on dynamic performance, especially in servomachinery, so designers have long sought effective dampers of vibration of beam-like elements. Sandwich beams consisting of alternating elastic and viscoelastic layers are known to have particularly high damping. This construct, known as a constrained-layer damper, has found wide application in civil, mechanical, and especially aerospace structures over the last forty years. But the theory and practice has focused almost exclusively on the damping of bending vibration in one plane.

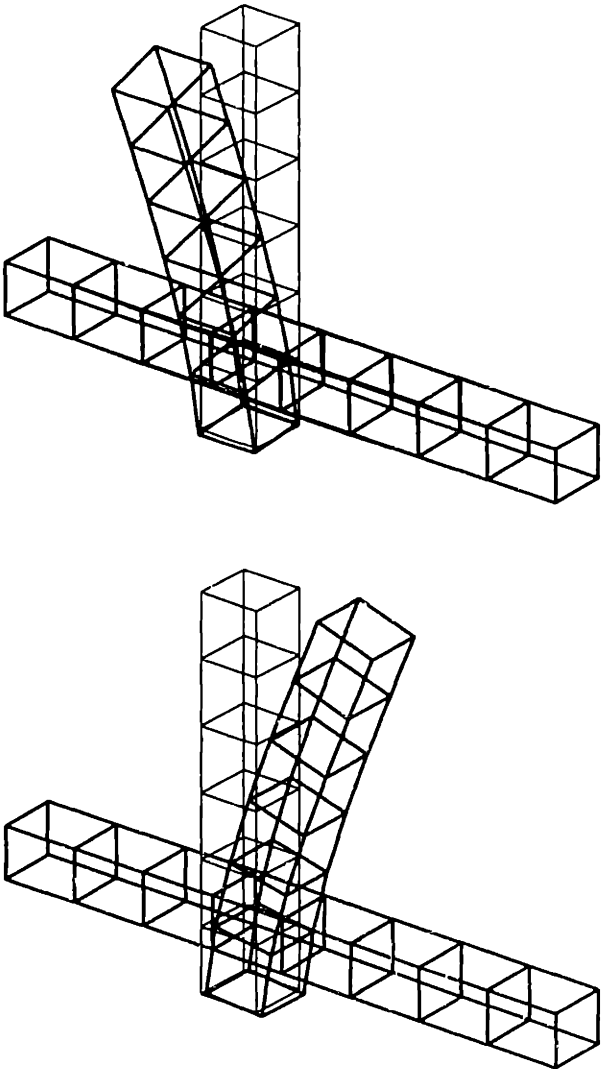

Figure 1.4 First two modes of the wafer-handling robot of Fig. 1.4.

It is therefore a goal of this research to develop analytical models of three-dimensional motion of structures that incorporate viscoelastic laminae. In the latter part of Chapter 2, we provide a review of the theory of planar constrained-layer damping (i.e., vibration of sandwich beams in the plane normal to that of lamination) and develop a finite-beam element suitable for analysis of planar motion of built-up structures with constrained-layer dampers.

In Chapter 3, we consider flexural motion of a sandwich beam in its plane of lamination. Approximating the behavior of the viscoelastic material as frequency-independent hysteretic, we derive an analytical model in the form of a boundary-value problem and study the resonant frequencies and loss factors for simple boundary conditions. Next, we develop approximate solutions by the classical Rayleigh-Ritz and low-order finite-element discretizations for cases including mixed boundary conditions and segmented elastic layers. In Chapter 4, we take up the problem of torsional vibration and develop a model for the Saint-Venant torsion of thin-walled elastic viscoelastic tubes. We develop a general set of equations and matching conditions for the warping displacement of the composite tube and then use these to derive expressions for the complex torsional stiffness of some basic tube geometries.

Damping Leadscrew Drives

Manufacturers of machine tools and precision manipulators have long relied on leadscrew drives for accurate positioning of linear-motion systems. But as speeds of operation increase, the dynamical behavior of leadscrew mechanisms takes on increasing importance in determining the stability and accuracy of machines (Chen and Tlusty, 1995). In Chapter 5, we present a new method for damping axial motion in leadscrew drives through the leadscrew's supports.

Sensitivity Analysis

For relatively simple lumped-parameter models it is a straightforward task to determine the "best" values for stiffness, inertia, and damping for a given arrangement. But for machines that require high-order or distributed-parameter modeling, and where there are a large number of design parameters to be set, our task is far more difficult, and an iterative approach is usually the most practical. Sensitivity analysis is at the heart of such optimization techniques, and we provide a survey of the methods and applications of sensitivity analysis

in Chapter 6.

Decoupled Eigenvalue Sensitivities

The most vital information in iterative design optimization is the sensitivity of performance measures to changes in design parameters. But if the number of parameters is large, this information, while useful to numerical schemes in the raw, lends little insight to the designer. In Chapter 7, we explore the idea of finding a set of infitessimal design changes such that each member of the set modifies only a particular natural frequency of a structure. Such a set would decompose the design space into subspaces corresponding to the individual eigenvalues of structural vibration and would give the designer considerable guidance in optimization of machine performance.

Design Example

A number of methods for augmenting the damping in machine elements are developed in this thesis, and their individual application is illustrated by examples along the way. In Chapter 8, we use the example of the machine shown in Fig. 1.3 to illustrate their use in concert to obtain loss factors of better than seven per cent for the lowest two modes.

We begin by applying the methods of Chapter 6 to adjust key dimensions of the machine to maximize the lowest resonant frequency and then use the results obtained in Chapters 2–5 to individually size dampers for each of the major elements of the machine. Next, we use a low-order finite-element model to predict the damping of the first two modes of the machine with these dampers in place and to tune the design parameters to maximize the damping.

1.3 Summary of Contributions

1. Non-planar flexure of elastic-viscoelastic beams: We show that a sandwich beam with elastic and viscoelastic layers can be designed to have high damping in flexural vibration both in the plane of lamination and the plane normal to lamination.

2. Torsion of elastic-viscoelastic beams: We derive formulae for the damping of closed, thin-walled tubes with constrained viscoelastic layers in tor-

sion and find that significant damping can arise from differential warping of the tube wall and constraining layers.

3. Low-order finite-element modeling of damped structures: We develop a finite-beam element for rapid modeling of built-up structures involving elastic-viscoelastic beams.

4. Longitudinal vibration in leadscrew drives: We present a new method of damping longitudinal vibration in leadscrew drives through the support bearings. We show that the attainable damping is proportional to the preload force necessary to accommodate thermal expansion in the screw.

5. Decoupled eigenvalue sensitivities: We develop the idea of orthogonalizing the sensitivities of the eigenvalues to shape changes so that each member of the set of sensitivities modifies only one eigenvalue of a structure.

CHAPTER 2

The Design of Damping Treatments

2.1 Modeling Damping

A system in which the damping forces at any instant are proportional to the velocity of motion is said to have viscous damping. For a single-degree-of-freedom oscillator the equation of motion takes the familiar form

$$m\ddot{x} + c\dot{x} + kx = F(t) \tag{2.1}$$

which is usually written as

$$\ddot{x} + 2\zeta\omega_n\dot{x} + \omega_n^2 x = F(t)/m \tag{2.2}$$

where $\zeta = c/2\sqrt{km}$ is the damping ratio and $\omega_n = \sqrt{k/m}$ is the undamped natural frequency of oscillation.

Loss Factor

Unfortunately, most of the damping present in machine structures does not obey the viscous damping model, and mathematical descriptions of the damping force are too cumbersome for practical use. Hence, rather than attempting to set forth a model for the damping force, we characterize it by the amount of energy dissipated under steady harmonic motion. The most common measure of this dissipation is the loss factor η, which is formed by taking the ratio of

the *average* energy dissipated per radian to the peak potential energy during a cycle. That is,

$$\eta = \frac{W}{2\pi U} \tag{2.3}$$

where W is the energy dissipated per cycle and U is the peak potential energy. For example, in a system with viscous damping, the energy dissipated during a period of harmonic motion $x = a\sin\omega t$ is

$$W = \oint c\dot{x}\,dx = \int_0^{2\pi/\omega} c\dot{x}^2\,dt = \pi c\omega a^2 \tag{2.4}$$

At resonance, $\omega = \sqrt{k/m}$ and we have $W = 2\pi\zeta ka^2$ and therefore the loss factor at resonance is 2ζ. For most materials and structures, we can't derive an expression for the loss factor and must instead rely on measurements of the stiffness and loss factor as a function of temperature and frequency.

A direct extension of Eq. (2.3) is that a system composed of N elements each with loss factor η_k has a system loss factor given by

$$\eta = \frac{\sum_{k=1}^{N} \eta_k U_k}{\sum_{k=1}^{N} U_k} \tag{2.5}$$

where U_k is the peak energy stored in the kth element while undergoing vibration. This formula is often used to approximate the loss factor of a system if one has an idea of the mode shape. It also confirms for us the intuitive notion that to increase the damping we must channel the strain energy into lossy elements of a machine.

Hysteretic Damping and Complex Stiffness

Now supposing that we impose the cyclic deformation $x = a\cos\omega t$ on a sample and find that the force lags the displacement by the angle ϕ so that it can be written as

$$f = ka\cos(\omega t + \phi) = ka\,(\cos\phi\cos\omega t - \sin\phi\sin\omega t) \tag{2.6}$$

Then the work done per cycle is

$$W = \int_0^{2\pi/\omega} f\,dx = \pi ka^2\sin\phi \tag{2.7}$$

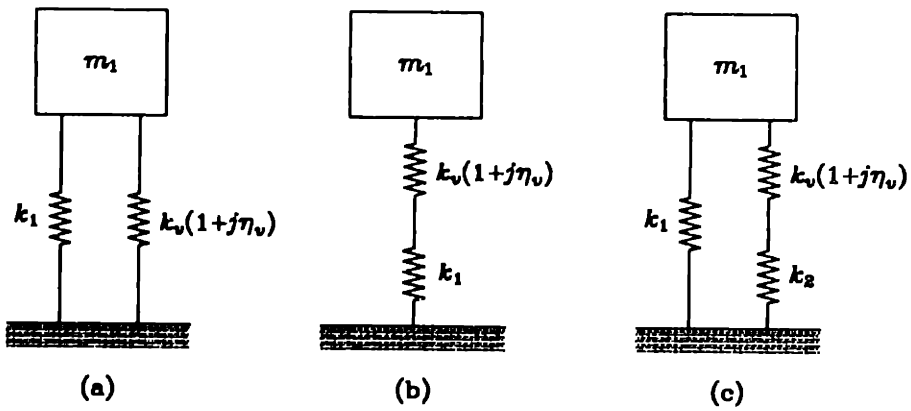

Figure 2.1 Combinations of elastic and hysteretic elements: (a) parallel, (b) series, and (c) parallel stacked.

and the maximum potential energy is $(ka^2 \cos\phi)/2$ so that $\eta = \tan\phi$. The harmonic force can then be written as

$$f = ak' (\cos\omega t - \eta \sin\omega t) \tag{2.8}$$

If we introduce complex notation and write $x = ae^{j\omega t}$, then the force can be written as

$$f = \mathrm{Re}\,[k'(1 + j\eta)x] \tag{2.9}$$

The quantity $k'(1 + j\eta)$ is known as the complex stiffness. It can only be used for under the condition of steady harmonic motion.

In a causal system, the complex stiffness is necessarily a function of frequency (Crandall, 1970); hence to predict the loss factor of a given resonance we must first estimate its frequency well enough to specify the correct complex stiffness for the various components. Fortunately, the complex stiffness usually varies slowly enough with frequency to make this approach practical.

2.2 Basic Damper Configurations

Consider the problem of damping the vibration of an elastic structure of effective mass m_1 and stiffness k_1 by the introduction of a hysteretic damping element. If, as shown in Fig. 2.1(a), a hysteretic damping element of complex

stiffness $k_v(1+j\eta_v)$ is placed in parallel with k_1, the complex stiffness $k(1+j\eta)$ of the structure (normalized against k_1) becomes

$$\frac{k}{k_1}(1+j\eta) = (1+Y)\left(1+j\frac{Y\eta_v}{1+Y}\right) \tag{2.10}$$

where the "stiffness ratio" $Y = k_v/k_1$. Hence, for a parallel combination of hysteretic and elastic springs, the damping as well as the static stiffness increases monotonically as the stiffness ratio Y is increased, and the loss factor approaches that of the hysteretic damping element as $Y \to \infty$. Under static load, the creeping deflection is limited to Y times the instantaneous deflection. Unfortunately, it is rarely possible to introduce a damping element in parallel to the load path in a machine.

On the other hand, it is usually easy to introduce a hysteretic element into the load path in series with the load-carrying elements to obtain the configuration shown in Fig. 2.1(b). In this case, the effective normalized complex stiffness is

$$\frac{k}{k_1}(1+j\eta) = \frac{g+g^2(1+\eta_v^2)}{1+2g+g^2(1+\eta_v^2)}\left(1+j\frac{\eta_v}{1+g(1+\eta_v^2)}\right) \tag{2.11}$$

where the "coupling parameter" $g = k_v/k_1$. Thus we see that in a series combination the loss factor drops (and the stiffness increases) monotonically as the coupling parameter g is increased. Such a configuration may be useful when it is permissible to allow the stiffness to drop in exchange for damping. But series configurations are rarely used because the creeping deflection is limited only by the hysteretic element, and hence is usually unacceptably large.

In practice, then, we strive for a parallel configuration, but often fall short of this ideal because (as we shall see in many examples) we can't find a rigid support for the hysteretic element. In this case, we have the "parallel stack" configuration of Fig. 2.1(c), where the series combination of a hysteretic element and an elastic element act in parallel with the load path. We define a coupling parameter g as k_v/k_2 and a stiffness parameter Y as k_2/k_1, and write the components of complex stiffness $k(1+j\eta)$ in the form

$$\frac{k}{k_1} = \frac{g^2(1+Y)(1+\eta_v^2)+g(2+Y)+1}{(1+g)^2+(g\eta_v)^2} \tag{2.12}$$

and

$$\eta = \frac{gY\eta_v}{g^2(1+Y)(1+\eta_v^2) + g(2+Y) + 1} \tag{2.13}$$

From Eq. (2.13), we see that for a given Y the loss factor does not increase monotonically with g, but reaches a peak at an intermediate value of g as shown in Fig. 2.2.

It is therefore useful to establish a formula for the optimal value of g for a given Y. Following the approach of Marsh and Hale (1997), we differentiate Eq. (2.13) with respect to g, equate the result to zero, and find that the optimal value of g is given by

$$g_0^2 = \frac{1}{(1+Y)(1+\eta_v^2)} \tag{2.14}$$

which corresponds to the maximum loss factor

$$\eta_m = \frac{Y\eta_v}{Y + 2 + 2[(1+Y)(1+\eta_v^2)]^{1/2}} \tag{2.15}$$

We plot the maximum loss factor η_m as a function of Y for various η_v in Fig. 2.3. The damping increases monotonically with the stiffness ratio Y provided that g is maintained at its optimum value, and the key to the successful design of damping treatments is the maximization of the stiffness ratio Y in the face of weight or space penalties.

It is useful to note that the stiffness ratio can be interpreted as the fractional increase in stiffness when the hysteretic element is varied from perfectly compliant to perfectly rigid; that is,

$$Y = \frac{k_\infty - k_0}{k_0} \tag{2.16}$$

where k_∞ and k_0 are, respectively, the stiffnesses of the structure when the hysteretic element is perfectly rigid and perfectly compliant. The coupling parameter g is in general the ratio of the stiffnesses of the hysteretic element and its series companion; it is a measure of where a particular design lies between the perfectly compliant and perfectly rigid extremes.

Example: Damping Transverse Motion in Bearings

A resonance frequently encountered in linear-motion systems, such as the one shown in Fig. 2.4, is a "rigid-body" mode involving roll of the carriage about

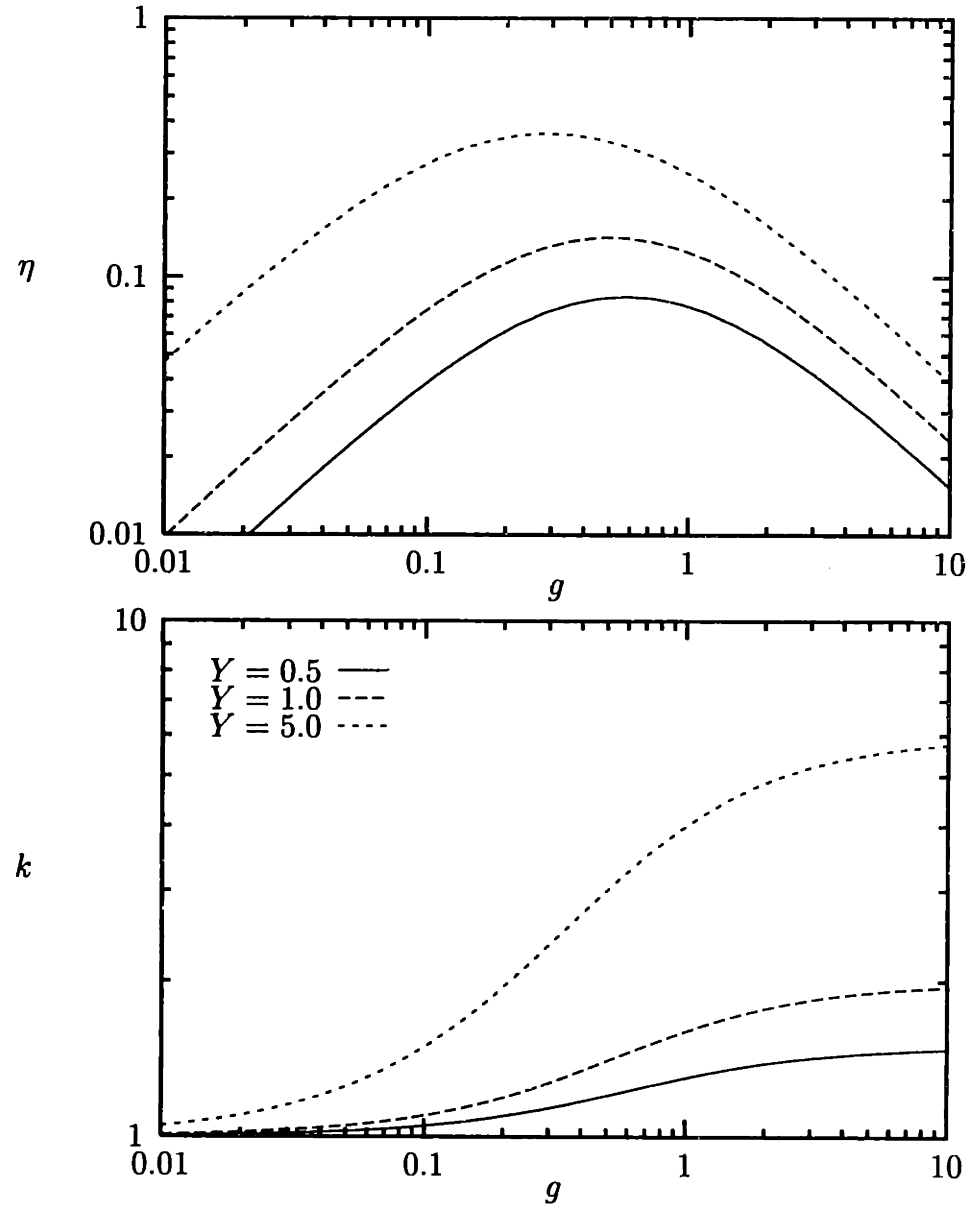

Figure 2.2 Stiffness and loss factor of the parallel stacked system of Fig. 2.1(c) as a function of the coupling parameter g with $\eta_v = 1$ and various values of Y.

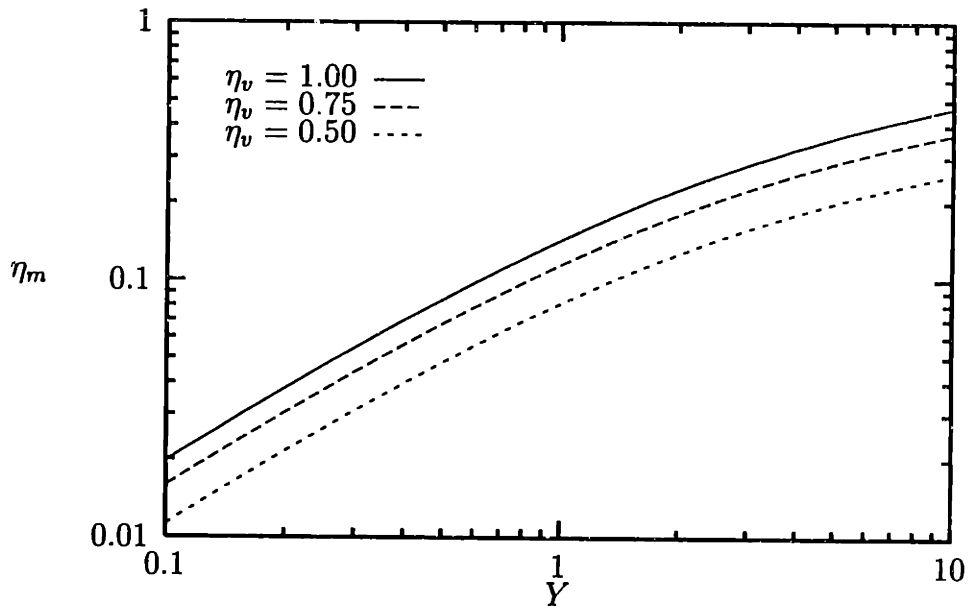

Figure 2.3 Maximum loss factor as a function of the stiffness parameter Y for various viscoelastic material loss factors η_v.

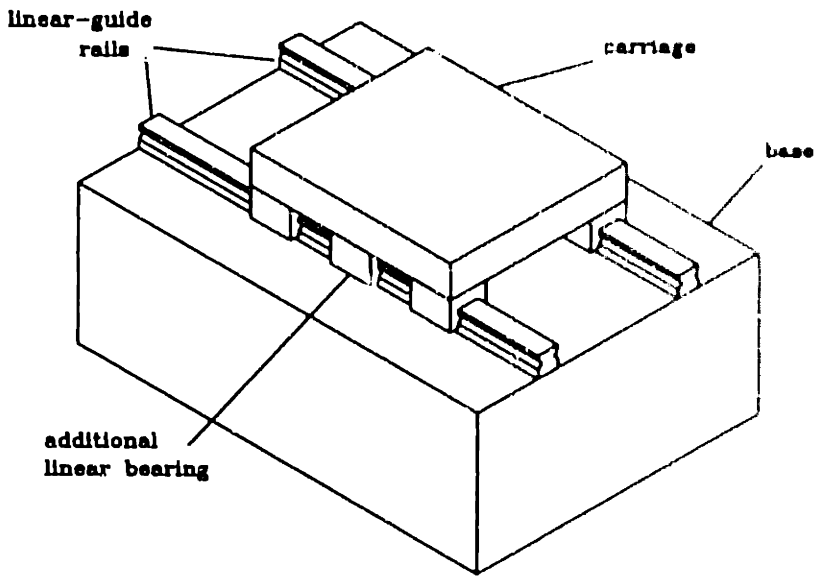

Figure 2.4 A carriage on linear guides: An additional bearing on each linear guide serves to stiffen and damp rolling motion of the carriage about its axis of travel

its axis of travel. One method of raising the natural frequency as well as the damping of such a mode is the introduction of an additional linear bearing on each rail and coupling it to the carriage via a layer of viscoelastic material. If the only compliance in the system is the linear bearings, then we have exactly the the parallel stack configuration of Fig. 2.1(c). Because the additional bearings have presumably the same stiffness as the four original bearings, we have $Y = 0.5$. Hence, assuming a lossy viscoelastic material with $\eta_v = 1$, we compute from Eq. (2.15) that the maximum achievable loss factor is 0.084. This maximum damping is obtained with $g = 0.58$ and the stiffness against roll with this value of g is 22 per cent greater than that of the carriage without additional bearings.

So is this any better than rigidly coupling the additional bearing to the carriage? Rigidly coupling the carriage to the extra bearings would not significantly increase the damping, but it would raise the stiffness against roll by 50 per cent over that of the carriage without additional bearings. Whether it is more important to raise the damping or the stiffness depends on the design objectives as well as the nature of the disturbances, but an important factor in comparing the performance of these designs is the degree of damping that would be present in the rigidly coupled case. Measurements indicate that η is typically between 0.005 and 0.03 if the carriage is on recirculating ball bearings, and between 0.02 and 0.04 if it is on recirculating roller bearings. If the loss factor of the rigidly coupled system is at the high end of this range, it may not pay off to augment the damping using viscoelastic material.

2.3 Constrained-Layer Damping

Consider the elastic-viscoelastic sandwich beam shown in Fig. 2.5. It consists of a principal load-carrying layer to which are laminated relatively compliant viscoelastic layers followed by constraining layers with stiffness comparable to that of the principal layer. When this viscoelastic sandwich beam undergoes flexural vibration in the z direction (the direction normal to the plane of lamination), the viscoelastic layers are subjected to large shear strains and energy is dissipated; this so-called constrained-layer or shear damping mechanism has found application in aerospace, automotive, machine-tool, and civil structures.

In this section, we provide a brief review of the theory of vibration of viscoelastic beams in the plane normal to lamination (the xz plane in Fig. 2.5),

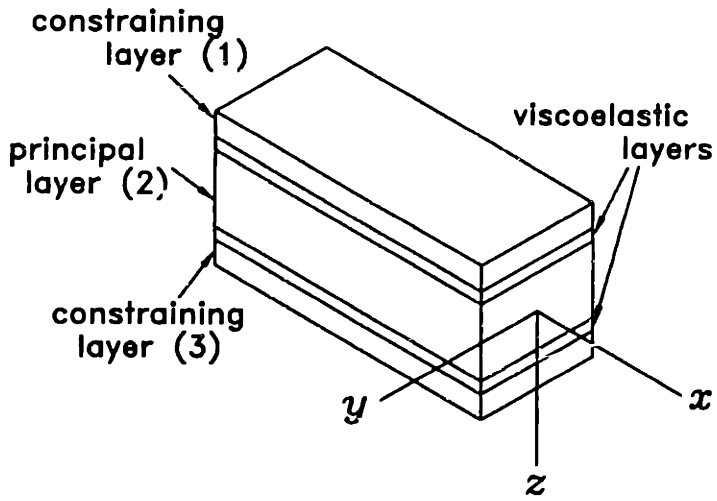

Figure 2.5 Sketch of a five-layer sandwich beam.

and develop a finite sandwich-beam element for use in the analysis of built-up structures with constrained viscoelastic layers.

2.3.1 Background

A substantial body of literature on constrained-layer damping has developed in the forty years since the concept was first suggested by Plass (1957) and Kerwin (1959). The theoretical foundation for much of the work that followed was laid by Ross *et al.* (1959) who analyzed the vibration of a three-layer sandwich beam under sinusoidal deflections. Since then, various researchers have extended the theory to include various boundary conditions (DiTaranto, 1965; Mead and Markus, 1969; Rao, 1978), segmented and multiple constrained layers (e.g., Plunkett and Lee, 1970), and a host of other geometries as summarized in the review by Torvik (1980).

The theory has also been extended to account for higher-order effects such as rotary inertia and shear deformation (e.g., Rao, 1977; Chen and Levy, 1996). Other researchers have presented simplified analyses for design along with fabrication methods for internal shear dampers (Ruzicka, 1961; Marsh and Slocum, 1996). In recent years, a number of studies have focused on the construction of damped sandwich structures with anisotropic layers (e.g., Rao

and He, 1993). The work cited in the foregoing is only a small sample of that which has appeared over the years. For a more comprehensive survey, the reader is directed to the review article by Torvik (1980).

2.3.2 Three-Layer Laminate

The basic model of vibration of elastic-viscoelastic beams in the direction normal to the plane of lamination was set forth by Ross, Ungar, and Kerwin in 1959 (Ross *et al.*, 1959) and is often referred to in the literature as the "RKU model." Their analysis is based on the following assumptions:

1. The shear strains in the elastic layers are negligible in comparison with the shear strains in the viscoelastic layers.

2. The normal stresses in the viscoelastic layers are negligible in comparison with the normal stresses in the elastic layers.

3. Transverse strains in both the elastic and viscoelastic layers are negligible so that the transverse deflections of the various layers are equal.

4. Longitudinal and rotary inertia are negligible.

Using these assumptions, Ross *et al.* obtained an expression for the damping of a laminate vibrating in the shape of a sine wave.

Later, DiTaranto (1965) formulated a sixth-order equation which, along with suitable boundary conditions, forms an eigenvalue problem for the resonant frequencies and loss factors of a finite-length sandwich beam and later discussed methods for its solution (Ditaranto and Blasingame, 1967). Though DiTaranto formulates the sixth-order equation of motion in terms of the longitudinal deflection, subsequent researchers (e.g., Mead and Markus, 1968; Rao, 1978) have preferred to write the equation of motion in terms of the transverse deflection. In this work we wish to design built-up structures which contain sandwich beams and it is simplest to set forth the boundary conditions if the governing equations are written in terms of both the transverse and longitudinal displacements.

Under assumptions 1–4 above, the deformation of a three-layer laminate is as shown in Fig. 2.6, and the shear strain in the viscoelastic layer is given by

$$\gamma_{xz}(x) = \frac{1}{t_v}\left[u_2(x) - u_1(x) + cw'(x)\right] \tag{2.17}$$

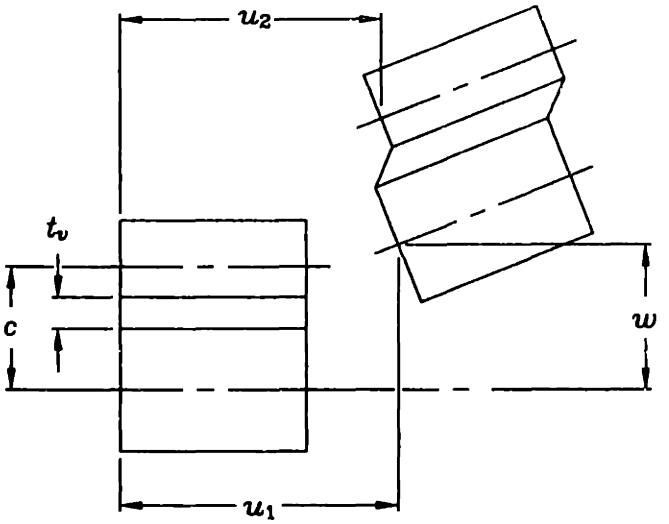

Figure 2.6 Undeformed and deformed configurations of an element of a three-layer sandwich beam: Points on the neutral axes of the elastic layers undergo longitudinal deflections $u_1(x)$ and $u_3(x)$ as the sandwich beam undergoes a transverse deflection $w(x)$.

where $w(x)$ is the transverse displacement of the composite beam, $u_1(x)$ and $u_2(x)$ are the longitudinal displacements of the neutral axes of the elastic layers, t_v is the thickness of the viscoelastic layer, and c is the distance between the neutral axes of the elastic layers. Making use of this expression and introducing the complex shear modulus G and width $2h$ of the viscoelastic layer, we write the equations of longitudinal equilibrium in the elastic layers as

$$E_1 A_1 u_1'' + \frac{2Gh}{t_v}(u_2 - u_1 + cw') = 0 \tag{2.18}$$

$$E_2 A_2 u_2'' - \frac{2Gh}{t_v}(u_2 - u_1 + cw') = 0 \tag{2.19}$$

where $E_1 A_1$ and $E_3 A_3$ are the extensional rigidities of, respectively, the bottom and top elastic layers of the laminate. For steady harmonic motion with angular frequency Ω, the equation of equilibrium in the transverse direction takes the form

$$-\Omega^2(\rho_1 A_1 + \rho_2 A_2)w + (E_1 I_1 + E_2 I_2)w^{iv} = \frac{2Ghc}{t_v}(u_2' - u_1' + cw'') \tag{2.20}$$

where, in accordance with the usual notation for an elastic layer, the flexural rigidities are E_1I_1 and E_2I_2 and the masses per unit length are ρ_1A_1 and ρ_2A_2. Equations (2.18)–(2.20) appear to form an eighth-order system, but in fact one of the longitudinal equations can be eliminated because we must have

$$E_1A_1u_1' + E_2A_2u_2' = 0 \tag{2.21}$$

in order to maintain longitudinal equilibrium of the composite beam.

We now introduce the dimensionless coordinate $\xi = x/L$ and characteristic time

$$t_0 = L^2\sqrt{\frac{\rho_1A_1 + \rho_2A_2}{E_1I_1 + E_2I_2}} \tag{2.22}$$

which is recognized to be proportional to the period of oscillation of the coupled beam system if the shear stiffness of the viscoelastic layer is set to zero. Combining Eqs. (2.18)–(2.21), we can write a single differential equation in w:

$$\frac{\partial^6 w}{\partial\xi^6} - g(1+Y)\frac{\partial^4 w}{\partial\xi^4} + \omega^2\left(\frac{\partial^2 w}{\partial\xi^2} - gw\right) = 0 \tag{2.23}$$

where ω is the dimensionless frequency of motion and the coupling or shear parameter is

$$g = g_r(1 + j\eta_v) = \frac{2GhL^2}{t_v}\left(\frac{E_1A_1 + E_2A_2}{E_1A_1E_2A_2}\right) \tag{2.24}$$

and the stiffness or geometric parameter is

$$Y = \frac{c^2}{E_1I_1 + E_2I_2}\left(\frac{E_1A_1E_2A_2}{E_1A_1 + E_2A_2}\right) \tag{2.25}$$

Equation (2.23) with three boundary conditions involving up to the fifth derivative of w at each end form an eigenvalue problem for the complex resonant frequency ω.

A closed-form solution of Eq. (2.23) is available for a simply supported beam without longitudinal restraints. The dimensionless frequency of the nth mode is given by

$$\mathrm{Re}\,\omega_n = (n\pi)^2\left[\frac{(n\pi)^4 + (n\pi)^2(2+Y)g + (1+\eta_v^2)(1+Y)g^2}{(n\pi)^4 + 2(n\pi)^2g + (1+\eta_v^2)g^2}\right]^{1/2} \tag{2.26}$$

and the corresponding loss factor is

$$\eta_n = \frac{(n\pi)^2 g Y \eta_v}{(n\pi)^4 + (n\pi)^2(2+Y)g + (1+\eta_v^2)(1+Y)g^2} \tag{2.27}$$

It is interesting to note that these results correspond exactly to Eq. (2.13) if we replace L by the effective length $L/n\pi$ in the definition of g given in Eq. (2.24). Hence we see that constrained-layer damping corresponds exactly to the parallel stacked model of Fig. 2.1(c). For other boundary conditions, the behavior is much the same, but we must resort to numerical or approximate methods to find the effective length.

2.3.3 Finite-Element Model

In the analysis of built-up structures, we often resort to finite-element techniques, and it is somewhat cumbersome to write constraints in a form suitable for the sixth-order differential equation of Eq. (2.23). We choose instead to develop a finite-beam element in terms of the longitudinal and transverse coordinates in a manner that it may be incorporated into a standard finite-element code for framed structures.

Finite-element models for structures are readily obtained using an energy approach, but hysteretic damping is valid only in the frequency domain and energy methods cannot be applied directly. We can, however, introduce virtual displacements in the frequency domain and use these to obtain variational forms of the equations of motion and thence derive the desired finite-element model.

Multiplying Eqs. (2.18), (2.19), and (2.20), respectively, by the virtual displacements $\bar{u}_1$, $\bar{u}_2$, and $\bar{w}$, summing, integrating by parts, and discarding the boundary terms, we obtain a weak variational form of the equations of motion:

$$\int_0^L \left[(E_1 I_1 + E_2 I_2) w'' \bar{w}'' - \Omega^2(\rho_1 A_1 + \rho_2 A_2) w \bar{w}\right] dx = \tag{2.28}$$
$$\int_0^L \left[\frac{2Gh}{t_v}(u_3 - u_1 + cw')(\bar{u}_3 - \bar{u}_1 + c\bar{w}') - (E_1 A_1 u_1' \bar{u}_1' + E_2 A_2 u_2' \bar{u}_2')\right] dx$$

The terms on the left-hand side of this equation correspond to the usual Euler–Bernoulli equations for beam bending and the second term on the right-hand

side accounts for the longitudinal stiffness of the elastic layers. Of interest here are the components of the element stiffness due to the first term on the right-hand side of Eq. (2.28).

Using the standard cubic beam element, we expand the transverse displacement in terms of the displacement and slope at the ends of an element in the form

$$w = \phi_1(x)w(0) + \phi_2(x)w'(0) + \phi_3(x)w(L) + \phi_4(x)w'(L) \tag{2.29}$$

where the interpolation functions are given by

$$\begin{aligned} \phi_1(\xi) &= 1 - 3\xi^2 + 2\xi^3 && (2.30)\\ \phi_2(\xi) &= \xi - 2\xi^2 + \xi^3 && (2.31)\\ \phi_3(\xi) &= 3\xi^2 - 2\xi^3 && (2.32)\\ \phi_4(\xi) &= -\xi^2 + \xi^3 && (2.33) \end{aligned}$$

and $\xi = x/L$. For the longitudinal deflections, we use the linear interpolation functions

$$\psi_1(\xi) = 1 - \xi \quad \text{and} \quad \psi_2(\xi) = \xi \tag{2.34}$$

and expand in the form

$$\begin{aligned} u_1 &= \psi_1(x)u_1(0) + \psi_2(x)u_1(L) && (2.35)\\ u_2 &= \psi_1(x)u_2(0) + \psi_2(x)u_2(L) && (2.36) \end{aligned}$$

Substituting into the weak form given by Eq. (2.28) and requiring that the result be stationary with respect to each coordinate in turn, we obtain discretized equations of motion. If we let

$$\vec{u}_1 = \begin{bmatrix} u_1(0) \\ u_1(L) \end{bmatrix} \quad \vec{u}_2 = \begin{bmatrix} u_2(0) \\ u_2(L) \end{bmatrix} \tag{2.37}$$

and

$$\vec{w} = \begin{bmatrix} w(0) \\ w'(0) \\ w(L) \\ w'(L) \end{bmatrix} \tag{2.38}$$

we can write the discretized eigenvalue problem in matrix form as

$$-G_2^T \vec{w} + (K_1 + G_3)\,\vec{u}_1 - G_3 \vec{u}_2 = 0 \tag{2.39}$$

$$G_2^T \vec{w} - (K_2 + G_3)\,\vec{u}_2 - G_3 \vec{u}_1 = 0 \tag{2.40}$$

and

$$\left(K_3 + G_1 - \Omega^2 M_3\right)\vec{w} + G_2\,(\vec{u}_1 - \vec{u}_2) = 0 \tag{2.41}$$

The matrices G_1 through G_3 account for the stiffness of the viscoelastic layer; they are defined as

$$(G_1)_{ij} = \frac{2Ghc^2}{t_v}\left\langle \phi_i', \phi_j' \right\rangle \tag{2.42}$$

$$(G_2)_{ij} = \frac{2Ghc}{t_v}\left\langle \phi_i', \psi_j \right\rangle \tag{2.43}$$

$$(G_3)_{ij} = \frac{2Gh}{t_v}\left\langle \psi_i, \psi_j \right\rangle \tag{2.44}$$

where $\langle f(x), g(x)\rangle = \int_0^L f(x)\,g(x)\,dx$. The matrices M_3 and K_1 through K_3 are the beam mass and stiffness matrices in the standard form tabulated in many texts (e.g., Thomson, 1988):

$$(K_1)_{ij} = E_1 A_1 \left\langle \psi_i', \psi_j' \right\rangle \tag{2.45}$$

$$(K_2)_{ij} = E_2 A_2 \left\langle \psi_i', \psi_j' \right\rangle \tag{2.46}$$

$$(K_3)_{ij} = (E_1 I_1 + E_2 I_2)\left\langle \phi_i'', \phi_j'' \right\rangle \tag{2.47}$$

$$(M_3)_{ij} = (\rho_1 A_1 + \rho_2 A_2)\left\langle \phi_i, \phi_j \right\rangle \tag{2.48}$$

2.3.4 Five-Layer Symmetric Laminates

Many of the most useful designs make use of a central elastic layer with identical constrained viscoelastic layers mounted to each face. In this case, the net longitudinal force on the principal layer is zero, and the neutral axis of the composite beam coincides with its center line. Hence, the differential equation (2.23) derived for a three-layer beam can be used for a five-layer beam by setting

$$Y = \frac{2c^2 E_2 A_2}{E_1 I_1 + 2E_2 I_2} \tag{2.49}$$

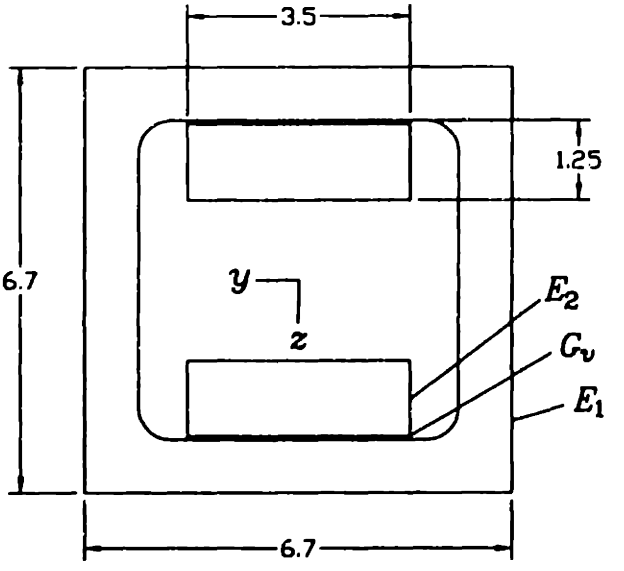

Figure 2.7 Cross section of a ceramic box beam with constrained viscoelastic layers: The beam is 0.914 m long and is composed of a principal layer with $E_1 = 311$ GPa, constraining layers with $E_2 = 372$ GPa, and viscoelastic layers with $G = 7.6(1 + j1.0)$ MPa (at 1000 Hz) and thickness 0.25 mm.

and

$$g = \frac{GhL^2}{t_v E_2 A_2} \tag{2.50}$$

It is also straightforward to couple any number of layers using our finite-element model, but it is most computationally efficient to take advantage of the symmetry by constraining extension of the first layer and lumping the stiffness and inertia of both constraining layers into the second layer of the finite-element model.

Example: Ceramic Box Beam

Consider the ceramic box beam shown in Fig. 2.7 with constrained viscoelastic layers mounted on its interior. The principal layer is a box beam composed of 96 per cent alumina ceramic with Young's modulus $E_1 = 311$ GPa and the constraining layers are 99.5 per cent aluminum oxide with $E_2 = 372$ GPa. The

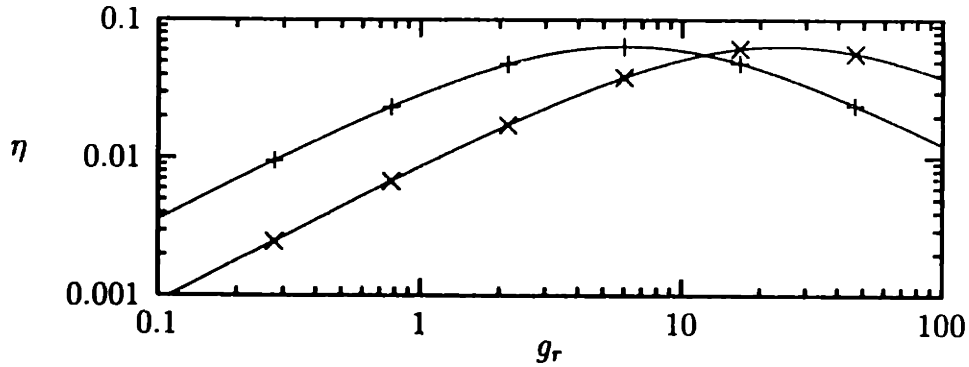

Figure 2.8 Loss factor of the first (+) and second (×) modes of the ceramic beam of Fig. 2.7 on simple supports: The solid lines are the closed-form solution and the symbols are the results of a finite-element calculation.

viscoelastic layers are composed of EAR C-1002 damping elastomer, which at 1000 Hz and room temperature has complex modulus $G = 7.6(1 + j1.0)$ MPa.

For this configuration, we have $Y = 0.37$, and we can plot the loss factor of the first two modes of the simply supported beam as a function of the coupling parameter g as shown in Fig. 2.8. The solid lines correspond to the closed-form solution of Eq. (2.27) and the symbols correspond to the results of a ten-element finite-element model.

Next, consider the same beam with free ends. The loss factor of the first two modes are plotted in Fig. 2.9 as a function of the real part g_r of the coupling parameter g. From the plot, it is apparent that the highest damping of the first mode is attainable with g_r between five and eight. A sample was constructed using viscoelastic layers with thickness 0.25 mm, which for the material properties at 1000 Hz and room temperature has $g = 5.4(1+j1.0)$. We suspended the beam at its quarter points (approximately at the nodes of the first mode) using light surgical tubing and measured the endpoint receptance in the vertical direction; the results are shown in Fig. 2.10. The measured data compare to the finite-element predictions as follows:

frequency (Hz)		loss factor	
measured	predicted	measured	predicted
804	812	0.051	0.058
1980	2115	0.031	0.034

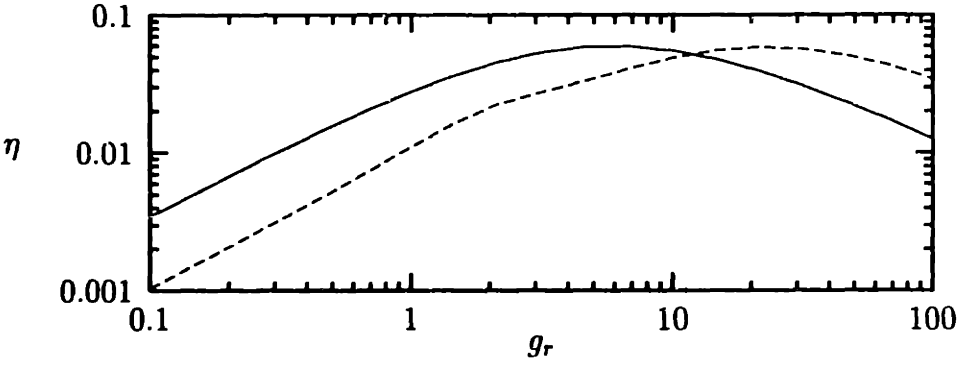

Figure 2.9 Finite-element prediction of the loss factor of the first (solid line) and second (dashed line) modes of the ceramic beam of Fig. 2.7 with free ends.

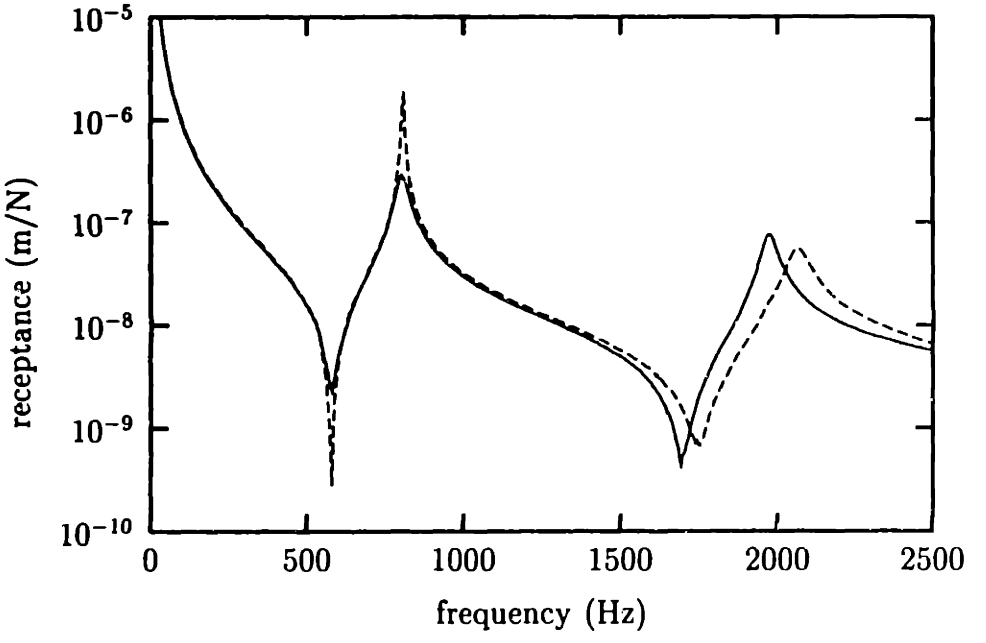

Figure 2.10 Measured endpoint receptance in the y (dashed line) and z (solid line) directions of the ceramic beam of Fig. 2.7: A free-free condition was approximated by suspending the beam with light surgical tubing.

The significant discrepancies between the measured and predicted values of damping may be attributed to errors in the viscoelastic material properties and—in the case of the second mode—coupling to the surgical tubing on which the beam is suspended.

The dashed line in Fig. 2.10 is the receptance in the plane of lamination (i.e., the y direction in Fig. 2.7). It is notable that the second mode in the y direction is better damped than its counterpart in the x direction. The mechanism of this damping is the subject of the next chapter.

CHAPTER 3

Vibration of Elastic-Viscoelastic Sandwich Beams in the Plane of Lamination

3.1 Introduction

We have seen in Chapter 2 that a sandwich beam consisting of alternating elastic and viscoelastic layers is potentially an effective dissipator of flexural vibration in the plane normal to lamination (the xz plane in Fig. 3.1). This potential was recognized some forty years ago, and an extensive literature and practice has developed since that time, as detailed in Section 2.3. We have also seen experimental evidence (Fig. 2.10) that significant dissipation can occur when such a sandwich beam vibrates in the plane parallel to lamination (the xy plane in Fig. 3.1). But a search of the literature reveals no studies on the vibration of sandwich beams parallel to their plane of lamination. It is our goal in this chapter to develop a model for such vibration.

Though we will develop the theory for a general N-layer laminate, it is perhaps worthwhile to note at the outset that we are interested primarily in three- and five-layer laminates of the type shown in Fig. 3.1 where one of the layers is far more massive than the others. This layer bears the applied loads and we designate it the "principal layer." We refer to the remaining elastic layers as "constraining layers." Though there is no distinction in our formulation between the principal and constraining layers, some of the modeling assumptions we will employ depend on the constraining layers being much thinner than the principal layer.

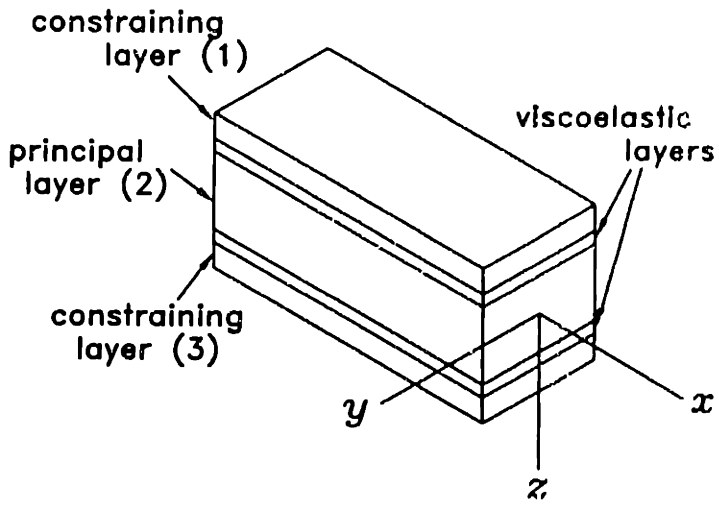

Figure 3.1 Sketch of a five-layer symmetric sandwich beam.

3.2 The Nature of Motion

When a sandwich beam such as the one shown in Fig. 3.1 vibrates in its plane of lamination, the elastic layers need not deflect together and significant strains can be induced in the viscoelastic layers, resulting in potentially high damping. In this section, we develop a picture of the deformations and stresses that arise in such motion and obtain estimates of their relative magnitudes.

3.2.1 Lumped-Parameter Analogy

A lumped-parameter analogy for vibration in the plane of lamination of a sandwich beam such as that shown in Fig. 3.1 can be obtained by lumping the mass and stiffness of each layer as shown in Fig. 3.2. The effective mass and flexural stiffness of the principal layer are lumped into m_2 and k_2. Likewise, we model the first constraining layer as an effective mass m_1 and flexural stiffness k_1 and the second as m_3 and k_3. Although the viscoelastic layers have negligible mass, they act as springs k_{12} and k_{23} that couple the elastic layers.

For a symmetric laminate such as that shown in Fig. 3.1, we have $k_1 = k_3$, $m_1 = m_3$, and $k_{12} = k_{23}$; and the mode shapes of the structure will be either symmetric or antisymmetric. If we for the moment consider k_{12} to be real,

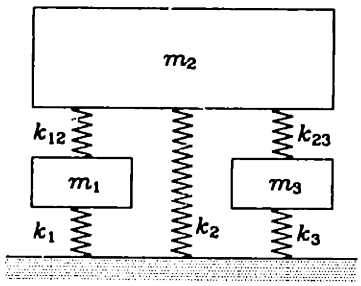

Figure 3.2 Lumped-parameter model for vibration in the plane of lamination of a five-layer beam: The principal layer with effective mass m_2 is coupled via the viscoelastic layers with effective stiffness k_{12} and k_{23} to the constraining layers with effective mass m_1 and m_3.

the mode shapes can be visualized as in Fig. 3.3. The mode shape labeled (d) consists of antisymmetric motion of the constraining layers while the principal layer is still. In (c) the principal layer and constraining layers move in opposite phase. For laminates with reasonably stiff viscoelastic layers, both of these modes impart a great deal of strain energy into the viscoelastic layer, and hence correspond to high-frequency, well-damped modes. The mode shape in (b), on the other hand, corresponds to a relatively low-frequency resonance with somewhat less damping. Here, the largest displacement belongs to the principal layer and hence we refer to such modes as "principal modes." It is our primary goal to develop an accurate model of these.

3.2.2 Coupling Between Bending and Twist

In general the elastic layers that make up a beam like that shown in Fig. 3.1 do not bend together in the xy plane, and their relative motion produces a shearing stress in the viscoelastic layers. These shearing stresses act in such a way as to produce a twisting moment on the elastic layers, in effect coupling bending and twist of the composite beam. In the following, we estimate the angle of twist that results from displacement of one elastic layer relative to another and establish conditions under which the coupling between bending and twist can be ignored.

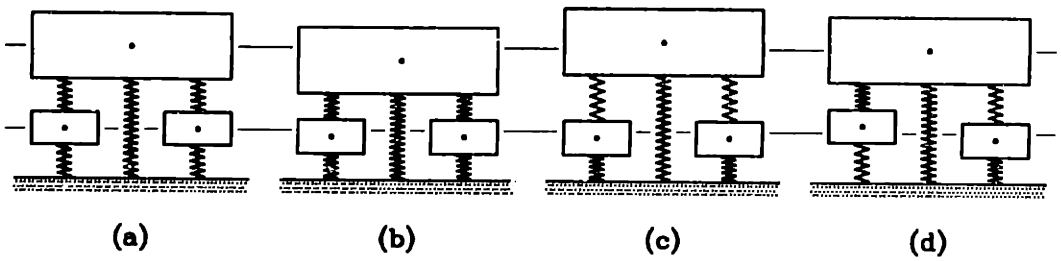

Figure 3.3 Mode shapes from the lumped-parameter model of a symmetric five-layer laminate oscillating in its plane of lamination: (a) static configuration, (b) primary mode, (c) high-frequency symmetric mode, and (d) antisymmetric mode.

Symmetric Modes

For symmetric modes, the principal layer will not twist at all, and we are concerned with rotation of the constraining layers relative to the principal layer. If we neglect the torsional stiffness of the constraining layers, we can treat a constraining layer as a rigid block on a compliant sheet as shown in Fig. 3.4. In response to a force applied at a distance a above the foundation, the displacement v is related to the rotation ψ by

$$\frac{h\psi}{v} = \frac{3G}{E}\left(\frac{a}{h}\right) \sim \frac{a}{h} \tag{3.1}$$

where G and E are, respectively, the shear and elongational moduli of the compliant layer. In our problem, the distance a is the distance from the center of mass of the constraining layer to its base, and the quantity $h\psi$ is the magnitude of the vertical deflection at the edge of the constraining layer. Hence, as long as $a \ll h$, the deflection $h\psi$ due to twist is much smaller than the horizontal deflection v, and twist of the constraining layer can be neglected.

Antisymmetric Modes

For antisymmetric modes, a net moment is exerted on the principal layer, which we take to have a torsional rigidity of G_pJ_p. If, as shown in Fig. 3.5, the constraining layers are displaced a distance v without rotation relative to the principal layer, a twisting moment per unit length of magnitude $(4Ghb/t_v)v$

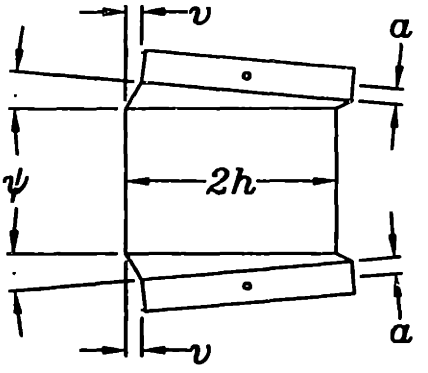

Figure 3.4 Coupling of bending and twist in symmetric modes: A horizontal force applied at the centroid of a constraining layer results in deflection v and rotation ψ relative to the principal layer.

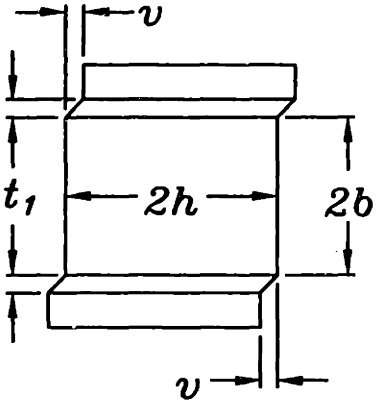

Figure 3.5 Coupling of bending and twist in antisymmetric modes: The constraining layers are displaced a distance v, and the shear stresses developed in the viscoelastic layers exert a moment on the principal layer, causing it to take on an angle of twist ψ.

is exerted on the principal layer. Neglecting the torsional rigidity of the constraining layers, the angle of twist ψ in the principal layer will scale with the displacement v of the constraining layer as

$$\frac{h\psi}{v} \sim \frac{G}{G_p}\left(\frac{h^2L^2b}{t_vJ_p}\right) \tag{3.2}$$

where L is a characteristic length in the longitudinal direction. If the aspect ratio of the cross-section of the principal layer is near unity, we expect that $J_p \sim h^4$ and $b \sim h$ so that we must have

$$\frac{G_p}{G} \gg \frac{L^2}{t_vh} \tag{3.3}$$

in order to ignore twist for antisymmetric modes.

3.2.3 Longitudinal Warping of Cross Sections

When a pair of elastic layers rotate relative to each other, the intervening viscoelastic layer develops shear stresses oriented in the longitudinal direction, giving rise to some warping of the cross sections of the elastic layers. According to the Euler–Bernoulli beam model, the longitudinal strain at a distance y from the neutral axis of a beam bent into the shape $v(x)$ is

$$\epsilon_x = \frac{\partial u}{\partial x} = -y\frac{\partial^2 v}{\partial x^2} \tag{3.4}$$

Hence, for the first few modes of an Euler–Bernoulli beam of length L and height h the maximum longitudinal displacement is of order hv/L. Let us now compare this displacement to that due to warping of cross sections.

As a worst case, consider the deformation in the principal layer of a symmetric laminate undergoing antisymmetric motion. As shown in Fig. 3.6, rotation $\partial v/\partial x$ of a constraining layer causes a relative longitudinal displacement of order $h(\partial v/\partial x)$ in a beam of half-width h. The shear stress induced in the viscoelastic layer is of order Ghv/tL where t is the thickness of the viscoelastic layer. This stress must be matched by a longitudinal shear stress in the principal layer, which over the width of the layer causes longitudinal deflections

$$u_s \sim \frac{Ghvb}{G_pLt} \tag{3.5}$$

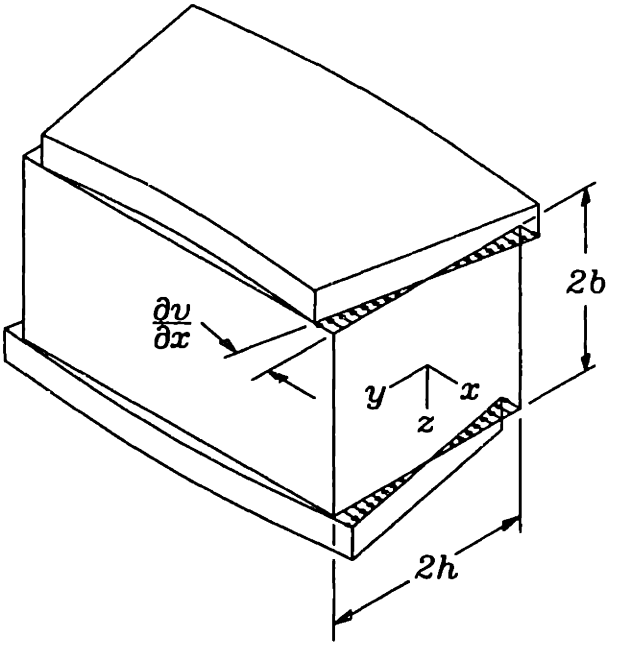

Figure 3.6 Longitudinal warping stresses: Antisymmetric rotational motion of the constraining layers of magnitude $\partial v/\partial x$ induces a distribution of stress that tends to warp the principal layer.

where G_p is the shear modulus of the principal layer and b is its thickness. If we wish to ignore longitudinal warping of sections, we must have

$$\frac{u_s}{u} \sim \frac{G}{G_p}\left(\frac{h}{t}\right) \ll 1 \tag{3.6}$$

3.2.4 Transverse Warping of Cross Sections

Referring again to Fig. 3.5, we see that a shear stress of magnitude Gv/t_v is induced in a viscoelastic layer when the adjoining layers undergo a relative deflection v. Under antisymmetric motion, the shear stress exerted on opposite faces of the principal layer tend to warp its cross section in its own plane. If the principal layer is solid, the shear strains are of order $Gv/G_p t_v$ through its thickness, and we can estimate the magnitude of the resulting deflections v_s by

$$\frac{v_s}{v} \sim \frac{G}{G_p}\left(\frac{b}{t_v}\right) \tag{3.7}$$

For a thin-walled box section, the principal mode of deformation is bending of the walls. If the shear stress in the viscoelastic layer is again Gv/t_v, then

$$\frac{v_s}{v} \sim \frac{G}{E_p}\left(\frac{hb^3}{t_v t_w^3}\right) \tag{3.8}$$

where t_w is the wall thickness of the principal layer. Hence, we see that, as the wall thickness t_w is made small, deformation of the section plays an increasingly important role in antisymmetric motion.

3.2.5 State of Stress in a Viscoelastic Layer

Assuming steady harmonic motion, we let the displacement of the ith layer be

$$\hat{v}_i = v_i e^{j\omega t} \tag{3.9}$$

If plane sections of the elastic layers remain plane and normal to the neutral axis and the neutral axis does not extend, then the harmonic deflection of a point in the elastic layer will be

$$u_i(x,y) = -y\frac{\partial v_i(x)}{\partial x} \qquad \text{and} \qquad v_i(x,y) = v_i(x) \tag{3.10}$$

Then assuming the shear strains do not vary through the thickness of a viscoelastic layer, they are given by

$$\gamma_{xy}(x,y) = 0$$

$$\gamma_{xz}(x,y) = \frac{y}{t_v}\left[\frac{\partial v_i(x)}{\partial x} - \frac{\partial v_{i+1}(x)}{\partial x}\right] \tag{3.11}$$

$$\gamma_{yz}(x,y) = \frac{v_{i+1}(x) - v_i(x)}{t_v} \tag{3.12}$$

$$\tag{3.13}$$

We model the viscoelastic material as hysteretically damped without frequency dependence. This "ideal" hysteretic damping model is valid only for steady harmonic motion (e.g., Crandall, 1991), and can be represented in the frequency domain by a complex stiffness. Hence, we introduce the complex shear modulus $G = G_v(1 + j\eta_v)$ and the harmonically varying shear stresses in the viscoelastic layer are given by $\tau_{xz} = G\gamma_{xz}$ and $\tau_{yz} = G\gamma_{yz}$.

3.3 Equations of Motion

In the following, we consider the balance of forces on an N-layer composite beam during vibration in its plane of lamination and obtain a boundary-value problem governing the harmonic displacement of each of the N layers. We then cast this boundary-value problem in a variational form which we use later to develop approximations for the eigenvalues of motion.

3.3.1 Summary of Modeling Assumptions

In Section 3.2, we developed estimates for the relative magnitude of various components of deflection. Based on these estimates, we make the following modeling assumptions:

1. The principal and constraining layers are perfectly elastic, and the viscoelastic layers are frequency-independent hysteretic.

2. The principal and constraining layers obey the Euler–Bernoulli beam model; that is, rotary inertia as well as all components of shear deformation are neglected in the elastic layers.

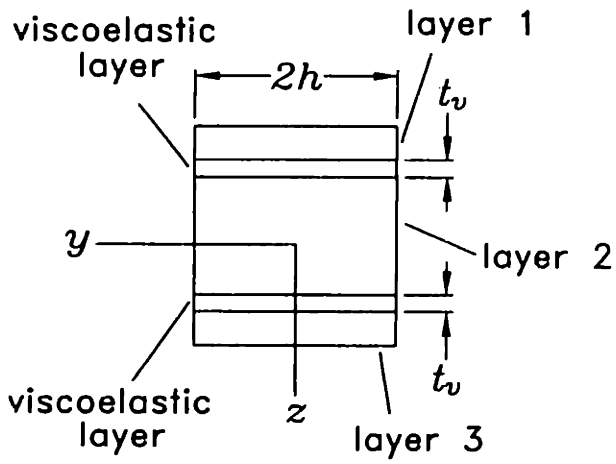

Figure 3.7 Cross-sectional view of a sandwich beam showing the notation used in the analysis: The elastic layers are numbered sequentially from top to bottom, the width of the laminated section is $2h$, and each of the viscoelastic layers is of thickness t_v.

3. The inertia of the viscoelastic layers is negligible. This is usually a safe assumption because the mass density of most damping materials is low in comparison with that of structural materials and most designs employ relatively thin viscoelastic layers.

4. The shear strain is treated as constant through the thickness of a viscoelastic layer.

5. The normal stresses in the viscoelastic layers are negligible in comparison to the normal stresses in the principal and constraining layers. This assumption follows from the viscoelastic layers having comparable normal strains but much lower moduli than the other layers.

6. The angle of twist is negligible in each layer of the composite beam.

3.3.2 Equations of Motion

We now set forth equations of motion for an N-layer sandwich beam of width $2h$ and where all of the viscoelastic layers are of thickness t_v as shown in Fig. 3.7. The ith elastic layer is characterized by flexural stiffness E_iI_i and

mass per unit length $\rho_i A_i$. Denoting its time-harmonic deflection as $v_i(x)$, we obtain an equation of motion in the form

$$-\omega^2 \rho_i A_i v_i + E_i I_i \frac{\partial^4 v_i}{\partial x^4} + Q_i(x) - \frac{\partial R_i(x)}{\partial x} = 0 \tag{3.14}$$

where $Q_i(x)$ and $R_i(x)$ represent, respectively, the distributed force and moment exerted on the layer by conterminous viscoelastic layers. Integrating the shear-stress distribution given in Eqs. (3.11)–(3.13) over the width of the laminate, we obtain the net force per unit length

$$Q_i(x) = -\frac{2Gh}{t_v}(v_i - v_{i+1}) - \frac{2Gh}{t_v}(v_i - v_{i-1}) \tag{3.15}$$

and bending moment per unit length

$$R_i(x) = \frac{2Gh^3}{3t_v}\left(\frac{\partial v_i}{\partial x} - \frac{\partial v_{i+1}}{\partial x}\right) + \frac{2Gh^3}{3t_v}\left(\frac{\partial v_i}{\partial x} - \frac{\partial v_{i-1}}{\partial x}\right) \tag{3.16}$$

At each end of the beam, we must specify either the slope $\partial v_i/\partial x$ or bending moment $E_i I_i \partial^2 v_i/\partial x^2$ and either the displacement v_i or shear force

$$V_i = Q_i - E_i I_i \frac{\partial^3 v_i}{\partial x^3} \tag{3.17}$$

3.3.3 Nondimensional Form

We now designate the pth layer to be the principal layer and introduce the nondimensional variables

$$x^* = x/L \quad \omega^* = \omega t_0 \quad v_i^* = v_i/L \tag{3.18}$$

where L is the length of the beam and t_0 is given by

$$t_0 = L^2\sqrt{\frac{\rho_p A_p}{E_p I_p}} \tag{3.19}$$

which is recognized as a characteristic of the period of oscillation of the principal layer in the absence of any other layers. We next define for the ith layer the mass and stiffness ratios

$$m_i = \frac{\rho_i A_i}{\rho_p A_p} \quad \text{and} \quad k_i = \frac{E_i I_i}{E_p I_p} \tag{3.20}$$

which are, respectively, the ratio of the mass per unit length to that of the principal layer and the ratio of the flexural stiffness to that of the principal layer. We also find it convenient to introduce the displacement coupling parameter

$$g_v = \frac{2GhL^4}{t_v E_p I_p} \tag{3.21}$$

which is the nondimensional restoring force per unit length developed in a viscoelastic layer when the adjoining elastic layers undergo a relative deflection, and the rotation coupling parameter

$$g_m = \frac{2Gh^3L^2}{3t_v E_p I_p} = \frac{h^2}{3L^2} g_v \tag{3.22}$$

which is the nondimensional restoring moment per unit length developed in a viscoelastic layer when adjoining elastic layers undergo a relative rotation.

Substituting these quantities into the governing equation (3.14) and the expressions for the shear force (3.15) and bending moment (3.16), we obtain

$$\begin{aligned} -\omega^{*2} m_i v_i^* + \frac{\partial^4 v_i^*}{\partial x^{*4}} = & \\ -g_v \left(2v_i^* - v_{i+1}^* - v_{i-1}^*\right) + g_m & \left(2\frac{\partial^2 v_i^*}{\partial x^{*2}} - \frac{\partial^2 v_{i+1}^*}{\partial x^{*2}} - \frac{\partial^2 v_{i-1}^*}{\partial x^{*2}}\right) \end{aligned} \tag{3.23}$$

In terms of the nondimensional quantities, the bending moment in the ith layer is $k_i \partial^2 v_i / \partial x^2$ and the internal shear force is

$$V_i^* = g_m \left(2\frac{\partial^2 v_i^*}{\partial x^{*2}} - \frac{\partial^2 v_{i+1}^*}{\partial x^{*2}} - \frac{\partial^2 v_{i-1}^*}{\partial x^{*2}}\right) - k_i \frac{\partial^3 v_i^*}{\partial x^{*3}} \tag{3.24}$$

In the remainder of this work, we will utilize the nondimensional quantities but drop the asterisks and use $(\cdot)'$ to denote $\partial(\cdot)/\partial x$ in oder to obtain a more compact notation. Thus we write the equation of motion as

$$\begin{aligned} -\omega^2 m_i v_i + k_i v_i^{\mathrm{iv}} = & \\ -g_v \left(2v_i - v_{i+1} - v_{i-1}\right) + g_m & \left(2v_i'' - v_{i-1}'' - v_{i+1}''\right) \end{aligned} \tag{3.25}$$

and the internal shear force as

$$V_i = g_m \left(2v_i'' - v_{i-1}'' - v_{i+1}''\right) - k_i v_i''' \tag{3.26}$$

3.3.4 Variational Form

When developing approximate solutions to the eigenvalue problem posed by Eq. (3.25) with appropriate boundary conditions, we will find it convenient to work from a variational formulation. Multiplying Eq. (3.25) by the virtual displacement $\bar{v}_i$, integrating over the length of the beam, and summing over i, we obtain

$$\sum_i \int_0^1 \bar{v}_i \left(k_i v_i^{\mathrm{iv}} - \omega^2 m_i v_i\right) dx = \tag{3.27}$$
$$\sum_i \int_0^1 \bar{v}_i \left[g_m \left(2v_i'' - v_{i+1}'' - v_{i-1}''\right) - g_v \left(2v_i - v_{i+1} - v_{i-1}\right)\right] dx$$

Integration by parts yields the so-called weak form

$$\sum_i \int_0^1 \left(k_i \bar{v}_i'' v_i'' - \omega^2 m_i \bar{v}_i v_i\right) dx = \tag{3.28}$$
$$\sum_i \int_0^1 \left[g_m \bar{v}_i' \left(2v_i' - v_{i+1}' - v_{i-1}'\right) - g_v \bar{v}_i \left(2v_i - v_{i+1} - v_{i-1}\right)\right] dx +$$
$$\sum_i \left\{k_i \bar{v}_i' v_i'' - \bar{v}_i \left[k_i v_i''' - g_m \left(2v_i' - v_{i-1}' - v_{i+1}'\right)\right]\right\}_0^1$$

If we require that the virtual displacement $\bar{v}_i$ satisfy the geometric boundary conditions, we see that the boundary terms appearing in the preceding must vanish for non-energetic boundary conditions.

3.4 Solution Techniques

Our task now is to solve the eigenvalue problem posed by Equation (3.25) along with appropriate boundary conditions. Exact analytical solutions are attainable for only the simplest of boundary conditions, and we must in general resort either to approximate analytical solutions or to numerical methods. In the following, we describe three of the most useful approaches to eigenvalue problems of this type: direct numerical solution, modal discretization, and finite-element discretization.

3.4.1 Direct Solution

The governing equations (3.25) constitute a set of constant-coefficient, linear, homogeneous equations of order $4N$, where N is the number of elastic layers. Therefore, unless an eigenvalue and eigenvalue are repeated, the v_i will be of the form $A_i e^{\lambda x}$, where the A_i and λ are complex constants. If we substitute this form of solution into Eq. (3.25) we obtain the set of homogeneous algebraic equations

$$\left(g_v - \lambda^2 g_m\right) A_{i-1} + \left(k_i \lambda^4 - m_i \omega^2 + 2g_v - 2\lambda^2 g_m\right) + \left(g_v - \lambda^2 g_m\right) A_{i+1} = 0 \tag{3.29}$$

which can be assembled into a matrix equation of the form

$$\left[D_1(\omega^2, \lambda)\right] [A_i] = 0 \tag{3.30}$$

where the coefficient matrix $D_1(\omega^2, \lambda)$ yields a determinant of order $4N$ in the eigenvalue λ, so that for a given value of ω we can solve for the $4N$ values of λ that satisfy Eq. (3.25) and determine the eigenvectors A_i corresponding to each eigenvalue.

Denoting now the $4N$ eigenvalues and eigenvectors as λ_k and $A_i^{(k)}$ for $k = 1, 2, \ldots, 4N$, we can write the displacement $v_i(x)$ in the form

$$v_i(x) = \sum_{k=1}^{4N} V_k A_i^{(k)} e^{\lambda_k x} \tag{3.31}$$

where the V_k are complex constants. These displacements are required to satisfy $4N$ boundary conditions, which usually involve the $v_i(x)$ and their derivatives evaluated at the ends of the beam. If the boundary conditions are homogeneous, we can assemble them into the form

$$\left[D_2(\lambda_1, \lambda_2, \ldots, \lambda_{4N})\right] [V_k] = 0 \tag{3.32}$$

where the dependence of D_2 on the λ_k is usually transcendental. Our task then is to find the value of ω and corresponding λ_k and $A_i^{(k)}$ for which the determinants of the matrices D_1 and D_2 are zero.

The most common approach to solving such problems is a search method, wherein one guesses a value for ω and solves for the values of λ_k and $A_i^{(k)}$ which force determinant of D_1 to zero. Then the determinant of D_2 is evaluated to

check for convergence. If this determinant is not sufficiently close to zero, a new guess for ω is generated (most commonly using a Newton–Raphson approach), and the process is repeated.

This is the approach most often used in the literature for finding the resonant frequencies and damping ratios of vibration in the plane normal to lamination, and its success depends largely on the quality of the initial guess for ω and the details of the scheme of iteration. Several researchers have reported difficulties in obtaining convergence for cases with non-symmetric boundary conditions (e.g., Markus and Valaskova, 1972), but evidently these difficulties can be overcome with careful programming as reported in a paper by Rao (1977).

3.4.2 Classical Rayleigh-Ritz Discretization

The eigensolutions for vibration of Euler–Bernoulli beams with pinned, sliding, clamped, or free ends are well known and tabulated in many texts. Hence, for a composite beam with such boundary conditions, we find it convenient to expand the motion of the ith layer in the form

$$\bar{v}_i(x) = v_i(x) = \sum_r \psi_{ir}(x) a_{ir} \tag{3.33}$$

where the trial function ψ_{ir} is the rth eigenfunction of the ith layer if it is decoupled from the remaining layers and a_{ir} is the associated complex amplitude. For the boundary conditions of interest, the decoupled eigenvalue problem is self adjoint, and the eigenfunctions ψ_{ir} can be orthonormalized so that

$$\langle \psi_{ir}(x), \psi_{is}(x) \rangle = \delta_{rs} \tag{3.34}$$

where $\langle f(x), g(x) \rangle = \int_0^1 f(x)\, g(x)\, dx$ is the inner product over the length of the beam.

Noting that the series expansion in Eq. (3.33) satisfies the boundary conditions exactly, we substitute it into the weak variational form given by Eq. (3.28) and minimize the error by requiring the result to be stationary with respect to the a_{ns}. This process yields the following set of algebraic equations governing the a_{ns} for $n = 1, 2, 3 \ldots, N$ and $s = 1, 2, 3 \ldots$

$$-\omega^2 m_n a_{ns} + k_n \sum_r \langle \psi''_{nr}, \psi''_{ns} \rangle\, a_{nr} = \tag{3.35}$$

$$-g_v\left[2a_{ns}-\sum_r\left(\left\langle\psi_{ns},\psi_{(n+1)r}\right\rangle a_{(n+1)r}+\left\langle\psi_{ns},\psi_{(n-1)r}\right\rangle a_{(n-1)r}\right)\right]$$
$$+g_m\sum_r\left[2\left\langle\psi'_{ns},\psi'_{nr}\right\rangle a_{nr}-\left\langle\psi'_{ns},\psi'_{(n+1)r}\right\rangle a_{(n+1)r}-\left\langle\psi'_{ns},\psi'_{(n-1)r}\right\rangle a_{(n-1)r}\right]$$

The various inner products involving the ψ_{ns} and their derivatives can be evaluated analytically or numerically. In many cases it will prove convenient to integrate by parts in order to express the inner products in terms of the boundary values. Some useful results of this type are derived in Appendix 3.7.

3.4.3 Finite-Element Discretization

For general boundary conditions, it is difficult to guess a set of global trial functions which give rapid convergence, and we therefore find it useful to discretize locally by the finite-element method. We now treat the sandwich beam of Eqs. (3.28) as one element of a longer beam and approximate the deflection of the ith layer of this element as a cubic polynomial of the form

$$v_i(x)=p_{i1}+p_{i2}x+p_{i3}x^2+p_{i4}x^3 \tag{3.36}$$

We require that the displacement and slope at the end of each layer of the element match that in the adjoining element, so it is convenient to rewrite the expansion for $v_i(x)$ in terms of the displacements and slopes at the ends of the element. That is,

$$v_i(x)=\phi_1(x)q_{i1}+\phi_2(x)q_{i2}+\phi_3(x)q_{i3}+\phi_4(x)q_{i4} \tag{3.37}$$

where

$$q_i=\begin{bmatrix} v_i(0)\\ v_i'(0)\\ v_i(1)\\ v_i'(1)\end{bmatrix} \tag{3.38}$$

and the interpolation functions ϕ_i are given by

$$\phi_1(x) = 1-3x^2+2x^3 \tag{3.39}$$
$$\phi_2(x) = x-2x^2+x^3 \tag{3.40}$$
$$\phi_3(x) = 3x^2-2x^3 \tag{3.41}$$
$$\phi_4(x) = -x^2+x^3 \tag{3.42}$$

Substituting this expansion into the weak form (3.28) and requiring that it be stationary with respect to the q_{ns}, we obtain the set of equations

$$-\omega^2 m_n \sum_{r=1}^{4} \langle \phi_r, \phi_s \rangle q_{nr} + k_n \sum_{r=1}^{4} \langle \phi_r'', \psi_s'' \rangle q_{nr} = \tag{3.43}$$
$$-\sum_{r=1}^{4} \left(g_v \langle \phi_r, \phi_s \rangle - g_m \langle \phi_r', \phi_s' \rangle \right) \left(2q_{nr} - q_{(n+1)r} - q_{(n-1)r} \right)$$

which we write in matrix from as

$$\left(K_n - \omega^2 M_n + 2G_v - 2G_m \right) q_n - (G_v - G_m)(q_{n+1} + q_{n-1}) = 0 \tag{3.44}$$

where the elements of the component matrices are defined as

$$(M_n)_{ij} = m_n \langle \phi_i, \phi_j \rangle \tag{3.45}$$
$$(K_n)_{ij} = k_n \left\langle \phi_i'', \phi_j'' \right\rangle \tag{3.46}$$
$$(G_v)_{ij} = g_v \langle \phi_i, \phi_j \rangle \tag{3.47}$$
$$(G_m)_{ij} = g_m \left\langle \phi_i', \phi_j' \right\rangle \tag{3.48}$$

The mass matrix M_n and the stiffness matrix K_n are identical to the mass and stiffness matrices from the standard cubic beam element:

$$M_n = \frac{m_n}{420} \begin{bmatrix} 156 & 22 & 54 & -13 \\ 22 & 4 & 13 & -3 \\ 54 & 13 & 156 & -22 \\ -13 & -3 & -22 & 4 \end{bmatrix} \tag{3.49}$$

$$K_n = k_n \begin{bmatrix} 12 & 6 & -12 & 6 \\ 6 & 4 & -6 & 2 \\ -12 & -6 & 12 & -6 \\ 6 & 2 & -6 & 4 \end{bmatrix} \tag{3.50}$$

The force coupling matrix G_v can be obtained from the mass matrix by multiplying it by the scalar g_v/m_n for some particular value of n. We compute the moment coupling matrix G_m from its definition in Eq. (3.48) to be

$$G_m = \frac{g_m}{30} \begin{bmatrix} 36 & 3 & -36 & 3 \\ 3 & 4 & -3 & -1 \\ -36 & -3 & 36 & -3 \\ 3 & -1 & -3 & 4 \end{bmatrix} \tag{3.51}$$

3.5 Examples

3.5.1 Simple Supports

In this section, we examine the dynamics of the sandwich beam for the particular case of a symmetric five-layer laminate where each of the principal and constraining layers is simply supported. For this set of boundary conditions, we find it convenient to employ a classical Rayleigh–Ritz discretization.

Designating the second elastic layer to be the principal layer, we have $m_2 = k_2 = 1$. Because the laminate is symmetric, $m_1 = m_3 = m$ and $k_1 = k_3 = k$. Moreover, because each of the elastic layers is simply supported, the decoupled eigenfunctions are

$$\psi_{1r}(x) = \psi_{2r}(x) = \psi_{3r}(x) = \phi_r(x) = \sqrt{2}\sin r\pi x \tag{3.52}$$

and the corresponding eigenvalues are $\lambda_r = (r\pi)^4$. Hence, the discretized equations given in Eq. (3.35) can be written in the form

$$\begin{aligned} -\omega_r^2 m a_{1r} + k\sum_s \langle \phi_r'', \phi_s'' \rangle a_{1s} &= -g_v a_{1r} + g_v \sum_s \langle \phi_r, \phi_s \rangle a_{2s} \\ &\quad - g_m \sum_s [\langle \phi_r', \phi_s' \rangle a_{1s} - \langle \phi_r', \phi_s' \rangle a_{2s}] \end{aligned} \tag{3.53}$$

$$\begin{aligned} -\omega_r^2 a_{2r} + \sum_s \langle \phi_r'', \phi_s'' \rangle a_{2s} &= -2g_v a_{2r} + g_v \sum_s \langle \phi_r, \phi_s \rangle (a_{1s} + a_{3s}) \\ &\quad - g_m \sum_s [\langle \phi_r', \phi_s' \rangle a_{2s} - \langle \phi_r', \phi_s' \rangle (a_{2s} + a_{3s})] \end{aligned} \tag{3.54}$$

$$\begin{aligned} -\omega_r^2 m a_{3r} + k\sum_s \langle \phi_r'', \phi_s'' \rangle a_{3s} &= -g_v a_{3r} + g_v \sum_s \langle \phi_r, \phi_s \rangle a_{2s} \\ &\quad - g_m \sum_s [\langle \phi_r', \phi_s' \rangle a_{3s} - \langle \phi_r', \phi_s' \rangle a_{2s}] \end{aligned} \tag{3.55}$$

Using the results derived in Appendix 3.7, we reduce the system of ordinary-differential equations (3.53)–(3.55) to

$$-\omega_r^2 m a_{1r} + k(r\pi)^4 a_{1r} = -\Gamma (a_{1r} - a_{2r}) \tag{3.56}$$

$$-\omega_r^2 a_{2r} + (r\pi)^4 a_{2r} = -\Gamma (2a_{2r} - a_{1r} - a_{3r}) \tag{3.57}$$

$$-\omega_r^2 m a_{3r} + k(r\pi)^4 a_{3r} = -\Gamma (a_{3r} - a_{2r}) \tag{3.58}$$

where

$$\Gamma = g_v + g_m (r\pi)^2 \tag{3.59}$$

from which we see that the rth coordinates are decoupled from the sth coordinates for any $s \neq r$. Thus, corresponding to the rth mode of a decoupled simply supported beam, we have three modes of the composite beam, for which each layer deflects in the shape of the rth mode of a simply supported uniform beam.

Hence, for a given wavenumber r, the motion of a composite beam on simple supports can be modeled using the lumped parameter model shown in Fig. 3.2. In Eqs. (3.56)–(3.58), the effective stiffness of the viscoelastic layers is measured by the parameter Γ, which we see from Eq. (3.59) is made up of a linear combination of the displacement-coupling parameter g_v and the slope-coupling parameter g_m. Recalling from Eq. (3.22) that $g_m = g_v(h^2/3L^2)$, we see that g_m can often be neglected for low-wavenumber modes.

The eigenvalue problem given by Eqs. (3.56)–(3.58) is symmetric and hence admits two types of solution: antisymmetric modes with $a_{1r} = -a_{3r}$ and $a_{2r} = 0$ that satisfy

$$\omega_r^2 = \frac{\Gamma + k(r\pi)^4}{m} \tag{3.60}$$

and symmetric modes with $a_{1r} = a_{3r}$ that satisfy

$$\begin{aligned} m\omega_r^4 - \left[\Gamma(1+2m) + (r\pi)^4(k+m)\right]\omega_r^2 \\ + \left[\Gamma(r\pi)^4(1+2k) + k(r\pi)^8\right] = 0 \end{aligned} \tag{3.61}$$

and

$$\left[\Gamma + k(r\pi)^4 - m\omega_r^2\right] a_{1r} = \Gamma a_{3r} \tag{3.62}$$

Modeling the behavior of the viscoelastic material as frequency-independent hysteretic, we set its complex shear modulus to $G = G_v(1 + j\eta_v)$, where η_v is the loss factor of the viscoelastic material. Since Γ is proportional to G, we can write

$$\Gamma = \Gamma_r(1 + j\eta_v) \tag{3.63}$$

For nonzero η_v, the resonant frequencies ω_r are complex, and the loss factor η of the composite beam is given by the ratio of the imaginary and real parts of the square of ω_r:

$$\eta = \frac{\mathrm{Im}(\omega_r^2)}{\mathrm{Re}(\omega_r^2)} \tag{3.64}$$

In the following, we will discuss the effects of varying Γ_r and k for composite beams with lossy viscoelastic ($\eta_v = 1$) and constraining layers each with one-tenth the mass of the principal layer ($m = 0.1$).

For the case where $k/m = 1$ (where the natural frequencies of the decoupled principal and constraining layers are equal), the resonant frequencies are

$$\omega_r^2 = \left\{ (r\pi)^4 \ , \ (r\pi)^4 + \frac{\Gamma}{m} \ , \ (r\pi)^4 + \frac{\Gamma}{m}(1+2m) \right\} \tag{3.65}$$

from which we see that the first resonant frequency of the composite beam is equal to that of the individual layers and has $\eta = 0$. The principal mode in this case involves synchronous motion of the elastic layers of the beam. The two higher resonances are well damped for large η_v and Γ.

Next, we consider the case where $k/m > 1$ so that the natural frequencies of the decoupled constraining layers are higher than those of the principal layer. The resonant frequencies and loss factors are plotted as a function of Γ_r in Fig. 3.8. The two higher resonances are well damped for all but very low values of Γ_r. One of these resonances involves antisymmetric motion of the constraining layers and no motion of the principal layer, while the other involves symmetric motion of the constraining layers and relatively little motion of the principal layer.

Of greater practical interest is the first resonance, which involves large motion of the principal layer. The damping follows a trend similar to that observed for the planar shear damping mechanism: For small Γ_r, the principal and constraining layers are weakly coupled and large shear strains but little strain energy is imparted to the viscoelastic layers. For large Γ_r, the constraining layers are entrained to the principal layer and little shear strain occurs in the viscoelastic layers. Between these extremes, there exists a range of Γ_r over which significant damping (η as high as 0.09) can be obtained.

When $k/m < 1$, the natural frequencies of the decoupled constraining layers are lower than those of the principal layer. Consequently, as Γ_r is increased from a very low value (assuming $m < 0.5$), the two resonances given by Eq. (3.61) cross over as shown in Fig. 3.9. Near this crossover region, the behavior resembles that of a tuned-mass damper and loss factors greater than 0.2 can be obtained for all three resonances. These results bear some similarity to those found by Douglas and Yang (1978) who found that significant damping arises due to relative transverse motion of the face layers of a three-layer sandwich beam near its transverse compressional frequency. This behavior can be described as distributed tuned-mass damping, which was recently studied by Zapfe and Lesieutre (1996).

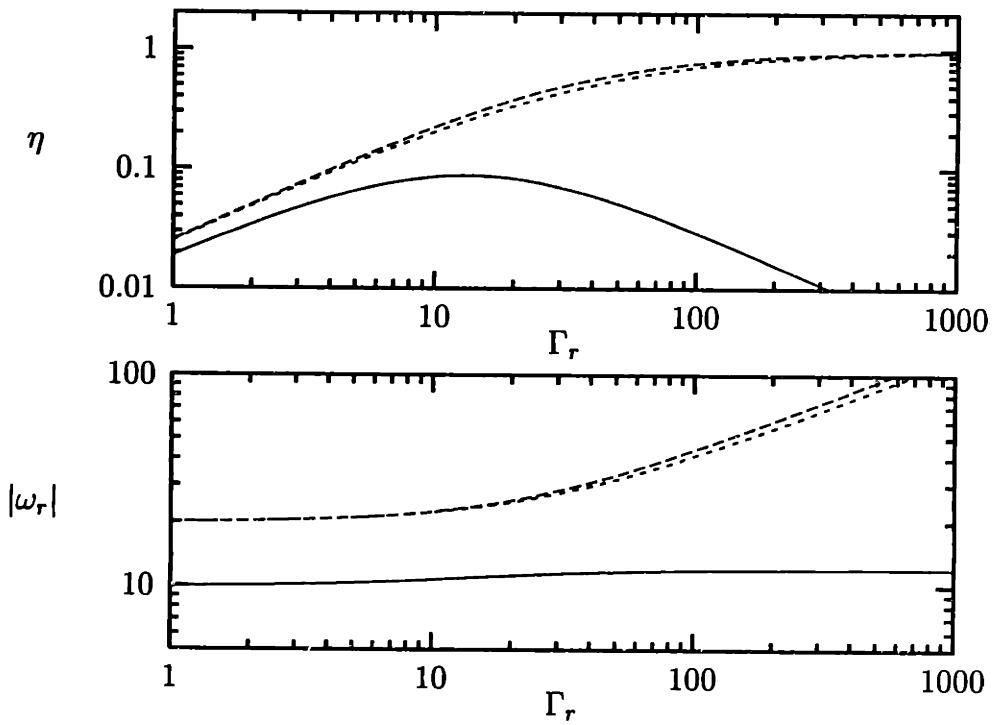

Figure 3.8 Resonant frequencies and composite loss factors as a function of the real part of Γ for vibration in the plane of lamination of a five-layer symmetric laminate for $r = 1$, $\eta_v = 1.0$, $m = 0.1$, and $k/m = 4$. All layers of the beam are simply supported.

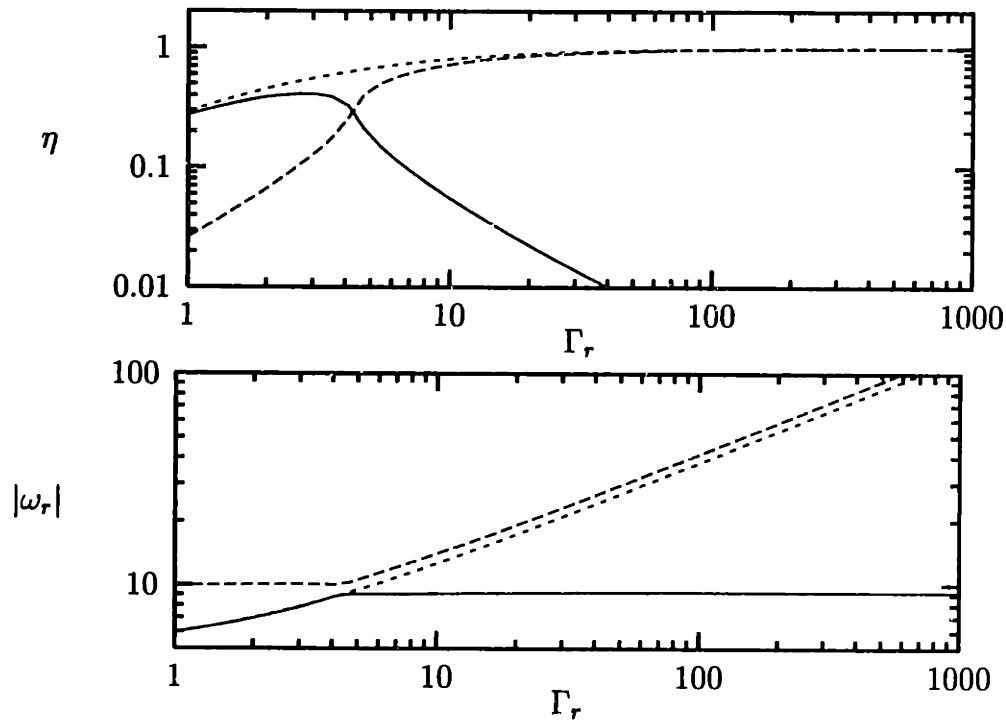

Figure 3.9 Resonant frequencies and composite loss factors as a function of the real part of Γ for vibration in the plane of lamination of a five-layer symmetric laminate for $r = 1$, $\eta_v = 1.0$, $m = 0.1$, and $k/m = 0.25$. All layers of the beam are simply supported.

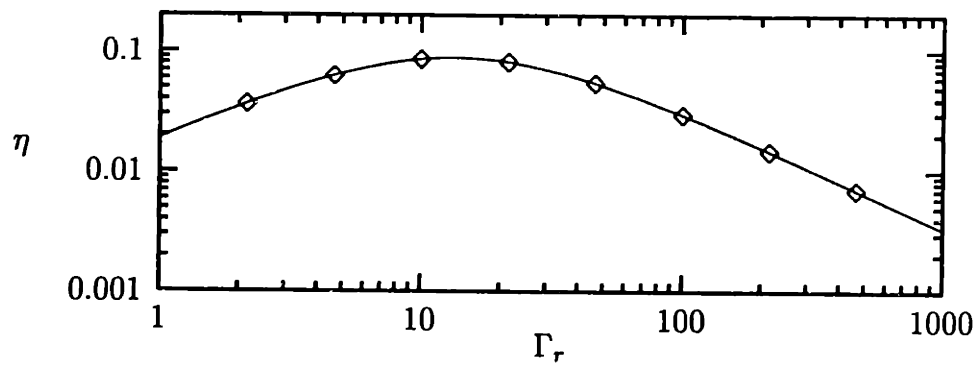

Figure 3.10 Comparison of finite-element results (diamonds) to the exact solution (line) for the loss factor of the principal mode of vibration in the plane of lamination of a five-layer symmetric laminate with $\eta_v = 1.0$, $m = 0.1$, and $k/m = 4$. All layers of the beam are simply supported.

Validation of Finite-Element Code

Before moving on to laminates with other boundary conditions, it is worthwhile to validate our finite-element code against the exact solutions for simply supported laminates. Following the formulation given in Section 3.4.3, we developed a program for computation of the complex eigenvalues of laminated sandwich beams. Because we are interested in only the principal resonance of a symmetric laminate, we can lump both constraining layers into a single layer with twice the mass stiffness.

The exact solution was found to depend on the properties of the viscoelastic layer only through the parameter Γ, which is defined in Eq. (3.59) to be a linear combination of the displacement- and slope-coupling parameters g_v and g_m. Setting $g_m = 0$ so that $\Gamma = g_v$, using the same parameter values as in Fig. 3.8, and segmenting the composite beam into six elements, we obtain the results shown in Fig. 3.10. The error in the finite-element approximation to the loss factor is everywhere less than 0.1 per cent. Nearly identical results (to within 0.02 per cent) are obtained with $g_v = 0$ so that $\Gamma = \pi^2 g_m$.

3.5.2 Pinned and Free Ends

We now consider vibration in the plane of lamination of a five-layer symmetric sandwich beam whose principal layer is simply supported but whose constraining layers are free. Because the decoupled mode shapes of the principal and constraining layers are different, a classical Rayleigh-Ritz expansion will require several terms in order to converge, and we choose at present to use the finite-element formulation given in Section 3.4.3.

As in Section 3.5.1, we consider a beam whose two constraining layers are each one-tenth the mass of the principal layer and whose viscoelastic layers have loss factor $\eta_v = 1$. We are concerned with only the lowest few modes of the beam and hence we neglect the slope coupling g_m and plot the resonant frequencies and loss factors as functions of the real part of the displacement coupling parameter g_v. Moreover, because the antisymmetric modes of the laminate involve no motion of the principal layer, we solve for only its symmetric modes.

Let us first consider the case where the constraining layers have a higher stiffness per unit mass than the principal layer. The resonant frequency and loss factor of the first six symmetric modes of the laminate vary with $\mathrm{Re}(g_v)$ as shown in Fig. 3.11. For very small g_v the principal and constraining layers of the beam behave as if they are decoupled: the resonant frequencies correspond to those of the individual layers, and the loss factors approach zero. The solutions along the branches labeled *a* and *b* in Fig. 3.11 correspond, respectively, to rigid-body translation and rotation of the constraining layers. Branches *c*, *d*, and *f* correspond to the first three modes of the simply supported principal layer. Branch *e* represents the first flexural mode of the constraining layers.

For very large g_v, the principal and constraining layers behave as if they are rigidly coupled. The resonant frequencies are those of a simply supported beam with normalized flexural stiffness $1+2k$ and mass per unit length $1+2m$. Thus, branches *g* through *l* correspond to the first six flexural modes of a simply supported beam.

Consider the principal mode, which at low g_v corresponds to branch *c*. As g_v is increased from roughly 1 to 7, the resonant frequency increases very slowly but the loss factor goes from less than 10^{-3} to greater than 0.3. At $g_v \approx 7$, this eigenvalue coalesces with that of the rigid-body mode of branch *a* and the branches *g* and *m* are born. On the plot of $\log|\omega|$ versus $\log g_v$, the branch *m* lies approximately on a straight line along which the frequency

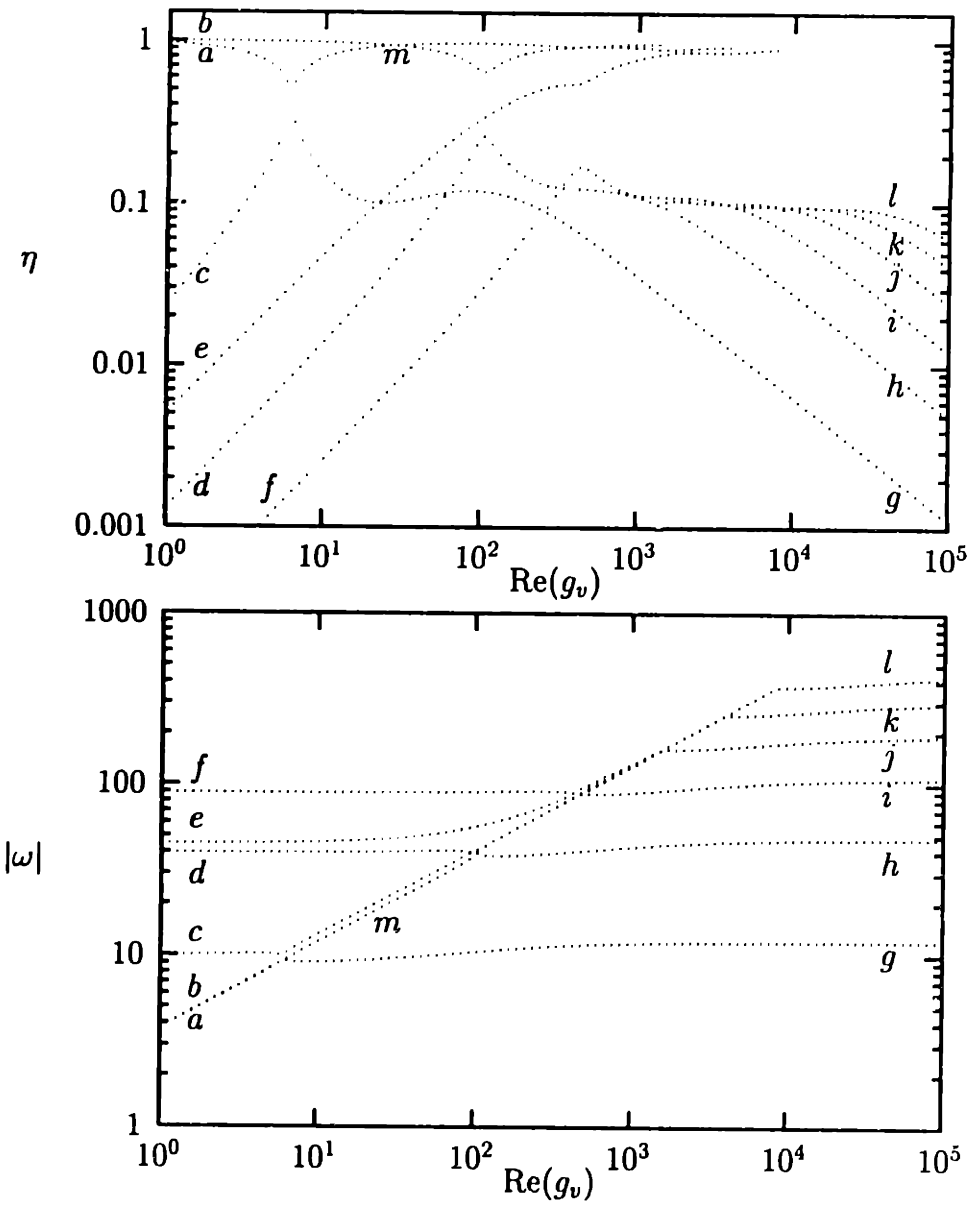

Figure 3.11 Resonant frequency and loss factor of the first six symmetric modes of vibration in the plane of lamination of a symmetric five-layer laminate: The principal layer is simply supported and the constraining layers are free, $m = 0.1$, $k/m = 4$, $\eta_v = 1$, and $g_m = 0$.

increases rapidly with g_v and the loss factor approaches unity. At $g_v \approx 700$ branch m ends and gives rise to branch i.

The response to a low-frequency disturbance is determined primarily by the resonant frequency and loss factor along the branches c and g. The highest damping is obtained at their intersection (at $\mathrm{Re}(g_v) \approx 7$) where $\eta \approx 0.3$ and $|\omega| \approx 10$. However, the damping near this intersection is very sensitive to changes in g_v and the damping along branch $\tilde{d}$ is very light. It may therefore be advantageous to choose designs with $\mathrm{Re}(g_v)$ between 50 and 200, where the loss factor along both branches g and d are both greater than 0.1.

Next, consider the case where the constraining layers have lower stiffness per unit mass than the principal layer. The resonant frequencies and loss factors obtained from the finite-element model for the case $k/m = 0.25$ are plotted in Fig. 3.12. The maximum damping of the principal mode in this case is comparable to that shown in Fig. 3.11 for the case $k/m = 4$, but it is attainable over a very narrow range of g_v. Moreover, whereas for $k/m = 4$ loss factors greater than 0.1 can be obtained along the branch g for values of $\mathrm{Re}(g_v)$ between 7 and 200, the loss factor in this case falls to below 0.1 at $\mathrm{Re}(g_v) = 11$.

We have seen in Section 3.5.1 that, when each elastic layer of the beam is simply supported, significant damping of the principal modes can be obtained only if the principal and constraining layers are detuned. But if the boundary conditions differ, then the principal modes are well damped (for appropriately chosen g_v) even for perfectly tuned principal and constraining layers. In Fig. 3.13, we plot the first six resonant frequencies and loss factors of a "perfectly tuned" ($k/m = 1$) laminate whose principal layer is simply supported but whose constraining layers are free. The damping behavior in this case is comparable to that found for the case $k/m = 0.25$.

3.5.3 Free Ends

Let us now consider free-free vibration in the plane of lamination of the ceramic-viscoelastic beam with the cross section shown in Fig. 3.14. The principal layer is a box beam composed of 96 per cent alumina ceramic with Young's modulus $E_1 = 311$ GPa and the constraining layers are 99.5 per cent aluminum oxide with $E_2 = 372$ GPa. The viscoelastic layers are each 0.25 mm thick and composed of EAR-C1002, which at 2000 Hz and room temperature has complex modulus $G_v = 13.9(1 + j0.95)$ MPa. The endpoint receptance

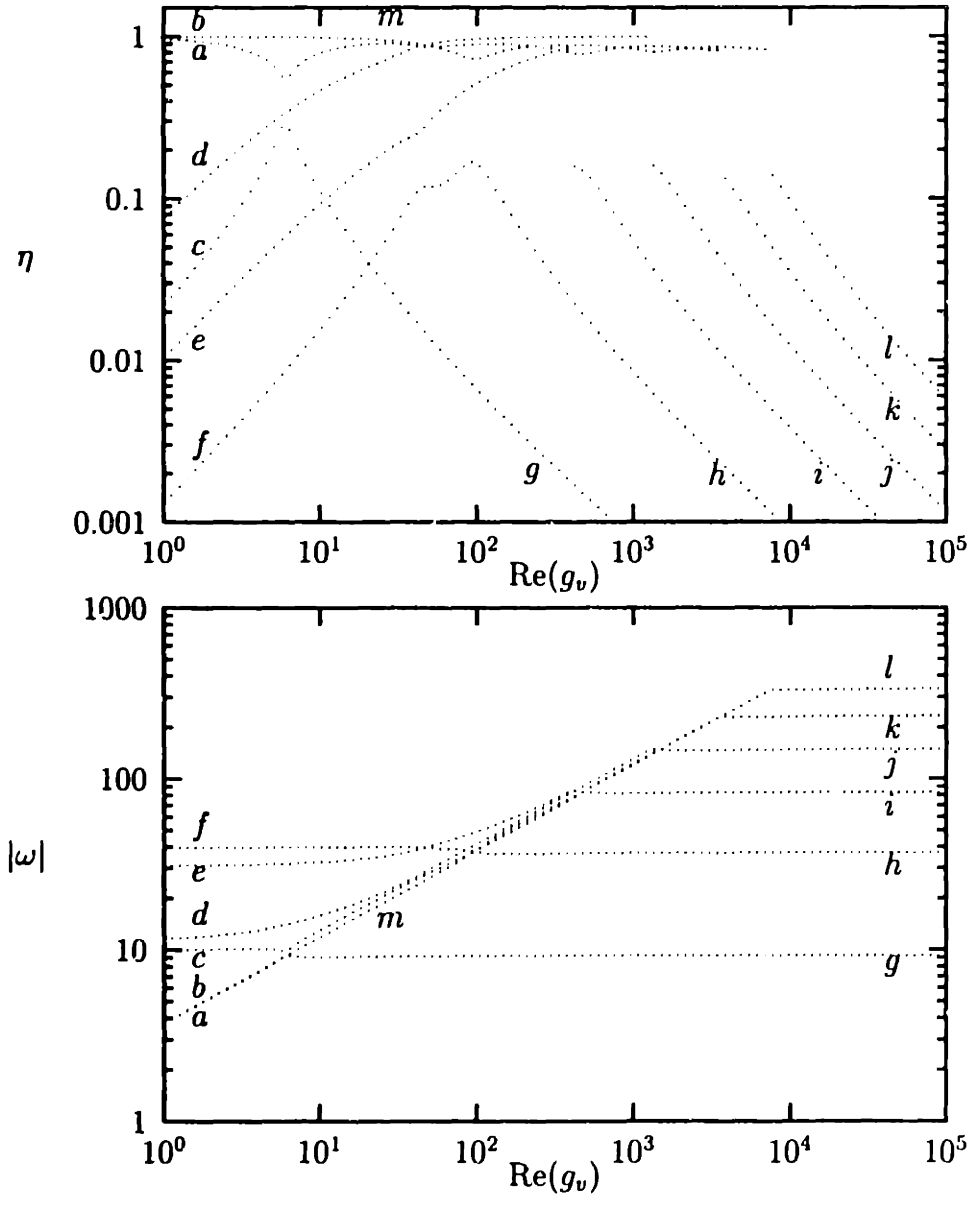

Figure 3.12 Resonant frequency and loss factor of the first six symmetric modes of vibration in the plane of lamination of a symmetric five-layer laminate: The principal layer is simply supported and the constraining layers are free, $m = 0.1$, $k/m = 0.25$, $\eta_v = 1$, and $g_m = 0$.

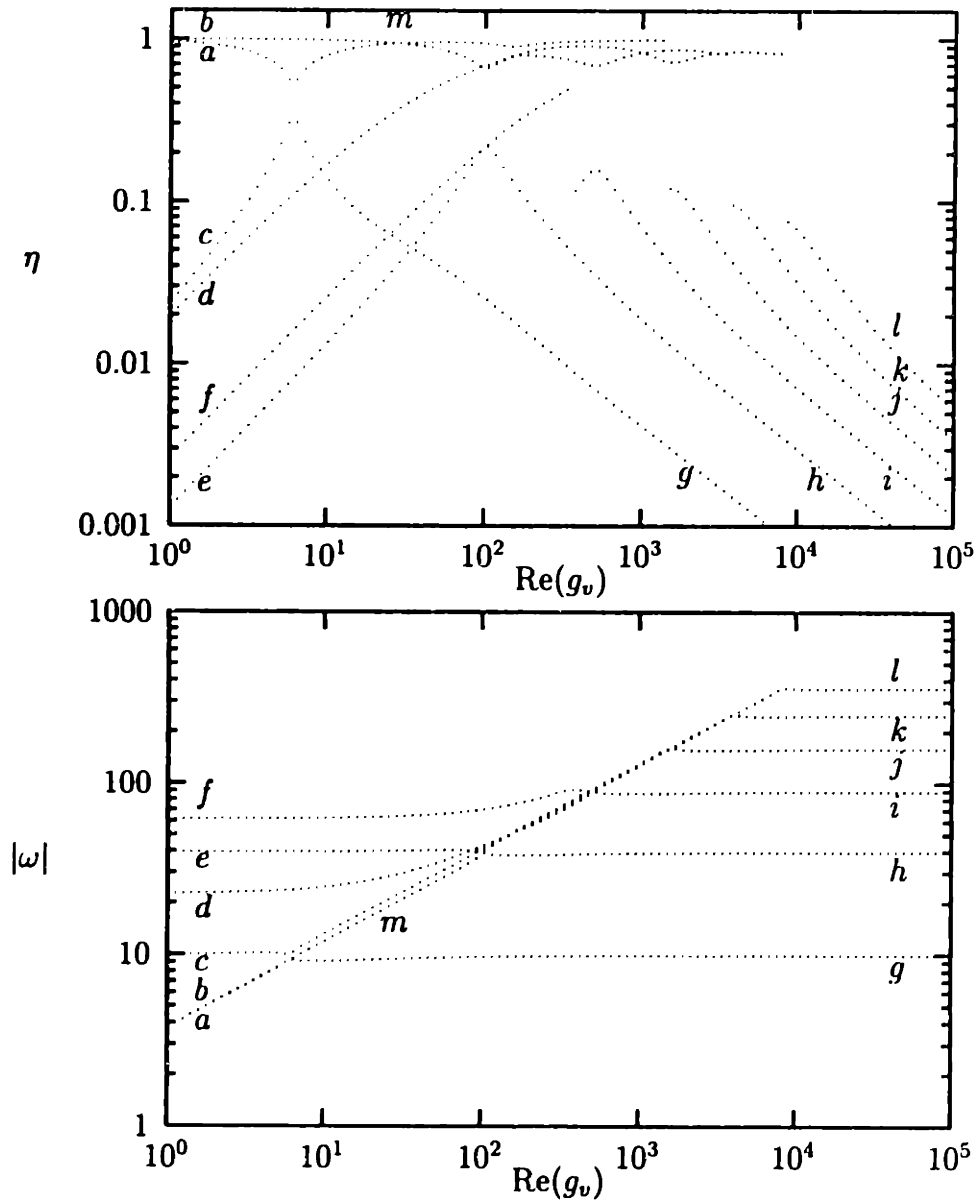

Figure 3.13 Resonant frequency and loss factor of the first six symmetric modes of vibration in the plane of lamination of a symmetric five-layer laminate: The principal layer is simply supported and the constraining layers are free, $m = 0.1$, $k/m = 1$, $\eta_v = 1$, and $g_m = 0$.

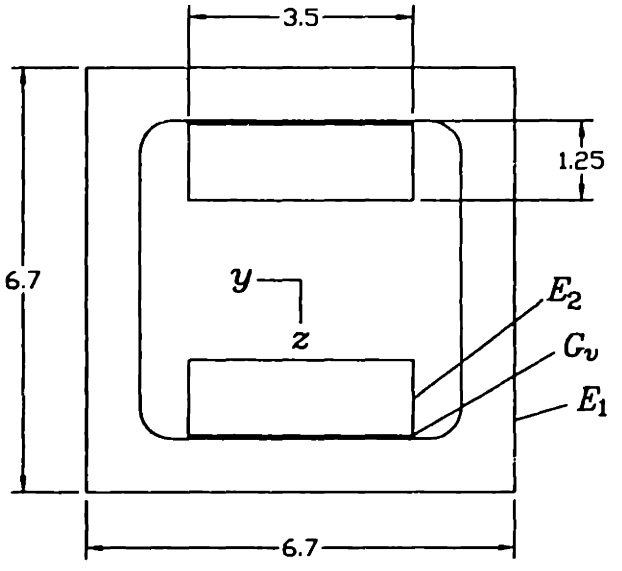

Figure 3.14 Cross section of a ceramic box beam with constrained viscoelastic layers: The beam is 0.914 m long and is composed of a principal layer with $E_1 = 311$ GPa, constraining layers with $E_2 = 372$ GPa, and viscoelastic layers with $G_v = 13.9(1 + j0.95)$ MPa and thickness 0.25 mm. Dimensions are in cm.

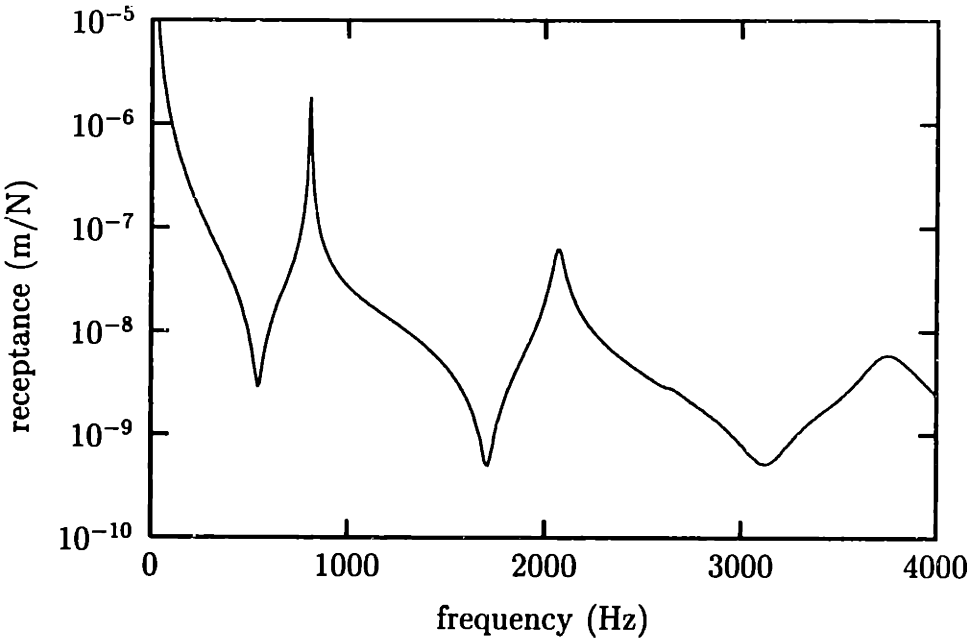

Figure 3.15 Measured endpoint receptance in the plane of lamination of the ceramic beam of Fig. 3.14: A free-free condition was approximated by suspending the beam with light surgical tubing.

measured in the y direction of the composite beam is plotted in Fig. 3.15.

In terms of our nondimensional parameters, the ceramic laminate has $m = 0.25$, $k = 0.055$, $\eta_v = 0.95$, and $g_v = 2160(1 + j0.95)$. The slope coupling g_m in this case is equal to $g_v/2000$ and can be safely ignored for the lowest several modes of the beam. The results of a finite-element calculation for these parameter values compare to the measured data as follows:

frequency (Hz)		loss factor	
measured	predicted	measured	predicted
808	795	0.007	0.004
2065	2103	0.036	0.034
3730	3800	0.103	0.141

The considerable error in the prediction of the loss factor of the first and third modes is probably due to the variation of the viscoelastic material properties with frequency. We use the material properties corresponding for 2000 Hz in

our calculations although the shear modulus of the viscoelastic material (EAR C-1002) more than doubles as the frequency increases from 1000 to 3000 Hz. Moreover, according to Eq. (3.1), the displacement-normalized twist between elastic layers under symmetric motion is of order a/h, where a is half the thickness of the constraining layer and h is half its width. For the beam under consideration $a/h = 0.36$ so we can't expect the model to predict the damping very accurately with such thick constraining layers.

It is perhaps interesting to see what damping (according to the model) would be achievable by adjusting g_v. In Fig. 3.16, we plot the resonant frequencies and loss factors of the beam as a function of the real part of g_v. From the plot, it is apparent that loss factors of better than 0.3 for any one mode could be achieved with proper selection of g_v, and that the current design with $g_v = 2160(1+j0.95)$ is probably most effective for damping the third and fourth modes. A more compliant viscoelastic layer would yield better damping of the first two modes.

3.5.4 Free Ends with Segmented Layers

Let us now consider a free-free beam with the cross section shown in Fig. 3.17, where the principal and constraining layers are solid aluminum bars. The stiffness per unit mass in the principal and constraining layers are equal so that $k/m = 1$ and we expect to obtain very little damping of the principal modes. The measured receptance is shown using a dotted line in Fig. 3.18; a least-squares curve fit to the resonant peaks indicates that η is less than 0.001 for the first two modes. Next, we segmented the constraining layers by making a transverse cut at the midpoint of the beam and repeated the measurement. The result is plotted with a solid line in Fig. 3.18, from which we see that segmenting the constraining layers has caused a dramatic increase in the damping. In addition, we see that whereas the resonant frequency of the first mode has dropped, that of the second mode has increased.

Using a finite-element model with ten elements, we obtain the plot of resonant frequency and loss factor as a function of g_{vr} shown in Fig. 3.19. The viscoelastic layer in the sample is composed of $EARC$ – 3102 damping foam, which at room temperature and 500 Hz, has $G_v = 0.1(1 + j1.0)$ MPa. Each viscoelastic layer is 0.25 inches thick; hence for our sample we have $g_v = 60(1 + j1.0)$. The results of the computation compare to curve-fitted experimental data as follows:

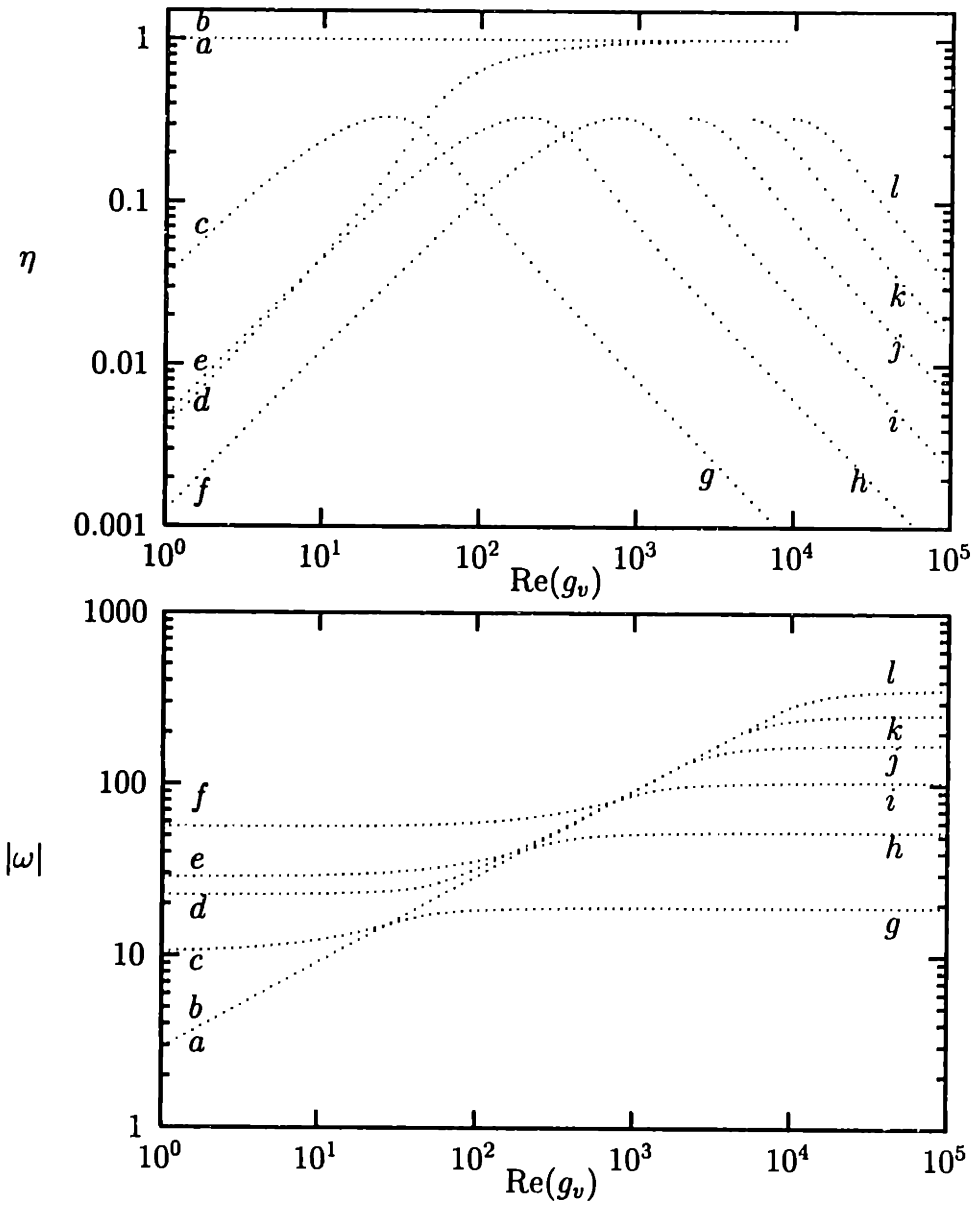

Figure 3.16 Resonant frequency and loss factor of the first six symmetric modes of vibration in the plane of lamination of the ceramic laminate of Fig. 3.14: The principal layer constraining layers have free ends, $m = 0.25$, $k/m = 0.22$, $\eta_v = 0.95$, and $g_m = 0$.

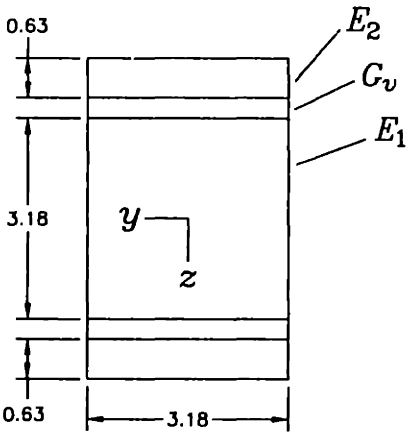

Figure 3.17 Cross-section of an aluminum sandwich beam: The beam is 0.914 m long, and made up of solid aluminum bars bonded with a thin layer of epoxy to the intervening layers of EAR C-3102 damping foam. Dimensions are in cm.

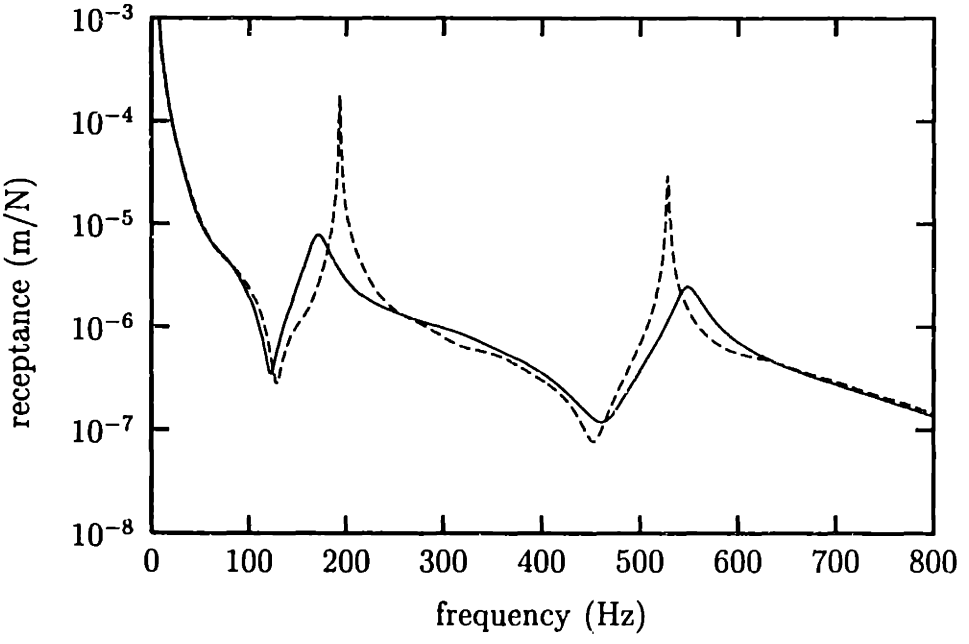

Figure 3.18 Comparison of measured receptances for the sandwich beam of Fig. 3.17 with contiguous (dashed line) and segmented (solid line) constraining layers.

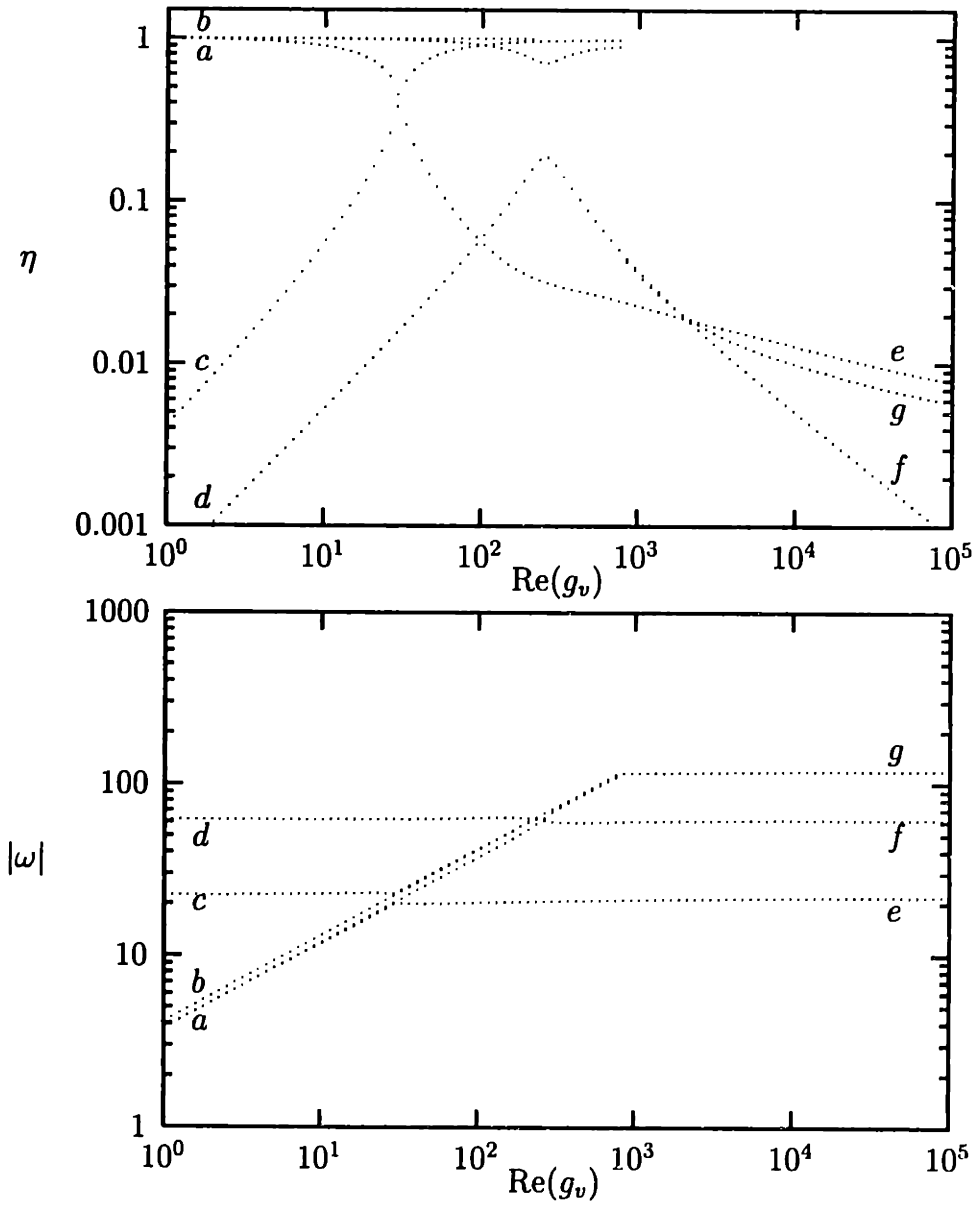

Figure 3.19 Resonant frequency and loss factor for the first several symmetric modes of vibration in the plane of lamination of a symmetric five-layer laminate: The constraining layers are segmented at the midpoint of the beam, all ends are free, $m = 0.1$, $k/m = 1$, $\eta_v = 1$, and $g_m = 0$.

frequency (Hz)		loss factor	
measured	predicted	measured	predicted
170	175	0.092	0.103
547	550	0.040	0.035

The agreement between the predicted and measured values is about as good as can be expected without taking into account the variation of the properties of the viscoelastic material with frequency.

3.6 Discussion

In this chapter, we have developed a model for vibration in the plane of lamination of elastic-viscoelastic beams. The model is based on the assumption that the angle of twist in each of the elastic layers is negligible, and hence is most accurate for beams with thin constraining layers mounted on opposing faces of a principal layer. According to the model, the damping in the composite beam depends on the mass ratio m, the stiffness ratio k, the coupling parameters g_v and g_m, and the boundary conditions on the various layers. For the lowest several modes of a slender beam, the slope coupling g_m can be neglected in comparison to g_v.

If the boundary conditions on the elastic layers are identical, the system behavior can be adequately modeled using a lumped parameter model such as shown in Fig. 3.2, and the behavior can be divided into three cases according to the tuning between the elastic layers: If the principal and constraining layers have the same stiffness per unit length, the principal mode is essentially undamped for any value of g_v. If the constraining layers have a higher stiffness per unit length than the principal layer, their inertia plays only a small role in the dynamics, and the behavior as g_v is varied follows the pattern of the parallel-stack damper of Fig. 2.1(c). On the other hand, if the constraining layers have a lower stiffness per unit length than the principal layer, the constraining layers can act as distributed tuned-mass dampers for some range of g_v.

If the boundary conditions on the principal and constraining layers differ, the variation of the resonant frequencies and damping ratios with changes in g_v are somewhat more complicated than can be captured with a lumped-parameter model. Because the mode shapes of the decoupled principal and constraining layers differ, the coupling forces are not distributed over the length

of a layer in proportion to its decoupled mode shape, and the constraining layers can present to the principal layer a distributed impedance far higher than its lumped stiffness. Hence the potential exists for damping significantly higher than in beams where the boundary conditions on the principal and constraining layers are identical.

3.7 Appendix: Evaluation of Various Inner Products

We wish to evaluate the inner products $\langle \phi_r', \phi_s' \rangle$ and $\langle \phi_r'', \phi_s'' \rangle$ where ϕ_r and λ_r satisfy the self-adjoint eigenproblem given by

$$\phi^{\mathrm{iv}}(x) = \lambda \phi(x) \quad x \in [0,1] \tag{3.66}$$

with suitable boundary conditions. The eigenfunctions ϕ_r are normalized so that $\langle \phi_r, \phi_s \rangle = \delta_{rs}$.

Using Eq. (3.66) we write the identity

$$\lambda_r \int_0^1 \phi_r' \phi_s' \, dx = \int_0^1 \phi_r^{\mathrm{v}} \phi_s' \, dx \tag{3.67}$$

and integrate twice by parts to obtain

$$\lambda_r \int_0^1 \phi_r' \phi_s' \, dx = \left[\phi_r^{\mathrm{iv}} \phi_s' - \phi_r''' \phi_s'' \right]_0^1 + \int_0^1 \phi_r''' \phi_s''' \, dx \tag{3.68}$$

Interchanging the indices and subtracting, we obtain

$$(\lambda_r - \lambda_s) \int_0^1 \phi_r' \phi_s' \, dx = \left[\lambda_r \phi_r \phi_s' - \lambda_s \phi_r' \phi_s - \phi_r''' \phi_s'' + \phi_s'' \phi_r''' \right]_0^1 \tag{3.69}$$

where we have again made use of Eq. (3.66). For a simply supported beam, each of the terms on the right-hand side of this equation vanishes and we conclude that $\langle \phi_r', \phi_s' \rangle = 0$ when $r \neq s$. For a free-free beam, the terms involving ϕ and ϕ' are not zero at the ends, but their total contribution is zero due to the symmetry of the problem; therefore, $\langle \phi_r', \phi_s' \rangle = 0$ when $r \neq s$. This inspectional approach can be used with some success for other simple and symmetric boundary conditions, but more difficult problems are often more easily handled numerically.

We follow a similar approach to evaluate $\langle \phi_r'', \phi_s'' \rangle$ in terms of the boundary values. In this case we begin with the identity

$$\lambda_r \delta_{rs} = \lambda_r \int_0^1 \phi_r \phi_s \, dx = \int_0^1 \phi_r^{\text{iv}} \phi_s \, dx \tag{3.70}$$

and integrate twice by parts to obtain

$$\lambda_r \delta_{rs} = [\phi_r''' \phi_s - \phi_r'' \phi_s']_0^1 + \int_0^1 \phi_r'' \phi_s'' \, dx \tag{3.71}$$

from which we conclude that $\langle \phi_r'', \phi_s'' \rangle = \lambda_r \delta_{rs}$ for simply supported, free-free, and cantilever beams.

CHAPTER 4

Torsion of Elastic-Viscoelastic Beams

In this chapter, we take up the problem of damping torsional vibration in slender beams. Assuming that the deformation obeys the Saint-Venant hypotheses, we develop a model suitable for predicting the complex stiffness per unit length in closed, thin-walled, elastic-viscoelastic tubes. We begin by studying the deformation of a closed tube formed from elastic shells joined by one or more viscoelastic seams running the length of the tube, derive an expression for the complex stiffness, and find that the damping behavior depends on a single dimensionless parameter. We then consider tubes whose walls consist of laminated elastic and viscoelastic layers, and formulate a boundary value problem for the warping deformations arising under Saint-Venant torsion. For some basic cross-sectional shapes, we solve the warping problem and thence obtain closed-form expressions for the complex stiffness per unit length. Finally, we provide some guidelines for the design of tubes with high damping in torsion.

4.1 Background

Consider the response of an elastic-viscoelastic beam to a harmonically varying twisting moment applied at its end. If the frequency of motion is low enough that the rotary inertia of the beam can be neglected, the internal twisting moment does not vary from section to section, and hence the strains developed in the beam are independent of the lengthwise coordinate. A slender

beam therefore takes on a constant angle of twist per unit length, and cross sections distant from either end of the beam rotate about the longitudinal axis without distortion in their own plane. But such rotation gives rise to shear stresses which, unless the cross section is axially symmetric, cause it to warp in the longitudinal direction. This model for the torsion of slender beams was first proposed by Saint-Venant in 1855 and is referred to in the literature as "uniform" or "Saint-Venant" torsion.

Near the ends of the beam, the deformation may violate the premises of the Saint-Venant theory of torsion in two important ways:

1. **Restraint Against Warping:** If an end is restrained against warping—for example, by welding it to a solid block—the deformation will not be uniform near that end. This effect is well documented in the elasticity literature and is known in homogeneous beams to be most significant for sections with large flanges (e.g., Timoshenko and Goodier, 1970; Kollbrunner and Basler, 1969). It may also cause significant nonuniformity for elastic-viscoelastic beams because, as we will see subsequently, warping displacements play an essential role in damping torsional vibration.

2. **In-Plane Distortion:** Depending on the distribution of stresses on the end of a beam, cross sections near that end may deform in their own plane. For homogeneous beams, this deformation can almost always be neglected, but for elastic-viscoelastic beams we can envision cases where it is of primary importance. Consider for example a beam made up of a circular elastic core and concentric viscoelastic and elastic layers. Suppose we exert a moment at one end of this beam on only the outer elastic layer. Near this end, the outer layer will undergo a larger rotation than the circular core, and this difference in rotation induces large strains in the viscoelastic layer. This mechanism of damping was studied by Chandrasekharan and Ghosh (1974) for straight beams and Nanda Kishore and Ghosh (1975) for coil springs. To the best of the author's knowledge, these are the only published works on nonuniform torsion of elastic-viscoelastic beams.

It is difficult to form a general measure of the importance of warping restraints and in-plane distortion; their effects must be evaluated on a case-by-case basis taking detailed account of the boundary conditions. In the present study, we will work under the assumptions of Saint-Venant torsion.

Upon review of the literature we find only two studies of Saint-Venant torsion of elastic-viscoelastic beams: Johnson and Woolf (1976) examine torsion of a two-layer beam made up of a thick elastic bar and a thin viscoelastic layer. Starting from the classical formulation given by Sokolnikoff (1956) for the stress distribution in a compound beam, they derive a perturbation solution valid when the viscoelastic layer is much more compliant than the elastic layer. From a similar formulation, Dewa (1989) generates numerical solutions for three-layer elastic-viscoelastic beams made up of solid rectangular laminae. These results do not readily generalize to beams with other cross sections and hence are of little use for structural design, where beams with solid cross sections are rarely employed.

Closed, thin-walled tubes have high flexural and torsional stiffness for a given mass, and therefore find wide application in machine structures. In the present work, we develop a model for torsion of closed, thin-walled, elastic-viscoelastic tubes. Assuming that the deformation obeys the Saint-Venant assumptions, and neglecting the rotary inertia of the compound tube, we derive expressions giving the complex torsional stiffness for two types of tube: (1) those made up of one or more elastic shells joined by viscoelastic seams to form a closed tube, and (2) those with constrained viscoelastic layers laminated to the thin elastic wall of a closed tube.

Because we neglect rotary inertia in our analysis, harmonic motion is governed in the frequency domain by equations of the same form as those governing static deformation. The reader should keep in mind, however, that the following derivations are carried out in the frequency domain and that the deformations, stresses, and strains are harmonically varying quantities whose magnitude and phase are represented by complex variables.

4.2 Thin-Walled Tube with Viscoelastic Seams

We consider in this section torsion of a member made up of one or more thin elastic shells joined into a closed tube by viscoelastic seams running the length of the tube. Such a tube, made up of a single elastic shell of modulus G_1 and a viscoelastic seam of modulus G_2 is sketched in cross section in Fig. 4.1. The shape of the tube is given by the vector $\vec{R}(s)$ whose dependence on the tangential coordinate s is normalized so that the unit vector $\vec{e}_s$ in the tangential direction is given by $d\vec{R}/ds$. For simplicity, we restrict our attention to cases

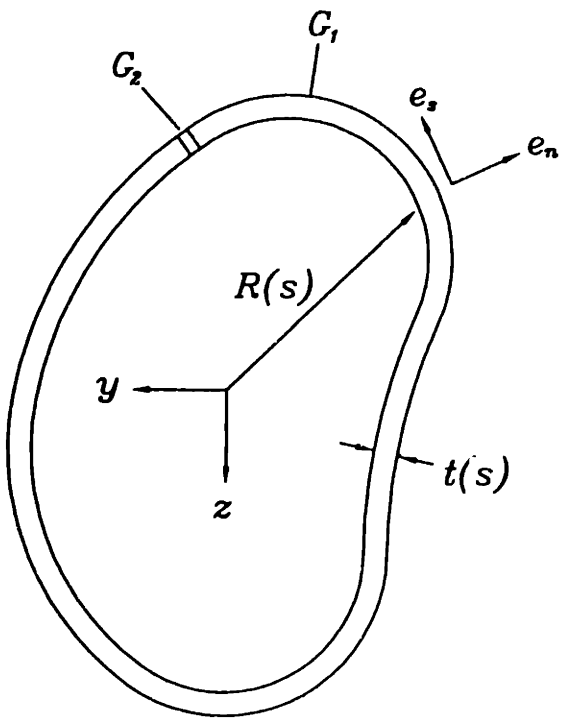

Figure 4.1 Cross section of a thin-walled tube consisting of elastic material with shear modulus G_1 and viscoelastic material with complex shear modulus G_2. The thickness of the tube wall is $t(s)$.

where $\vec{R}(s)$ divides the yz plane into a singly connected exterior and a simply connected interior; that is, the tube wall forms a single closed loop in the yz plane.

The stiffness of such a compound tube can be obtained by a straightforward generalization of the results for a homogeneous thin-walled tube (e.g., Kollbrunner and Basler, 1969). Here, we carry out the derivation in brief as a prelude to the discussion of tubes with laminated walls.

4.2.1 Modeling Assumptions

As stated previously, we assume that the tube deforms in accordance with the Saint-Venant assumptions. The analysis of thin-walled tubes is made tractable by the introduction of two further assumptions:

1. Because the tube wall is thin compared to the perimeter of the section and the inner and outer walls are traction free, the shear stress τ_{xn} in the direction normal to the perimeter is negligible.

2. The variation of the tangential shear stress τ_{xs} across the wall thickness can be neglected so that the the deformation and strain are functions of s only.

It should be noted that the second assumption is justified only for closed tubes. If the tube is open, the tangential shear stress must change sign across the thickness of the wall in order to sustain a net moment.

4.2.2 Stress Analysis

For Saint-Venant torsion, all points on the section rotate together and the warping deformation u is the same at any station along the length of the beam. Thus, if the beam takes on an angle of twist per unit length of magnitude θ we can write the deflection $\Delta\vec{R}$ of a point on the tube wall in the form

$$\Delta\vec{R} = u(s)\vec{e}_x + \theta x\vec{e}_x \times \vec{R}(s) \tag{4.1}$$

where $\vec{e}_x$ is the unit vector in the x direction. In terms of the deformation, we can write the shear strain in the tangential direction as

$$\gamma_{xs} = \frac{du}{ds} + \frac{d}{dx}\left(\Delta\vec{R}\cdot\vec{e}_s\right) \tag{4.2}$$

Now combining Eqs. (4.1) and (4.2), and making use of the vector identity $\vec{A} \times \vec{B} \cdot \vec{C} = \vec{B} \cdot \vec{C} \times \vec{A}$, we obtain

$$\gamma_{xs} = \frac{du}{ds} + \theta \vec{R} \cdot \vec{e}_n \tag{4.3}$$

A simple expression of the kinematics of twist can be obtained by integrating this expression for the shear strain around the closed section:

$$2A\theta = \oint \gamma_{xs}\, ds \tag{4.4}$$

where A is the area enclosed by the wall.

Since the inner and outer surfaces of the tube are traction free, and the shear stress in the direction normal to the tube wall is negligible, we obtain the equation of equilibrium

$$\frac{d}{ds}(t\tau_{xs}) = 0 \tag{4.5}$$

where t is the thickness of the tube wall, from which we see that the shear flow $t\tau_{xs}$ is constant over the perimeter of the section. The resultant moment M_t exerted on the cross section is computed by integrating the moment of the shear flow around the perimeter of the section. That is,

$$M_t = \oint (t\tau_{xs}) \vec{R} \cdot \vec{e}_n\, ds = 2At\tau_{xs} \tag{4.6}$$

Combining this result with the kinematic relation in Eq. (4.4), and introducing the complex shear modulus $\tau_{xs} = G(s)\gamma_{xs}$, we obtain the torsional stiffness

$$\frac{M_t}{\theta} = 4A^2 \left(\oint \frac{ds}{Gt} \right)^{-1} \tag{4.7}$$

In the present work, we are concerned with tubes whose walls are made up of piecewise uniform segments, so if the ith segment has length ℓ_i, shear modulus G_i, and thickness t_i, we can write

$$\frac{M_t}{\theta} = \frac{4A^2}{\sum_i (\ell_i / G_i t_i)} = \frac{4A^2}{\sum_i \sigma_i} \tag{4.8}$$

where the quantity $\sigma_i = \ell_i / G_i t_i$ can be interpreted as the shear compliance per unit length of the ith panel of the tube wall. From the form of Eq. (4.8), we see that segments of the tube wall work in serial to resist a twisting moment; hence introduction of a viscoelastic seam into an elastic tube wall forms a serial damper of the type discussed in Section 2.2.

4.2.3 Discussion

Now consider the particular case of a tube whose cross section has total perimeter $L_1 + L_2$ made up of (possibly non-contiguous) lengths L_1 and L_2 of elastic and viscoelastic material with shear moduli G_1 and G_2, respectively. If the wall thickness t is constant, we obtain from Eq. (4.7) the normalized complex torsional stiffness

$$k_t(1+\eta_t) = \frac{M_t}{\theta}\left(\frac{P}{4A^2G_1t}\right)\left(1+\frac{G_1L_2}{G_2L_1}\right)^{-1} \tag{4.9}$$

We note that the factor $4A^2G_1t/P$ is the torsional stiffness of a homogeneous tube of cross-sectional perimeter $P \approx L_1$ and shear modulus G_1. Hence η_t is the loss factor of the composite tube and k_t is the ratio of its static stiffness to that of the homogeneous tube. Now introducing for the viscoelastic material a storage modulus G_v and loss factor η_v and setting $G_2 = G_v(1+j\eta_v)$, we can write

$$k_t(1+j\eta_t) = \frac{M_t}{\theta}\left(\frac{P}{4A^2G_1t}\right) = \frac{1+g_t+\eta_v^2}{(1+g_t)^2+\eta_v^2} + j\frac{\eta_v g_t}{(1+g_t)^2+\eta_v^2} \tag{4.10}$$

where the coupling parameter g_t is given by

$$g_t = \frac{G_1/G_v}{L_1/L_2} \tag{4.11}$$

and we can write the composite loss factor in the form

$$\eta_t = \frac{\eta_v g_t}{1+g_t+\eta_v^2} \tag{4.12}$$

Equations (4.10) and (4.12) indicate that for small g_t the normalized stiffness approaches unity and the composite loss factor goes to zero. This is the "rigidly coupled" limit where the behavior of the tube approaches that of the homogeneous tube. For large g_t, the normalized stiffness goes to zero and the loss factor approaches that of the viscoelastic material. This behavior is illustrated in Fig. 4.2 for the case where $\eta_v = 1$.

4.3 Thin-Walled Tube with Constrained-Layer Dampers

Consider, as shown in Fig. 4.3, a closed elastic tube of modulus G_1 to which is attached a thin viscoelastic layer of modulus G_2 backed by an elastic layer of

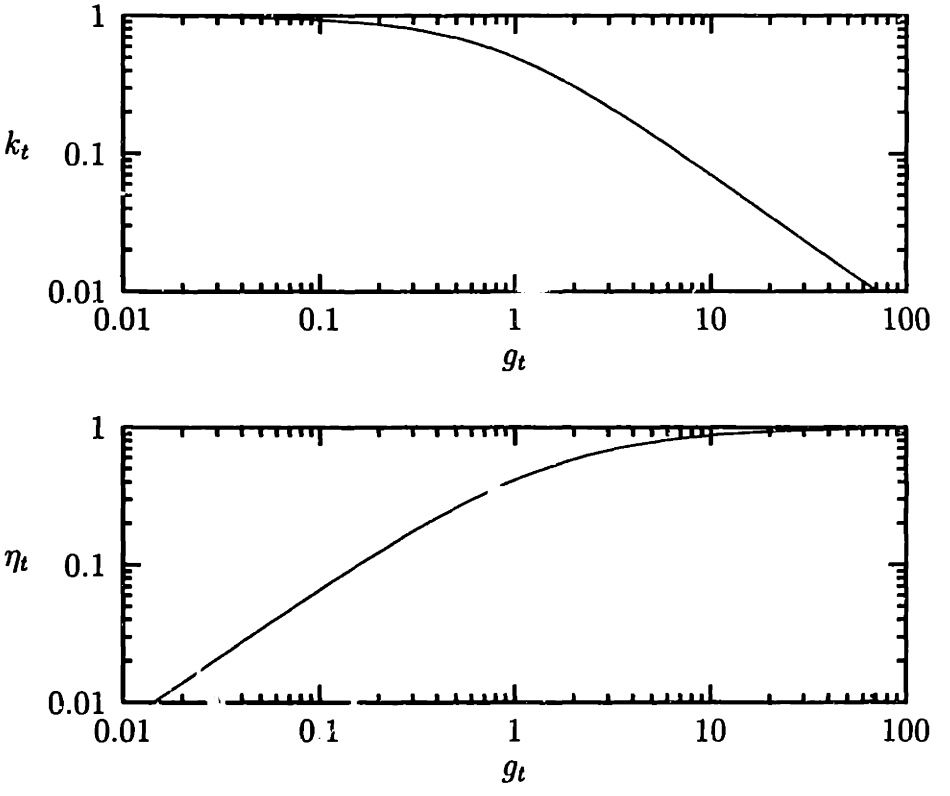

Figure 4.2 Dependence of the loss factor and normalized static stiffness on the coupling parameter $g_t = (G_1/G_v)/(L_1/L_2)$ for a thin-walled tube with viscoelastic segments with $\eta_v = 1$.

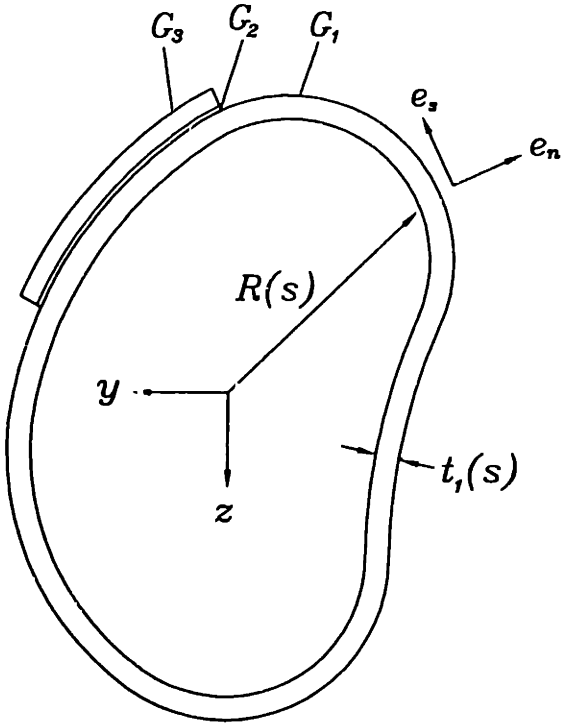

Figure 4.3 Cross section of a thin-walled tube consisting of an closed elastic tube of modulus G_1 and thickness $t_1(s)$, a viscoelastic layer of modulus G_2 and thickness $t_2(s)$, and a constraining layer of modulus G_3 and thickness $t_3(s)$.

modulus G_3. The thin-walled tube forms a single closed loop in the yz plane, and its shape is given by the vector $\vec{R}(s)$ normalized so that $d\vec{R}/ds = \vec{e}_s$. By mounting a constrained viscoelastic layer to one segment of an elastic tube wall, we form a parallel damper on that segment. But as we have seen, the individual segments of a tube wall act in series to resist a twisting moment, and hence this parallel damper acts in series with the remaining segments of the tube wall to sustain a dynamic twisting moment.

4.3.1 Modeling Assumptions

According to the Saint-Venant model, imposition of a twisting moment develops shear stresses in the yz plane. As we have seen in the previous sec-

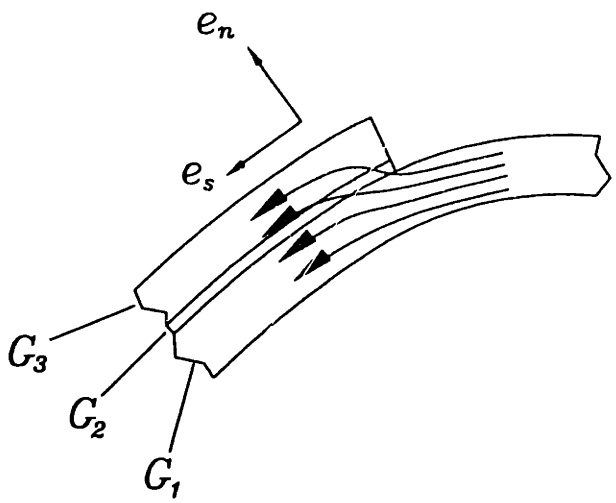

Figure 4.4 Sketch of the shear flow near the end of a constraining layer: The curved lines with arrows indicate the direction of the shear stress in the plane of the cross section.

tion, in the absence of laminated viscoelastic layers these stresses run parallel to the tube wall, and the shear flow $t\tau_{xs}$ is constant. In the present case, the shear flow $t_1(\tau_{xs})_1$ is constant only on that portion of the tube wall without lamination. On the laminated region, some stress is transmitted through the viscoelastic layer to the constraining layer, and the total shear flow $t_1(\tau_{xs})_1 + t_2(\tau_{xs})_2 + t_3(\tau_{xs})_3$ must be constant.

To get a clearer picture of the state of stress in the tube, consider the situation near the end of a constraining layer. The shear stress $(\tau_{xs})_3$ in the tangential direction in the constraining layer must vanish at the end of the layer, but may be nonzero a short distance from its end. The shear flow must then appear as sketched in Fig. 4.4, where a component of the stress is transmitted in the normal direction across the viscoelastic layer.

It follows immediately from the Saint-Venant assumptions that the only nonzero stresses are the shear stresses τ_{xs} in the tangential direction and τ_{xn} in the normal direction. So the differential equation of equilibrium in the ith layer is given by

$$\frac{\partial (\tau_{xn})_i}{\partial n} + \frac{\partial (\tau_{xs})_i}{\partial s} = 0 \tag{4.13}$$

Rather than attack this equation directly, we introduce the following modeling assumptions:

1. The viscoelastic layer is far more compliant than either of the elastic elastic layers, but is subject to the similar shear strains in the tangential direction. We can therefore neglect the shear stress $(\tau_{xs})_2$ in the tangential direction in the viscoelastic layer in comparison to $(\tau_{xs})_1$ and $(\tau_{xs})_3$ in the elastic layers.

2. The shear stress $(\tau_{xn})_2$ in the normal direction in the viscoelastic layer is of the same order as $(\tau_{xn})_1$ and $(\tau_{xn})_3$ in the elastic layers, but the viscoelastic layer is far more compliant. Hence the shear strains $(\gamma_{xn})_1$ and $(\gamma_{xn})_3$ in the elastic layers can be be neglected in comparison to $(\gamma_{xn})_2$ in the viscoelastic layer.

3. The shear stresses in the normal direction must vanish at the inner and outer walls of the tube, so it follows from Eq. (4.13) that, in the first elastic layer, $(\tau_{xn})_1 \sim (\tau_{xs})_1 t_1/R_0$ where R_0 is a characteristic length in the tangential direction and t_1 is the thickness of the inner elastic layer. Thus, for a thin-walled tube, we have $(\tau_{xn})_1 \ll (\tau_{xs})_1$. Likewise, in the constraining layer we have $(\tau_{xn})_3 \ll (\tau_{xs})_3$.

4. In the viscoelastic layer, the shear stress $(\tau_{xn})_2$ in the normal direction is of the same order as $(\tau_{xn})_1$ and $(\tau_{xn})_3$ in the elastic layers and hence (from item 3 above) is much smaller than $(\tau_{xs})_1$ or $(\tau_{xs})_3$.

5. The variation of $(\gamma_{xn})_2$ through the thickness of the viscoelastic layer and the variation of $(\tau_{xs})_1$ and $(\tau_{xs})_3$ through the thickness of the elastic layers can be neglected.

In summary: The shear *stress* in the direction tangent to the tube wall can be neglected in the viscoelastic layer but not in the elastic layers. Conversely, the shear *strain* in the direction normal to the tube wall can be neglected in the elastic layers but not in the viscoelastic layer. The shear stress in the tangential direction in the elastic layers and the shear strain in the normal direction in the viscoelastic layer can be treated as constants across the thickness of each layer. Moreover, the shear stresses are much larger in the tangential than in the normal direction.

4.3.2 Formulation

Consider a tube subject to an angle of twist per unit length of magnitude θ. Because the shear strains in the normal direction are negligible in the elastic layers, the warping displacements, u_1 in the tube wall and u_3 in the constraining layer, are functions of only the tangential coordinate s. Therefore, making use of the Saint-Venant assumptions, the displacement of a point on the tube wall can be written as

$$(\Delta\vec{R})_i = u_i(s)\vec{e}_x + \theta x\vec{e}_x \times \vec{R}(s) \tag{4.14}$$

where x is the lengthwise coordinate and $\vec{e}_x$ is the unit vector pointing along the axis of the tube.

As was argued in the foregoing, a twisting moment is resisted primarily by shear stresses in the tangential direction in the elastic layers. Making use of the deformation given in Eq. (4.14), we can write the corresponding shear strain in the tube wall as

$$(\gamma_{xs})_1 = \frac{du_1}{ds} + \frac{d}{dx}\left[(\Delta\vec{R})_1 \cdot \vec{e}_s\right] = \frac{du_1}{ds} + \theta\vec{R}\cdot\vec{e}_n \tag{4.15}$$

and, likewise, in the constraining layer

$$(\gamma_{xs})_3 = \frac{du_3}{ds} + \frac{d}{dx}\left[(\Delta\vec{R})_3 \cdot \vec{e}_s\right] = \frac{du_3}{ds} + \theta\vec{R}\cdot\vec{e}_n \tag{4.16}$$

In the viscoelastic layer, we are concerned with the shear strain in the normal direction; assuming it is constant through the thickness of the viscoelastic layer, we write it in terms of the warping displacements as

$$(\gamma_{xn})_2 = \frac{u_3 - u_1}{t_2} \tag{4.17}$$

where t_2 is the thickness of the viscoelastic layer.

In formulating the conditions for equilibrium, we examine first those portions of the tube wall not covered by a constrained viscoelastic layer. Consider a slice ds of this homogeneous wall. We have already argued that the only significant stress acting upon it is the shear stress in the direction tangent to the wall, and that this stress can be taken to be uniform through the thickness

of the wall. Denoting this stress $(\hat{\tau}_{xs})_1$, and summing forces in the x direction, we write the equation of equilibrium

$$\frac{d}{ds}\left[t_1\left(\hat{\tau}_{xs}\right)_1\right] = 0 \tag{4.18}$$

from which we see that the shear flow $t_1(\hat{\tau}_{xs})_1$ is constant on homogeneous segments of the tube wall.

On portions of the tube wall covered by a constrained viscoelastic layer, we must also consider the resultant of the normal stress transmitted through the viscoelastic layer. Hence, the force balance of the tube wall is of the form

$$\frac{d}{ds}\left[t_1\left(\tau_{xs}\right)_1\right] + \left(\tau_{xn}\right)_2 = 0 \tag{4.19}$$

Similarly, for the constraining layer we have

$$\frac{d}{ds}\left[t_3\left(\tau_{xs}\right)_3\right] - \left(\tau_{xn}\right)_2 = 0 \tag{4.20}$$

If we combine Eqs. (4.19) and (4.20), we see that the total shear flow $t_1(\tau_{xs})_1 + t_3(\tau_{xs})_3$ is constant on laminated segments of the tube wall. (Recall that $t_2(\tau_{xs})_2$ is negligible.)

Now introducing the shear moduli G_1, G_2, and G_3 for the tube wall, viscoelastic, and elastic layers respectively, we can use the shear strains given in Eqs. (4.15)–(4.17) to write the equations of equilibrium (4.18)–(4.20) in terms of the warping displacements. On homogeneous segments of the wall, we obtain

$$\frac{d}{ds}\left[G_1 t_1\left(\frac{d\hat{u}_1}{ds} + \theta\vec{R}\cdot\vec{e}_n\right)\right] = 0 \tag{4.21}$$

where we have introduced the notation $\hat{u}_1$ for the warping displacement on a homogeneous segment of the wall. On laminated segments of the wall, we obtain

$$\frac{d}{ds}\left[G_1 t_1\left(\frac{du_1}{ds} + \theta\vec{R}\cdot\vec{e}_n\right)\right] + \frac{G_2}{t_2}\left(u_3 - u_1\right) = 0 \tag{4.22}$$

for the tube wall and

$$\frac{d}{ds}\left[G_3 t_3\left(\frac{du_3}{ds} + \theta\vec{R}\cdot\vec{e}_n\right)\right] - \frac{G_2}{t_2}\left(u_3 - u_1\right) = 0 \tag{4.23}$$

for the constraining layer.

The warping displacements are governed by Equation (4.21) on homogeneous regions of the tube wall and by Eqs. (4.22) and (4.23) on laminated regions of the tube wall. Our task is to solve these equations subject to the following conditions:

1. The shear stress $(\tau_{xs})_3$ must vanish at the ends of a constraining layer. In terms of the warping displacement, this condition takes the form

$$\frac{du_3}{ds} + \theta \vec{R} \cdot \vec{e}_n = 0 \tag{4.24}$$

2. At junctions between laminated and homogeneous segments of the wall, the stresses in the tangential direction as well as the warping displacements must match; that is, $u_1 = \hat{u}_1$ and $(\tau_{xs})_1 = (\hat{\tau}_{xs})_1$ at the ends of a constraining layer.

3. The resultant of the shear stress on a cross section must equal the applied moment. The total moment is obtained by integrating the shear flow over the periphery of the section, and since the total shear flow is constant, we can evaluate it on a homogeneous segment of the wall where it is given by $t_1(\hat{\tau}_{xs})_1$. Integrating around the perimeter of the section, we obtain

$$M_t = \oint (t_1 (\hat{\tau}_{xs})_1) \vec{R} \cdot \vec{e}_n \, ds = 2A \left[t_1 (\hat{\tau}_{xs})_1 \right] \tag{4.25}$$

which combines with Eq. (4.15) to yield

$$M_t = 2A \left[G_1 t_1 \left(\frac{d\hat{u}_1}{ds} + \theta \vec{R} \cdot \vec{e}_n \right) \right] \tag{4.26}$$

where A is the area enclosed by the tube wall. The quantity in brackets can be evaluated anywhere on the homogeneous segments of the wall.

In the following sections, we use this formulation to derive expressions for the complex stiffness for some specific cross sections. We begin by considering a round tube with a single laminated viscoelastic segment, and then generalize the results to round tubes with multiple symmetric laminated regions. Finally, we obtain solutions for rectangular tubes with all four faces laminated.

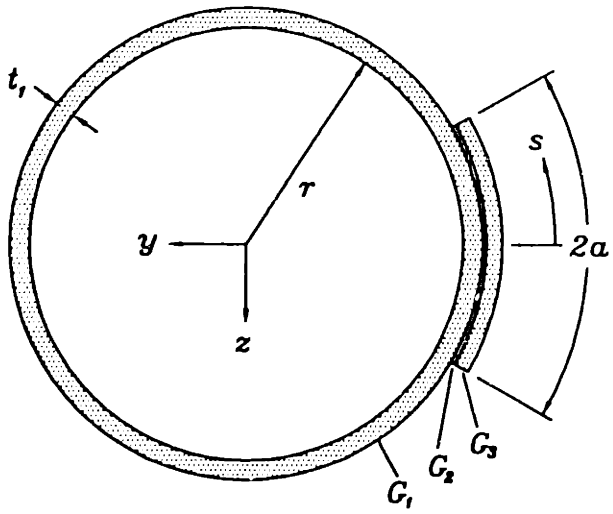

Figure 4.5 Cross section of a circular tube with a single constrained viscoelastic layer: The tube wall has shear modulus G_1, thickness t_1, and perimeter $2b$. The constrained viscoelastic layer extends over a length $2a$ of the tube wall and consists of a viscoelastic layer with complex modulus G_2 and thickness t_2 backed by an elastic layer with modulus G_3 and thickness t_3.

4.3.3 Circular Tube with a Constrained Viscoelastic Layer

Consider the tube shown in Fig. 4.5, which consists of a circular tube of radius r and constant wall thickness t_1 to which is laminated a viscoelastic layer of thickness t_2 backed by a constraining layer of thickness t_3. We set the origin of the tangential coordinate system at the center of the constraining layer so that the ends of the constraining layer are at $s = \pm a$. We also find it convenient to develop solutions in terms of the parameter b, which at present we set equal to πr so that $s = \pm b$ is the location on the tube wall directly opposite the midpoint of the constrained viscoelastic layer.

Before proceeding to solve for the warping displacements, it is useful to see how this tube fits into the framework discussed in Chapter 2. If the viscoelastic layer is infinitely compliant, the constraining layers contribute nothing to the torsional stiffness of the tube, and the torsional stiffness, from Eq. (4.8), is

simply

$$k_0 = \frac{4A^2 G_1 t_1}{2b} \tag{4.27}$$

where A is the area enclosed by the tube wall. At the other extreme, if the viscoelastic layer is rigid, Eq. (4.8) yields

$$k_\infty = \frac{4A^2 G_1 t_1 (G_1 t_1 + G_3 t_3)}{2b(G_1 t_1 + G_3 t_3) - 2aG_3 t_3} \tag{4.28}$$

From these results, we can form the stiffness ratio

$$K = \frac{k_\infty - k_0}{k_0} = \frac{aG_3 t_3}{b(G_1 t_1 + G_3 t_3) - aG_3 t_3} \tag{4.29}$$

which we expect to play an important role in determining the damping in the tube. We may also form a coupling parameter which measures the stiffness of the viscoelastic layer, but the form of such a parameter is difficult to descry without knowledge of the deformation.

Warping Displacements

For a circular tube with constant wall thickness, Eqs. (4.22) and (4.23) governing the warping displacements u_1 and u_3 on laminated regions of the tube reduce to

$$G_1 t_1 \frac{d^2 u_1}{ds^2} + \frac{G_2}{t_2}(u_3 - u_1) = 0 \tag{4.30}$$

$$G_3 t_3 \frac{d^2 u_3}{ds^2} - \frac{G_2}{t_2}(u_3 - u_1) = 0 \tag{4.31}$$

The general solution of this system of homogeneous equations can be written in the form

$$\begin{bmatrix} u_1 \\ u_3 \end{bmatrix} = (c_1 + c_2 s)\begin{bmatrix} 1 \\ 1 \end{bmatrix} + \left(c_3 \sinh \frac{g_t s}{a} + c_4 \cosh \frac{g_t s}{a}\right)\begin{bmatrix} 1 \\ \kappa \end{bmatrix} \tag{4.32}$$

where $\kappa = -G_1 t_1 / G_3 t_3$, the c_i are constants to be determined from the matching conditions, and the eigenvalue g_t/a is given by

$$\frac{g_t}{a} = \sqrt{\frac{G_2}{t_2}\left(\frac{G_1 t_1 + G_3 t_3}{G_1 t_1 G_3 t_3}\right)\left(\frac{a}{b}\right)} = \sqrt{\frac{G_2}{t_2}\left(\frac{1}{G_1 t_1 Y}\right)\left(\frac{a}{b}\right)} \tag{4.33}$$

where

$$Y = \frac{G_3 t_3}{G_1 t_1 + G_3 t_3} \left(\frac{a}{b}\right) \tag{4.34}$$

Examining the form of g_t/a given above, we see that it is a measure of the stiffness of the viscoelastic layer relative to that of the elastic layers. The parameter Y is related to the stiffness ratio K defined in Eq. (4.29) by

$$Y = \frac{K}{1-K} = 1 - \frac{k_0}{k_\infty} \tag{4.35}$$

As we shall see, the dimensionless parameters g_t and Y fully determine the complex stiffness of the composite tube.

On regions of the tube without lamination, the warping displacement $\hat{u}_1$ is governed by Eq. (4.21), which for a circular tube with constant wall thickness reduces to

$$G_1 t_1 \frac{d^2 \hat{u}_1}{ds^2} = 0 \tag{4.36}$$

whose general solution we write in the form

$$\hat{u}_1 = c_5 s + c_6 \tag{4.37}$$

where c_5 and c_6 are constants. Whereas an axially symmetric tube does not warp, we see from the warping displacements given by Eqs. (4.37) and (4.32) that the addition of the constrained viscoelastic layer causes the tube wall to warp to take on a constant slope on regions without lamination and to take on some curvature on regions with lamination.

The relative magnitudes of the warping displacements are determined upon enforcement of the matching conditions. We can argue that the warping displacements go to zero on the axis of symmetry; thus, at $s = 0$ we have

$$u_1(0) = u_3(0) = 0 \tag{4.38}$$

and at $s = b = \pi r$ we have

$$\hat{u}_1(b) = 0 \tag{4.39}$$

At $s = a$, the shear stress in the constraining layer must vanish. This condition, set forth Eq. (4.24), reduces to

$$\frac{du_3(a)}{ds} + r\theta = 0 \tag{4.40}$$

for a circular tube. In the tube wall, the displacements must match:

$$u_1(a) = \hat{u}_1(a) \tag{4.41}$$

The shear stresses must also match. Using Eq. (4.15), we write

$$\frac{du_1(a)}{ds} = \frac{d\hat{u}_1(a)}{ds} \tag{4.42}$$

The six matching conditions given in Eqs. (4.38)–(4.42) determine the constants c_1 through c_6 in terms of the angle of twist per unit length θ.

Substituting the warping displacements (4.37) and (4.32) into the matching conditions (4.38)–(4.42), and solving for the the c_i, we write the warping displacements in the form

$$\hat{u}_1 = \frac{br\theta Y\lambda}{1-\lambda Y}\left(\frac{s}{b} - 1\right) \tag{4.43}$$

and

$$\begin{bmatrix} u_1 \\ u_3 \end{bmatrix} = \frac{br\theta Y}{1-Y\lambda}\left\{\frac{\sinh g_t s/a}{g_t \cosh g_t}\begin{bmatrix} 1 \\ \kappa \end{bmatrix} + \left(\lambda - \frac{b}{a}\right)\left(\frac{s}{b}\right)\begin{bmatrix} 1 \\ 1 \end{bmatrix}\right\} \tag{4.44}$$

where g_t is defined in Eq. (4.33), Y is defined in Eq. (4.29), and

$$\lambda = 1 - \frac{\tanh g_t}{g_t} \tag{4.45}$$

We can now plot the warping displacements as shown in Fig. 4.6, where we illustrate the effect of increasing g_t for fixed Y and a/b. For small g_t, the tube wall and the constraining layer are nearly decoupled: the tube wall warps only slightly and the constraining layer suffers little shear deformation as it undergoes a large rigid-body rotation. As g_t is increased, the coupling becomes stronger, and we see that for large g_t the tube wall is strongly warped. We expect that the damping will be highest at intermediate values of g_t where the coupling is strong enough to induce significant stress into the constraining layer, but weak enough to allow significant strain.

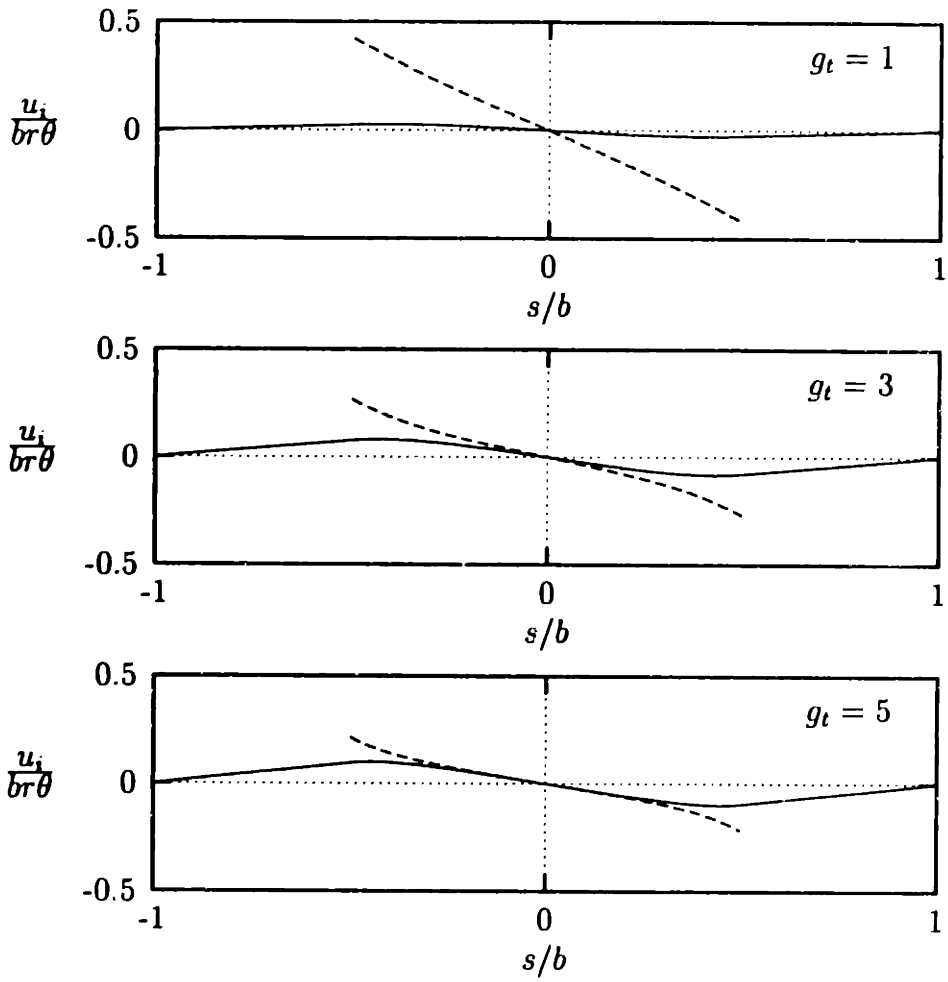

Figure 4.6 Static normalized warping displacements $u_1/br\theta$ and $u_3/br\theta$ in a circular tube with a single constrained viscoelastic layer; $a/b = 0.5$, $Y = 0.2$, $\kappa = 1.5$, and various g_t

Complex Stiffness

Substituting the expression for $\hat{u}_1$ given by Eq. (4.43) into the integral condition for the total moment on the tube set forth in Eq. (4.26), we obtain

$$k_t(1 + j\eta_t) = \frac{M_t}{\theta}\left(\frac{P}{4A^2G_1t_1}\right) = \frac{1}{1 - \lambda Y} \tag{4.46}$$

where k_t is the normalized static stiffness of the tube and η_t is its loss factor. The parameter Y, as we have seen, depends only on the material properties and dimensions of the tube wall and constraining layer, whereas λ is a function of g_t, which is a measure of the stiffness of the viscoelastic layer. Modeling the viscoelastic material as frequency-independent hysteretic, we write its complex shear modulus as $G_2 = G_v(1 + j\eta_v)$ and rewrite Eq. (4.33) as

$$g_t = \sqrt{(1 + j\eta_v)\frac{a^2G_v}{t_2}\left(\frac{1}{G_1t_1Y}\right)\left(\frac{a}{b}\right)} \tag{4.47}$$

The dependence of λ on g_t is given in Eq. (4.45), from which we see that λ approaches zero for small $|g_t|$ and unity for large $|g_t|$. At intermediate magnitudes of complex g_t, λ takes on complex values, yielding non-zero η_t.

In Fig. 4.7, we have fixed $\eta_v = 1$ and plotted the stiffness and loss factor as a function of the real part of g_t. As expected, the damping is maximized at intermediate magnitudes of g_t. The data shown are for $Y = 0.2$ which implies a stiffness factor K of 0.25. Since Y and λ appear as products in Eq. (4.46) for the torsional stiffness, the damping potential can be improved by increasing Y.

4.3.4 Circular Tube with Multiple Constrained Viscoelastic Layers

In this section, we consider torsion of a thin-walled tube with multiple constrained viscoelastic layers arrayed symmetrically on the tube wall. As shown in Fig. 4.8, each of the N identical constrained viscoelastic layers extends over a length $2a$ of the tube wall of total perimeter $2Nb$.

The equations of equilibrium take on exactly the same form as they did for a tube with a single constraining layer of length $2a$ on a tube of perimeter $2b$, so Eqs. (4.30), (4.31), and (4.36) governing the warping displacements are still valid for this case. The boundary conditions matching displacements and stresses at the ends of the constraining layers are unchanged, and we can again

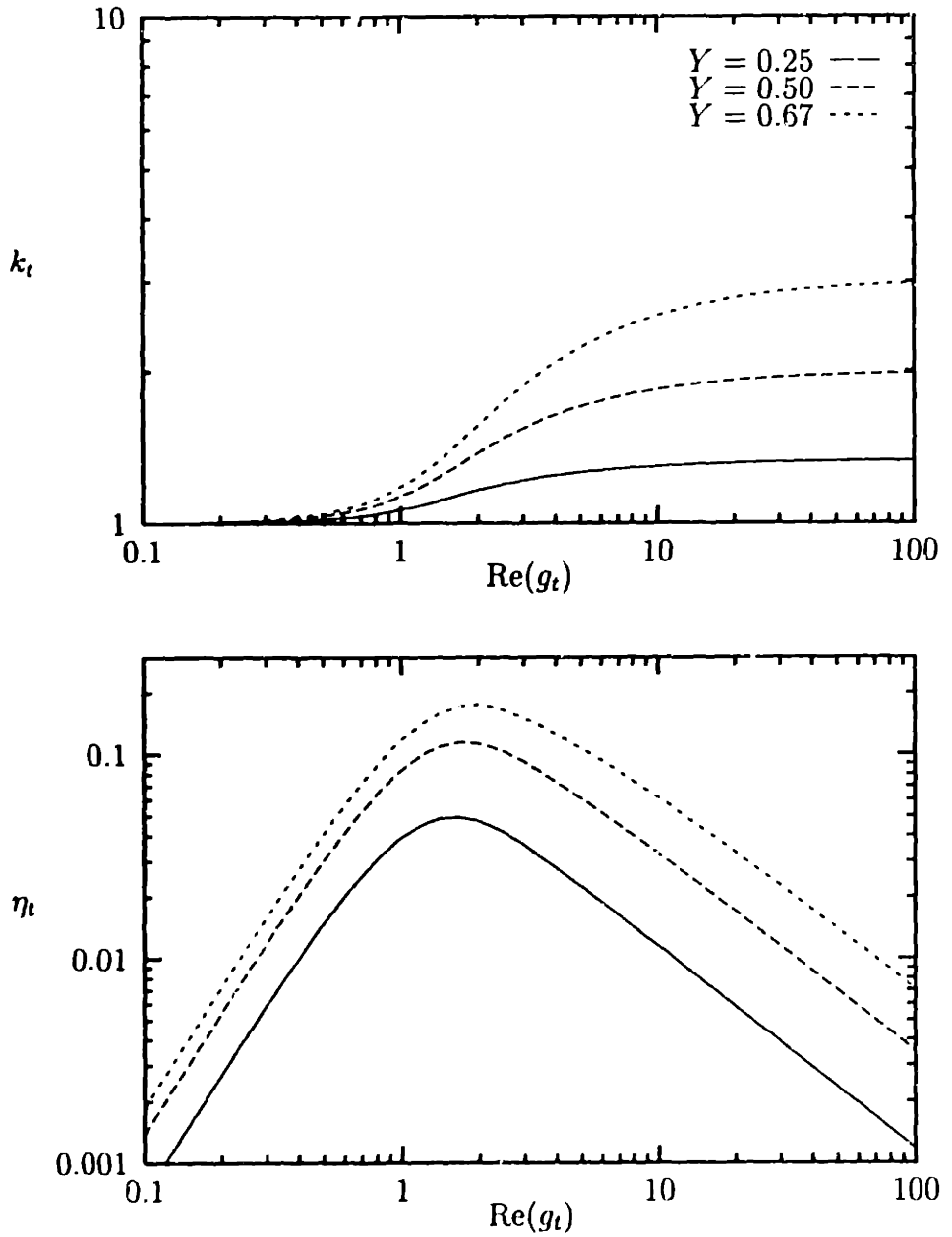

Figure 4.7 Static stiffness and loss factor plotted against the real part of g_t for a circular tube with a single constrained viscoelastic layer with $\eta_v = 1$ and $Y = 0.25$, 0.50, and 0.67.

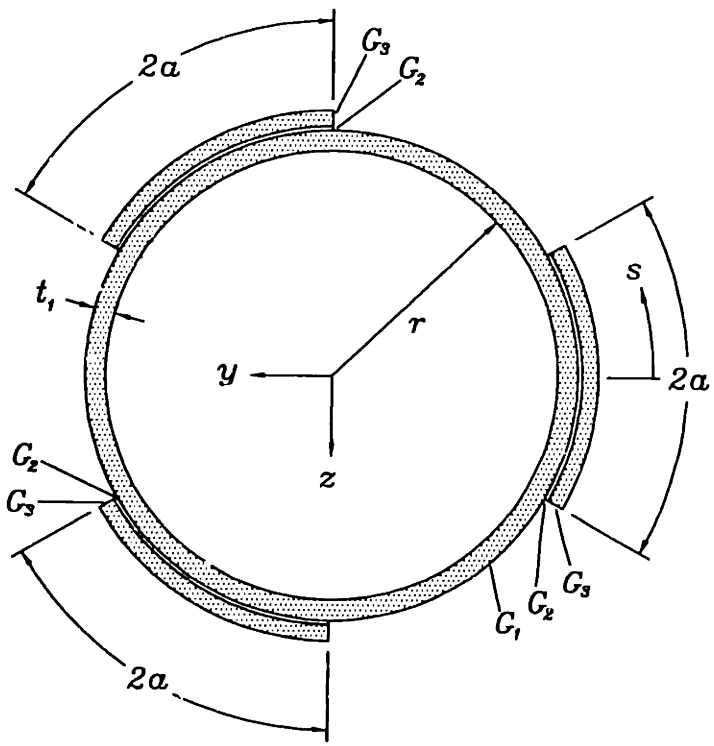

Figure 4.8 Cross section of a circular tube with three constrained viscoelastic layers arranged symmetrically on its perimeter: The tube wall has modulus G_1, thickness t_1, and perimeter $6b$. Each of the constrained viscoelastic layers extends over a length $2a$ of the tube wall, and consists of a viscoelastic layer of complex modulus G_2 and thickness t_2 and elastic layer of modulus G_3 and thickness t_3.

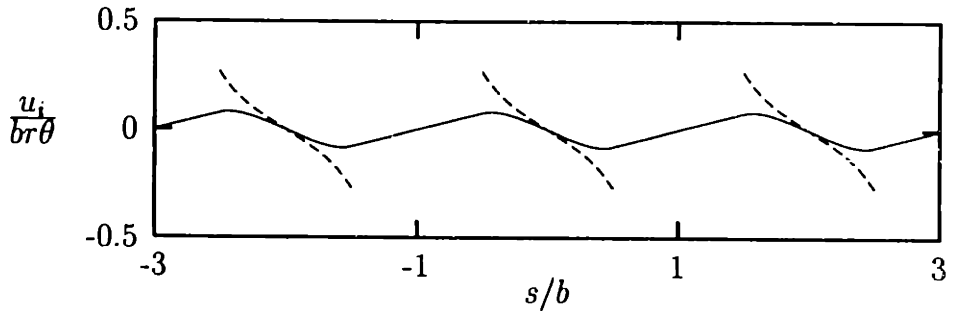

Figure 4.9 Static normalized warping displacements $u_1/br\theta$ and $u_3/br\theta$ in a circular tube with three constrained viscoelastic layers arranged symmetrically on the tube wall; $a/b = 0.5$, $Y = 0.2$, $\kappa = 1.5$, and $g_t = 3$.

argue from symmetry that the warping displacements must vanish at $s = 0$ and integer multiples of b. So we can also reuse the boundary conditions given in Eqs. (4.38)–(4.42). Thus the solutions for the warping displacements on $-b \leq s \leq b$ are independent of the number of constrained viscoelastic layers arrayed around the section, and the warping displacements on $-Nb \leq s \leq Nb$ can be constructed simply by stringing the displacements on $-b \leq s \leq b$ together as shown in Fig. 4.9.

The torsional stiffness of a composite tube with multiple constrained viscoelastic layers can be derived by the same method used for a tube with a single constrained viscoelastic layer, and we find that the result given in Eq. (4.46) is unchanged. Thus, for identical values of Y and λ, the same complex torsional stiffness is obtained for any number of symmetrically arrayed constrained viscoelastic layers.

This leads to some simple laws for scaling design parameters. Suppose for example that we have found a design using a single constrained viscoelastic layer which yields a favorable complex stiffness but requires the use of an unreasonably thick viscoelastic layer. If we split the constraining layer into four segments and hold a/b, t_1, t_3, and the material properties constant, Y does not change. Then from Eq. (4.33), we see that to obtain the same value of g_t (and therefore the same value of λ) we must scale the thickness t_2 of the viscoelastic layer with a^2. Thus, in our example, by cutting the constraining layer into four segments, we can reduce the thickness of the viscoelastic layer by a factor of sixteen without changing the complex stiffness.

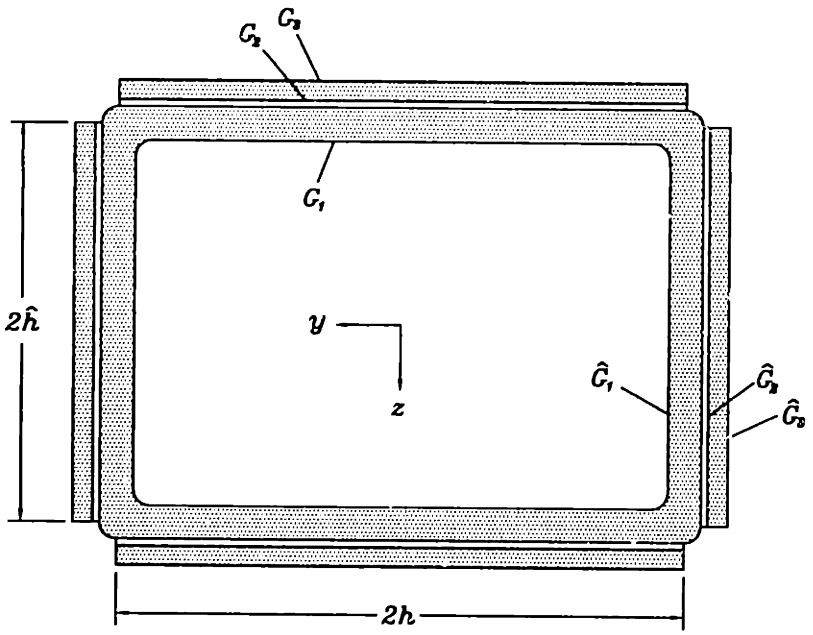

Figure 4.10 Cross-section of a rectangular tube: The tube is symmetric about both the y and z axes.

4.3.5 Rectangular Tubes

Consider the rectangular tube with constrained viscoelastic layers shown in Fig. 4.10. The faces of the tube that extend in the y direction have thickness t_1, shear modulus G_1, and length $2h$. These faces are covered completely by visceolastic layers of thickness t_2 and shear modulus G_2, which in turn are covered by elastic layers of thickness t_3 and modulus G_3. The faces of the tube that extend in the z direction have a similar layup, but possibly different dimensions and material properties. These are denoted in the like manner, but with the addition of a hat (e.g., $\hat{t}_1$, $\hat{G}_1$).

Warping Displacements

Examining Eqs. (4.22) and (4.23), we note that the quantity $\vec{R} \cdot \vec{e}_n$ is simply the normal distance from the origin to the face of the tube, and hence its derivative vanishes along any face of the tube. In the corners of the tube, the normal distance changes rapidly with s, but even large strains on such a

localized region cannot lead to large warping deflections, and we can safely ignore the corner effects when solving for the overall warping deflections in the tube.

On the segement of the tube from $y = -h$ to h, Eqs. (4.22) and (4.23) governing the warping displacements $u_1(y)$ and $u_3(y)$ become

$$G_1 t_1 \frac{d^2 u_1}{dy^2} + \frac{G_2}{t_2}(u_3 - u_1) = 0 \tag{4.48}$$

and

$$G_3 t_3 \frac{d^2 u_3}{dy^2} - \frac{G_2}{t_2}(u_3 - u_1) = 0 \tag{4.49}$$

whose general solution we denote

$$\begin{bmatrix} u_1 \\ u_3 \end{bmatrix} = (c_1 + c_2 y)\begin{bmatrix} 1 \\ 1 \end{bmatrix} + \left(c_3 \sinh \frac{g_t y}{h} + c_4 \cosh \frac{g_t y}{h}\right)\begin{bmatrix} 1 \\ \kappa \end{bmatrix} \tag{4.50}$$

where $\kappa = -G_1 t_1 / G_3 t_3$ and, in agreement with the results for a round tube with $a = b$ given in Eqs. (4.33) and (4.34),

$$g_t = \sqrt{\frac{G_2}{t_2}\left(\frac{h^2}{G_1 t_1 Y}\right)} \tag{4.51}$$

and

$$Y = \frac{G_3 t_3}{G_1 t_1 + G_3 t_3} \tag{4.52}$$

On the segment from $z = -\hat{h}$ to $\hat{h}$, the warping displacements $\hat{u}_1(z)$ and $\hat{u}_3(z)$ are governed by

$$\hat{G}_1 \hat{t}_1 \frac{d^2 \hat{u}_1}{dz^2} + \frac{\hat{G}_2}{\hat{t}_2}(\hat{u}_3 - \hat{u}_1) = 0 \tag{4.53}$$

$$\hat{G}_3 \hat{t}_3 \frac{d^2 \hat{u}_3}{dz^2} - \frac{\hat{G}_2}{\hat{t}_2}(\hat{u}_3 - \hat{u}_1) = 0 \tag{4.54}$$

whose solution we write

$$\begin{bmatrix} \hat{u}_1 \\ \hat{u}_3 \end{bmatrix} = (c_5 + c_6 z)\begin{bmatrix} 1 \\ 1 \end{bmatrix} + \left(c_7 \sinh \frac{\hat{g}_t z}{\hat{h}} + c_8 \cosh \frac{\hat{g}_t z}{\hat{h}}\right)\begin{bmatrix} 1 \\ \hat{\kappa} \end{bmatrix} \tag{4.55}$$

where $\hat{\kappa} = -\hat{G}_1\hat{t}_1/\hat{G}_3\hat{t}_3$, and $\hat{g}_t$ and $\hat{Y}$ are defined as in Eqs. (4.51) and (4.52) but with the addition of hats on all quantities. The constants c_1 through c_8 are determined by the imposition of eight matching conditions.

The cross section of the tube has two axes of symmetry, so the warping displacements must vanish at the midpoints of the walls:

$$u_1(0) = u_3(0) = 0 \tag{4.56}$$

$$\hat{u}_1(0) = \hat{u}_3(0) = 0 \tag{4.57}$$

Because of the symmetry, we can restrict our attention to the upper left quadrant of the cross section in Fig. 4.10, and we need to establish matching conditions at only one corner. The displacement and shear flow in the tube walls must match at a corner. Hence, at $y = h$ and $z = \hat{h}$, we write

$$u_1(h) = \hat{u}_1(\hat{h}) \tag{4.58}$$

and

$$G_1 t_1 \left(\frac{du_1(h)}{dy} + \theta\hat{h} \right) = \hat{G}_1\hat{t}_1 \left(-\frac{d\hat{u}_1(\hat{h})}{dz} + \theta h \right) \tag{4.59}$$

where we have made use of the expression for shear strain given in Eq. (4.15). At the ends of the constraining layers, the shear stresses must go to zero; in terms of the displacements, this condition takes the form

$$\frac{du_3(h)}{dy} + \theta\hat{h} = 0 \tag{4.60}$$

$$-\frac{d\hat{u}_3(\hat{h})}{dz} + \theta h = 0 \tag{4.61}$$

Now using the eight matching conditions (4.56)–(4.61) to solve for the c_i, we can write the warping displacements $u_1(y)$ and $u_3(y)$ in the form

$$\begin{bmatrix} u_1 \\ u_3 \end{bmatrix} = \frac{2h\hat{h}\theta\sigma Y}{\Lambda} \left\{ \frac{\sinh g_t y/h}{g_t \cosh g_t} \begin{bmatrix} 1 \\ \kappa \end{bmatrix} - \left(\kappa + \frac{\Lambda}{2\sigma Y} \right) \begin{bmatrix} 1 \\ 1 \end{bmatrix} \left(\frac{y}{h} \right) \right\} \tag{4.62}$$

where

$$\Lambda = \sigma(1 - \lambda Y) + \hat{\sigma}(1 - \hat{\lambda}\hat{Y}) \tag{4.63}$$

and, as in the case of circular tubes,

$$\lambda = 1 - \frac{\tanh g_t}{g_t} \quad \text{and} \quad \hat{\lambda} = 1 - \frac{\tanh \hat{g}_t}{\hat{g}_t} \tag{4.64}$$

The quantities σ and $\hat{\sigma}$ represent the shear compliances per unit length of the tube wall

$$\sigma = \frac{4h}{G_1 t_1} \quad \text{and} \quad \hat{\sigma} = \frac{4\hat{h}}{\hat{G}_1 \hat{t}_1} \tag{4.65}$$

which are defined so that the torsional stiffness of the tube without constraining layers is $A^2/(\sigma + \hat{\sigma})$. The warping displacements $\hat{u}_1(z)$ and $\hat{u}_3(z)$ take the same form as given in Eq. (4.62), but with y replaced by $-z$ and the hatted and unhatted quantities interchanged.

Torsional Stiffness

The resultant moment is given by integrating the shear flow around the periphery. The total shear flow is constant and most easily evaluated near a corner, where the stress in the constraining layer is zero and the shear flow is concentrated in the tube wall. Therefore, we rewrite Eq. (4.26) for this case as

$$M_t = 2AG_1 \left[\frac{du_1(h)}{dy} + \theta \hat{h} \right] \tag{4.66}$$

which, upon substitution for u_1 from Eq. (4.62) above yields

$$k_t (1 + j\eta_t) = \frac{M_t}{\theta} \left(\frac{\sigma + \hat{\sigma}}{A^2} \right) = \frac{\sigma + \hat{\sigma}}{\sigma(1 - \lambda Y) + \hat{\sigma}(1 - \hat{\lambda}\hat{Y})} \tag{4.67}$$

where η_t is the loss factor of the compound tube and k_t is the ratio of its static stiffness to that of the tube in the absence of constrained viscoelastic layers.

Comparing the form of the complex stiffness given in Eq. (4.67) above to that in Eq. (4.46) for a circular tube, we see that damping treatments on round and rectangular tubes have essentially the same character, the only difference being a lower degree of symmetry in rectangular tubes. Suppose the tube is a square with constant wall thickness, so that $\sigma = \hat{\sigma}$. If we restrict our attention to damping treatments where the constrained viscoelastic layers mounted to

each of the four faces of the tube are identical, we also have $Y = \hat{Y}$ and $\lambda = \hat{\lambda}$ and the normalized torsional stiffness given in Eq. (4.67) becomes

$$k_t(1 + j\eta_t) = \frac{1}{1 + Y\lambda} \tag{4.68}$$

in full agreement with Eq. (4.46) for a fully covered circular tube. If instead we wish to mount dampers to only two faces of the tube, then we can set $\hat{\lambda}$ to zero and obtain

$$k_t(1 + j\eta_t) = \frac{1}{1 + Y\lambda/2} \tag{4.69}$$

which is in agreement with Eq. (4.46) for a circular tube with viscoelastic layers on half of its circumference.

4.4 Design Notes

We have considered two methods of damping torsional motion in thin-walled tubes. In the first approach, a viscoelastic seam is introduced into an elastic tube wall to form a series damper. Such a configuration can yield a great deal of damping but somewhat lower stiffness than a closed elastic tube (see Fig. 4.2). The complex stiffness of such a tube, when normalized against that of a closed elastic tube of the same geometry, depends only upon a coupling parameter which takes the generic form

$$g = \frac{G_1/G_2}{L_1/L_2} \tag{4.70}$$

where G_1 and L_1 are, respectively, the shear modulus and total length of the elastic segments of the tube wall; and G_2 and L_2 are, respectively, the complex shear modulus and total length of the viscoelastic segments of the tube wall. The propensity of such a tube to creep makes it unsuitable for many applications: Under a static torsional load M_s it will eventually take up the same angle of twist per unit length as would an open tube, which is given by

$$\theta = \frac{M_s}{\frac{1}{3}t^3 L_1 G_1} \tag{4.71}$$

and is usually a few orders of magnitude larger than would be obtained for a closed tube.

In the second approach, we laminate constrained viscoelastic layers to the surface of a closed elastic tube to form a series of parallel dampers. We have seen that the complex stiffness of such a tube in torsion depends on two quantities for each constrained viscoelastic layer: one parameter of the generic form

$$Y = \frac{k_\infty - k_0}{k_\infty} \tag{4.72}$$

which is a measure of the increase in stiffness that could be obtained by rigidly bonding the constraining layer to the tube wall, and a second parameter $g \propto (G_2/t_2)^{1/2}$ which is a measure how strongly the viscoelastic layer couples the constraining layer to the tube wall. As in the case of most parallel dampers, the highest damping is obtained by maximizing Y and holding g at an intermediate magnitude.

So how does one achieve maximum damping with constrained viscoelastic layers? First, maximize Y by placing constraining layers where the tube wall is most compliant as measured by $\sigma = \ell/Gt$, where ℓ is the length of the segment of the tube wall, G is its shear modulus, and t is its thickness. If the tube wall is uniform, then complete coverage maximizes Y. For a given Y, the best value for g for a circular or square tube can be determined from Fig. 4.7. (For other geometries, use the theory given in Section 4.3.2.) An element of freedom in specifying the viscoelastic layer can be introduced by segmenting the constraining layer.

4.5 Conclusions and Future Work

In this chapter, we have developed models for the torsional vibration of closed, thin-walled, elastic-viscoelastic tubes, and provided a framework for determination of the complex stiffness per unit length of such tubes. Elastic and viscoelastic materials may be combined in many ways to form a thin-walled tube; the two most basic are by alternating either along the perimeter of the wall or through its thickness. We have found that the stress distribution in either case can be modeled with some fidelity in closed form.

In our analysis, we have ignored the inertia effects and concentrated on the determination of the complex stiffness under uniform torsion. If one is faced with a problem with distributed loading or significant rotary inertia, the complex stiffness derived here can be used in formulation of a distributed-

parameter model, provided that the characteristic length in the longitudinal direction is much larger than the cross section.

We have restricted our attention to cross sections where the wall forms a single closed loop in the xy plane. But the modeling assumptions—and indeed, the equations governing the warping deflections—can be applied without modification to multi-cell tubes, though satisfying the matching conditions becomes somewhat more tedious algebraically.

In keeping with the classical Saint-Venant model of torsion, we have ignored all end effects, but because the structures we are concerned with in machine design are not always slender, it would be useful to develop some estimates of their importance. As we have seen, the warping deflections play a key role in damping the torsional vibration of elastic-viscoelastic beams, so restraining the ends of such beams from warping can have a major impact on their damping properties. It is also possible for an uneven stress distribution at the point of loading of an elastic-viscoelastic beam to cause its cross section to deform within its own plane. To date, this effect has been studied only in beams with axially symmetric sections (Chandrasekharan and Ghosh, 1974).

CHAPTER 5

Damping Axial Motion in Leadscrew Drives

5.1 Leadscrew End Damper

A linear-motion system incorporating a leadscrew drive is shown schematically in Fig. 5.1. The leadscrew (1) is mounted to the machine base by means of rotary bearings (2) and (3) and driven by a motor (4) via a flexible coupling (5). The nut (6) is mounted to the carriage (7) which is constrained to move axially on linear bearings (not shown).

In modern machine applications, such a system is usually operated under closed-loop control where the position of the carriage, the rotation of the motor, or both are measured and used as feedback. If the feedback signal involves only rotation of the motor, axial disturbances are rejected in proportion to the mechanical impedance of the leadscrew mechanism. If the feedback signal includes the position of the carriage, the achievable bandwidth of the mechanism is limited by its impedance. In either case, high mechanical impedance is a prerequisite for rapid, accurate motion of the system.

5.1.1 Prior Art

In designing a mechanism for high mechanical impedance, one usually seeks to raise its rigidity and damping while minimizing its inertia. For most configurations, the nut, support bearings, and coupling can be sized for high rigidity without significantly increasing inertia. But the leadscrew has longitudinal stiffness proportional to the square of its radius and rotary inertia propor-

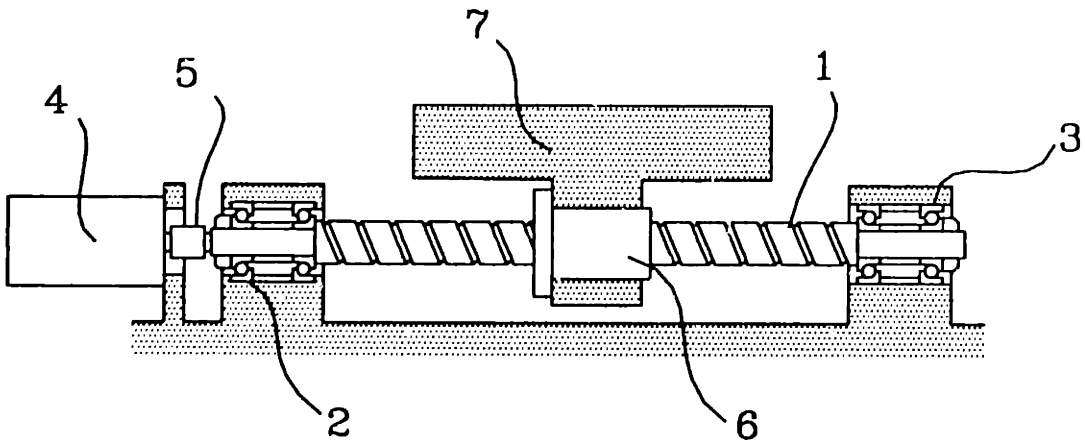

Figure 5.1 Schematic of a typical leadscrew drive system.

tional to the fourth power of its radius. Thus the tradeoff between stiffness and inertia drives the design toward relatively compliant screws.

During operation of the mechanism, friction between the screw and nut generates significant heat, leading to a temperature rise and thermal expansion in the screw. To accommodate this expansion, the screw is usually allowed to slide freely in the axial direction at the support bearing (3) furthest from the motor. Thus, the entire thrust load is transmitted to the base through the serial combination of the thrust bearing (2) and that portion of the screw between the nut (6) and thrust bearing (2).

The rigidity of the loaded portion of the screw is inversely proportional to its length, so that the overall rigidity of the mechanism decreases as the carriage moves away from the thrust bearing (2). For the representative system described in Table 5.1, we plot in Fig. 5.2 the response of carriage position to motor torque as a function of frequency for various carriage positions. As the carriage moves away from the thrust bearing, the resonant frequency drops and its peak amplitude rises.

The maximum bandwidth achievable with feedback proportional to carriage position can be determined graphically from Fig. 5.2 by drawing a line horizontally through the resonant peak, finding its intersection with the portion of the curve to its left, and reading off the frequency. A somewhat higher bandwidth can be obtained with proportional-derivative or more sophisticated feedback, but the resonant behavior of the leadscrew mechanism remains a lim-

Table 5.1 Description of the system used in numerical examples.

leadscrew length	1 m
leadscrew average diameter	25 mm
leadscrew pitch	8 mm
leadscrew material	steel
thrust-bearing stiffness	500 N/μm
nut stiffness	600 N/μm
coupling torsional stiffness	150 kN·m
carriage damping factor	0.015
carriage mass	1000 kg
motor inertia	0.23 g·m^2

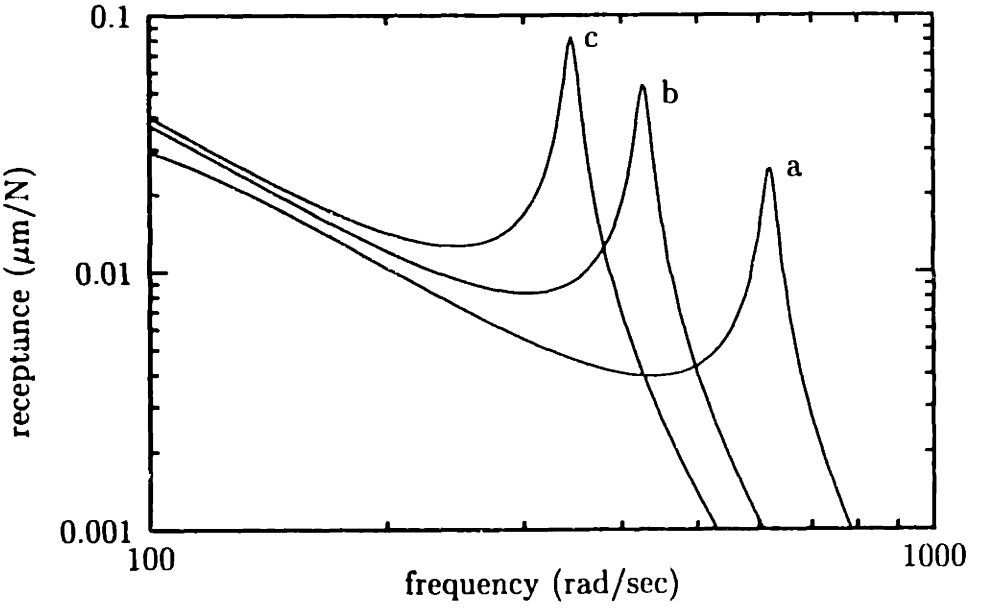

Figure 5.2 Frequency response of the example system with the leadscrew end unrestrained and the carriage positioned at (a)5 %, (b)50 %, and (c) 95% of its travel.

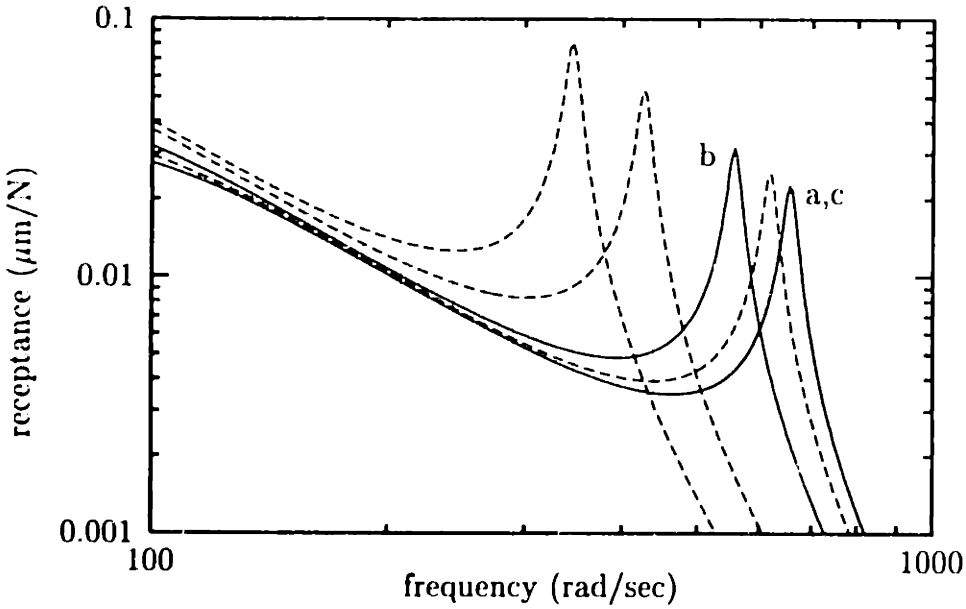

Figure 5.3 Frequency response of the example system with the leadscrew stretched rigidly against thrust bearings; the carriage is positioned at at (a) 5%, (b) 50%, and (c) 95% of its travel.

iting factor. It is therefore desirable to increase the resonant frequency and decrease the peak amplitude as much as possible.

An approach sometimes employed to increase rigidity is to use thrust bearings at both (2) and (3) and pre-stretch the screw in order to accommodate thermal expansion. Using this approach, the overall rigidity of the system can be increased, and the response of the system with the carriage near thrust bearing (3) is almost identical to that with the carriage near thrust bearing (2) as shown in Fig. 5.3. The disadvantage of this approach is that it requires that a prohibitively high preload be applied in stretching the screw. For our example system, a preload of approximately 25000 N is required to accommodate a temperature rise of 20°C. Such a high preload increases the starting torque and heat generation in the rotary support bearings and can appreciably warp the bed of the machine.

To obtain a lower preload, a relatively compliant medium such as a stack of Belville washers can be inserted into the preload path at (3). The preload

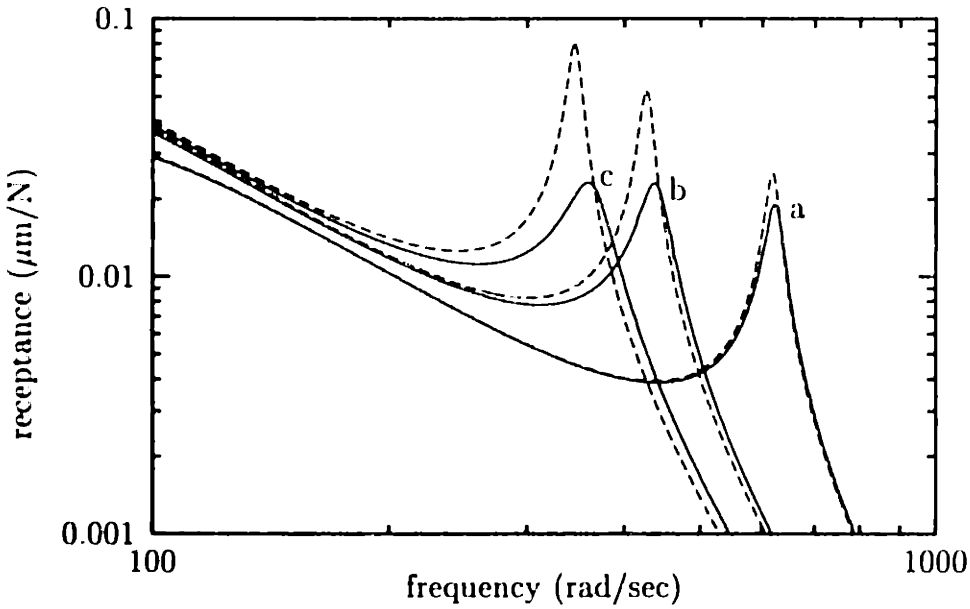

Figure 5.4 Frequency response of the example system with the leadscrew stretched against a damping element and thrust bearings; the carriage is positioned at (a) 5%, (b) 50%, and (c) 95% of its travel.

required to accommodate a given temperature rise drops directly with the stiffness of the preload medium, but so does the rigidity of the mechanism.

5.1.2 Damped Supports

In the present work, it is proposed that a damping element be placed in the preload path at (3). For a relatively compliant but lossy preload medium, significant attenuation of the resonant peak amplitude can be obtained as shown in Fig. 5.4. In this case a damping washer with 10 N/μm stiffness and a loss factor of 1.0 is employed, and the preload necessary to accommodate a 20°C temperature rise is approximately 2500 N.

By use of a compliant preload medium, we only marginally increase the rigidity of the mechanism, and therefore obtain resonant frequencies only slightly higher than those obtained with the leadscrew end unrestrained. But we have greatly increased the damping, especially when the carriage is posi-

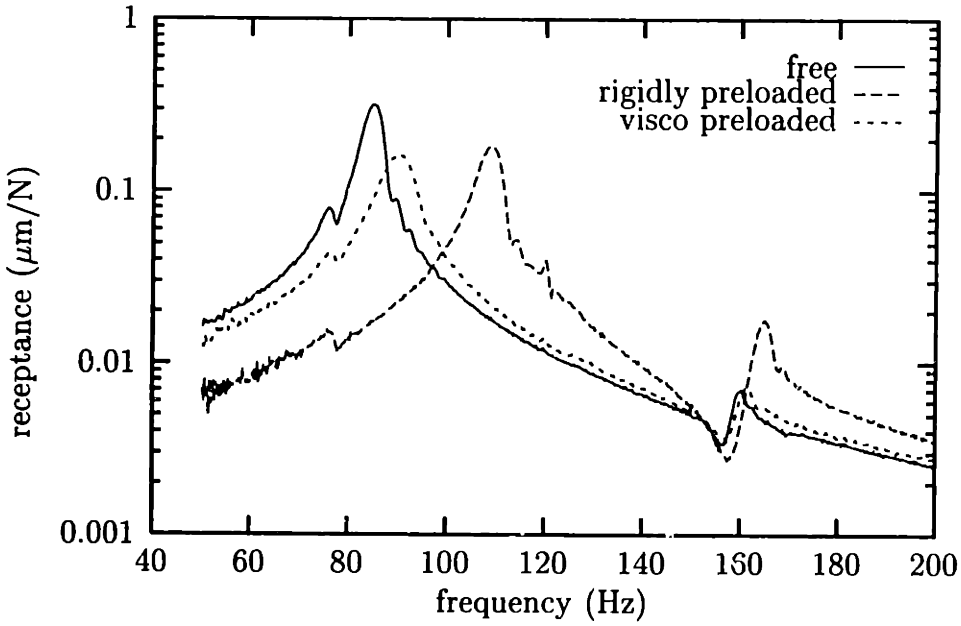

Figure 5.5 Measured receptances of the test slide with the shaft end free, preloaded rigidly against a pillow block, and preloaded via a viscoelastic washer against a pillow block.

tioned near the damped support bearing. The result is that the bandwidth achievable with proportional feedback is nearly independent of carriage position.

5.1.3 Test-Bed Results

A carriage weighing roughly 190 kg and mounted on Thomson Accuglide size 35 linear guides was clamped to a shaft with a free length of 20 inches and a diameter of 0.625 inches. One end of the shaft was rigidly loaded against a pillow block and the carriage was positioned near the opposite end of the shaft. An accelerometer was mounted to the carriage to measure axial vibration, and the carriage was struck with an instrumented hammer.

Measured receptances are shown in Fig. 5.5 for the cases where the second end of the shaft is free, preloaded rigidly against a pillow block, and preloaded via a viscoelastic washer against a pillow block. The resonant frequency and

	frequency (Hz)	loss factor
free	85.3	0.034
rigid preload	109.5	0.036
visco preload	90.5	0.078

Table 5.2 Resonant frequencies and damping ratios of the test slide.

loss factor for each case is shown in Table 5.2.

5.1.4 Design Notes

A leadscrew with a damped support is yet another example of the parallel-stack system of Fig. 2.1(c) where, with reference to Fig. 5.1, we identify the spring k_1 with the stiffness between the carriage and the motor through the thrust bearing (2) and the spring k_2 with that between the carriage and the motor through thrust bearing (3).

Examining Table 5.1, we see that although there are a number of contributors to the compliance of a leadscrew drive, by far most compliant element is the screw itself. Moreover, if the lead is small compared to the diameter, torsional wind up of the screw can be neglected in comparison with its axial deformation. Then, for a carriage positioned at location x along a leadscrew of length L, we have the stiffness ratio

$$Y = \frac{L}{L - x} \tag{5.1}$$

If the leadscrew has modulus E and average cross-sectional area A, the coupling parameter takes the form

$$g = \frac{k_v(L - x)}{EA} \tag{5.2}$$

where the viscoelastic preload medium has complex stiffness $k_v(1+j\eta_v)$. Using these parameters, all of the results derived in Section 2.2 can be used for design of a leadscrew system to have maximum damping at a given carriage location x.

But we are usually concerned with the performace of the drive over its entire range of travel, and we have seen that the damping is most important when the

carriage is at the end most distant from the drive motor. In that configuration (if we continue to treat the leadscrew as the only compliance in the system), we have the parallel system of Fig. 2.1(a) and both the damping and stiffness increase monotonically with the stiffness of the viscoelastic preload medium. Defining the stiffness ratio

$$Y = \frac{k_v L}{EA} \tag{5.3}$$

and using the expression for the complex stiffness of a parallel system given in Eq. (2.10), we write the system loss factor as

$$\eta = \frac{Y}{1+Y}\eta_v \tag{5.4}$$

But the preload force P necessary to accomodate a given temperature rise ΔT also increases monotonically with the stiffness of the preload medium according to

$$\frac{P}{EA\alpha\Delta T} = \frac{Y}{1+Y} = \frac{\eta}{\eta_v} \tag{5.5}$$

where α is the coefficient of thermal expansion of the leadscrew. We in general choose the preload medium to have as high a stiffness as possible without requiring an unacceptably large preload force.

CHAPTER 6

Sensitivity Analysis in Structural Modeling and Optimization

6.1 Background

Sensitivity analysis is an invaluable tool in any design activity because it allows the designer to determine the most profitable areas for improvement of performance. In an automated setting, it forms the basis for almost all parametric optimization methods. We can also use sensitivity analysis to gauge the effects of uncertainties such as manufacturing tolerances on the final performance of a product.

In this chapter, we begin with a detailed review of the various methods for computing the sensitivities of structural response to changes in design. Then we present a detailed discussion of the application of these methods in conjunction with the finite-element method and present some numerical examples. Finally, we give examples of how sensitivity analysis can be used to reconcile analytical models with experimental data and to redesign structures for improved performance.

6.2 Theory of Design Sensitivity Analysis

In this section, we provide a detailed review of the theory of design sensitivity analysis. We begin with the general finite-difference calculation, then move on

to analytical methods for the determination of static-response and eigenvalue sensitivities. The development here closely follows that of Haug et al. (1986).

6.2.1 Overall Finite Differences

A straightforward way to estimate the derivative with respect to a parameter p of any function $\psi(p)$ is to use finite differences. In its simplest incarnation, the finite-difference approximation to the derivative of a function $\psi(p)$ is

$$\frac{d\psi(p)}{dp} = \frac{\psi(p+\delta p) - \psi(p)}{\delta p} \tag{6.1}$$

The main advantage of this method is simplicity. The only requirement is that we be able to determine $\psi(p)$ in the neighborhood of the values of p that we are interested in. There are, however, no guarantees of the accuracy of the results and the cost of such computations for a large number of design variables is prohibitive.

6.2.2 Static Response Sensitivity

In this section, we discuss several methods for computation of the derivatives of the static response of a structure with respect to design parameters. All but one of the methods is completely analytical (i.e., exact) and, in the context of finite-element analysis for linear systems, they are all more computationally efficient than overall finite differences.

Direct Differentiation

Consider the problem of determining the static response z of a discrete system which depends on a vector p of parameters

$$K(p)z = F(p) \tag{6.2}$$

where $K(p)$ is the stiffness matrix and $F(p)$ is the load vector. If $K(p)$ is positive definite and the elements of $K(p)$ and $F(p)$ are differentiable with respect to p, then the implicit-function theorem guarantees that the response z is also differentiable with respect to p.

In most practical problems, we are concerned with an objective function

$$\psi = \psi(p, z(p)) \tag{6.3}$$

that depends on the design parameters both directly and via the response. The total derivative of this equation is given by

$$\frac{d\psi}{dp} = \frac{\partial\psi}{\partial p} + \frac{\partial\psi}{\partial z}\frac{dz}{dp} \tag{6.4}$$

The first term on the right-hand side, $\partial\psi/\partial p$, is usually easy to compute explicitly. To develop an expression for the remaining term, we introduce the derivative of the governing equation (6.2)

$$K\frac{dz}{dp} + \frac{\partial K}{\partial p}z = \frac{\partial F}{\partial p} \tag{6.5}$$

Recalling that K is positive definite and hence invertible, we can write

$$\frac{dz}{dp} = K^{-1}\left[\frac{\partial F}{\partial p} - \frac{\partial K}{\partial p}z\right] \tag{6.6}$$

and substitute into Eq. (6.4)

$$\frac{d\psi}{dp} = \frac{\partial\psi}{\partial p} + \frac{\partial\psi}{\partial z}K^{-1}\left[\frac{\partial F}{\partial p} - \frac{\partial K}{\partial p}z\right] \tag{6.7}$$

This equation is usually impractical to implement because it requires inversion of K, which is often a matrix of very large order. Therefore, a more common approach is to solve Eq. (6.5) for dz/dp and substitute the result into Eq. (6.4).

This procedure for computation of the derivatives involves solving the original problem for each load of interest, then solving Eq. (6.5) for each load and design variable of interest, and assembling the results into Eq. (6.4) for each element of the objective function ψ.

Adjoint Method

It is often useful to introduce an adjoint equation given by

$$K(p)\lambda = \frac{\partial\psi^T}{\partial z} \tag{6.8}$$

This equation is of the same form as the governing equation (6.2), and can be interpreted as solving the original problem with an adjoint load $\partial\psi^T/\partial z$.

Because we have already solved the original problem, a factored form of $K(p)$ is available, and it costs us little to solve for λ. We can now use the adjoint equation to write Eq. (6.7) as

$$\frac{d\psi}{dp} = \frac{\partial\psi}{\partial p} + \lambda^T \left[\frac{\partial F}{\partial p} - \frac{\partial K}{\partial p} z\right] \tag{6.9}$$

and use this equation to compute the sensitivity of the objective ψ to changes in design.

The procedure for computation of the derivatives via the adjoint method is to solve the original problem for each loading condition of interest, solve the adjoint problem for each element of the objective ψ, and then assemble the results into the above equation for each design variable of interest. Therefore, unless the dimension of objective ψ is larger than the product of the number of design variables and the number of loading conditions, the adjoint method is more efficient than the direct method.

Semi-Analytical Methods

The main difficulty in applying either the adjoint or direct methods is the need to compute $\partial K/\partial p$ and $\partial F/\partial p$. Usually, F and K are obtained from a finite-element model and analytical expressions in terms of the design variables are unavailable. If the finite-element code is accessible and the element matrices are implicitly generated, the derivatives of the individual elements can be assembled in the same manner as the element matrices were assembled, yielding exact expressions for the derivatives. This approach is usually difficult to implement in conjunction with a commercial finite-element program, and is very difficult to implement if the element matrices are determined by numerical integration rather than implicit methods.

A simple alternative is to use finite-differences to determine the elements of the derivative matrices. Using simple forward differencing, we can write

$$\frac{\partial K(p)}{\partial p} \approx \frac{K(p+\delta p) - K(p)}{\delta p} \tag{6.10}$$

This calculation must be repeated for every element of p at considerable cost, especially if the variation of p requires re-meshing of the finite-element model. In addition, the accuracy of the results are suspect (Haftka et al., 1990), even when the step size δp is chosen carefully.

Variational Method

In this method, we avoid the computation of the derivatives of the element matrices by computing the derivatives of the distributed-parameter system before discretization into finite elements. The resulting formulae can then be discretized for convenient computation. Yang and Botkin (1986) discuss the relationship between the variational and direct methods.

We begin with the variational formulation for the governing equations of linear elastic problems (i.e., the principle of virtual work)

$$a_p(z, \bar{z}) = l_p(\bar{z}) \tag{6.11}$$

where $a_p(z, \bar{z})$ is the energy bilinear form representing the strain energy of the system, $l_p(\bar{z})$ represents the loading, and $\bar{z}$ is a virtual displacement that satisfies the kinematic boundary conditions of the system. Parametric dependence on p is indicated by the subscript p. (An example is given in the section on eigenvalue sensitivities.)

The response z depends on position x, and the parameters $p(x)$. The variation of z in the direction δp can be written as

$$z'(x; p, \delta p) = \frac{d}{d\epsilon} \left[z(x; p + \epsilon \delta p) \right]_{\epsilon=0} \tag{6.12}$$

and the variation of a can be written as

$$a'_{\delta p}(z, \bar{z}) = \frac{d}{d\epsilon} \left[a_{p+\epsilon\delta p} \left(z(x, p), \bar{z} \right) \right]_{\epsilon=0} \tag{6.13}$$

Recalling the well-known property from calculus of variations that the order of partial differentiation and variation can be interchanged, we can write

$$\frac{d}{d\epsilon} \left[a_{p+\epsilon p} \left(z(x; p + \epsilon\delta p), \bar{z} \right) \right]_{\epsilon=0} = a'_{\delta p}(z(x; p), \bar{z}) + a_p(z', \bar{z}) \tag{6.14}$$

We can now take the variation of both sides of Eq. (6.11) and write the result as

$$a_p(z', \bar{z}) = l'_{\delta p}(\bar{z}) - a'_{\delta p}(z, \bar{z}) \tag{6.15}$$

which is of the same form as the original system in Eq. (6.11). Thus, we can solve for z' by solving the original problem with a loading obtained from the variations of the load and energy forms.

We now introduce an objective functional that can be expressed as an integral of a function the displacement, its gradient, and design,

$$\psi = \int_\Omega g(z, \nabla z, p)\, d\Omega \tag{6.16}$$

where Ω denotes the volume of the structure. This form allows us to accommodate objectives involving displacements, stresses, and strains. Point values can be obtained by introducing the Dirac δ. The variation of the objective functional is given by

$$\psi' = \int_\Omega \left(\frac{\partial g}{\partial z} z' + \frac{\partial g}{\partial (\nabla z)} \nabla z' + \frac{\partial g}{\partial p} \delta p \right) d\Omega \tag{6.17}$$

To deal with the first two terms in the integrand, we find it convenient to introduce an adjoint equation

$$a_p(\lambda, \bar{\lambda}) = \int_\Omega \left(\frac{\partial g}{\partial z} \bar{\lambda} + \frac{\partial g}{\partial (\nabla z)} \nabla \bar{\lambda} \right) d\Omega \tag{6.18}$$

whose right-hand side consists simply of the terms of interest with z' replaced by the virtual displacement $\bar{\lambda}$.

Now, if we set the virtual displacement in Eq. (6.15) equal to λ and use the symmetry of a, we have

$$a_p(\lambda, z') = l'_{\delta p}(\lambda) - a'_{\delta p}(z, \lambda) \tag{6.19}$$

whose left-hand side is equal to that of the previous equation with $\bar{\lambda}$ replaced by z'. Thus, we have

$$\int_\Omega \left(\frac{\partial g}{\partial z} z' + \frac{\partial g}{\partial (\nabla z)} \nabla z' \right) d\Omega = l'_{\delta p}(\lambda) - a'_{\delta p}(z, \lambda) \tag{6.20}$$

Substituting into the expression for ψ', we obtain the desired result

$$\psi' = \int_\Omega \frac{\partial g}{\partial p} \delta p \, d\Omega + l'_{\delta p}(\lambda) - a'_{\delta p}(z, \lambda) \tag{6.21}$$

which allows us to determine the variation of a response functional in terms of the variations of the system operators evaluated at the solution of an adjoint problem. We will delay presentation of an example of variational sensitivity analysis until the section on eigenvalue sensitivity.

6.2.3 Eigenvalue Sensitivity

In this section, we discuss methods for computation of the sensitivities of the eigenvalues of structures. These methods are in rough correspondence to the methods presented for static analysis. The principal differences are that the load is now replaced by a D'Alembert force representing the inertia and that it is unnecessary to introduce an adjoint equation.

Direct Method

A discrete eigenvalue problem for natural frequency can be written in the form

$$K(p)y = \zeta M(p)y \tag{6.22}$$

where K is the stiffness matrix, M is the inertia matrix, ζ is an eigenvalue, and y is the associated eigenvector. It is shown by Haug et al. (1986) that simple eigenvalues are differentiable with respect to design if K and M are symmetric, positive definite, and differentiable.

We begin by differentiating with respect to p to yield

$$\frac{\partial K}{\partial p}y + K\frac{dy}{dp} = \frac{d\zeta}{dp}My + \zeta\frac{\partial M}{\partial p}y + \zeta M\frac{dy}{dp} \tag{6.23}$$

Next, we premultiply by y^T and take advantage of the symmetry of M and K to write

$$y^T My\frac{d\zeta}{dp} = y^T\left(\frac{\partial K}{\partial p} - \zeta\frac{\partial M}{\partial p}\right)y + \frac{dy}{dp}(K - \zeta M)\,y \tag{6.24}$$

Noting that the second term on the right-hand side is zero for a solution of the original eigenproblem, we have the desired result

$$\frac{d\zeta}{dp} = \frac{y^T\left(\frac{\partial K}{\partial p} - \zeta\frac{\partial M}{\partial p}\right)y}{y^T My} \tag{6.25}$$

Thus, if we can evaluate the derivatives of K and M with respect to p, it is an extremely simple matter to compute the derivatives. Because the eigenvalue problem is self adjoint, it turns out to be much simpler to calculate derivatives of the eigenvalues than the derivatives of static response.

We are, however, still faced with the difficulty of determining the derivatives of the element matrices K and M. As in the case of static response, we

can introduce a semi-analytical method which uses finite differences, or we can compute the derivatives of the elements in our finite element code. The same difficulties that were mentioned in the case of static response arise in either case. A better approach is to use variational techniques.

Variational Method

As in the case of static response sensitivity, we avoid differentiating the element matrices by differentiating the governing equations before discretization. We represent the eigenvalue problem as

$$a_p(y, \bar{y}) = \zeta d_p(y, \bar{y}) \tag{6.26}$$

where, as in the static analysis, $a_p(y, \bar{y})$ is a bilinear form for the strain energy and $\bar{y}$ is a virtual displacement. The bilinear form $d_p(y, \bar{y})$ represents the kinetic energy in the system.

Again, we introduce the prime notation for variations in the δp direction

$$\zeta'(p, \delta p) = \frac{d}{d\epsilon} \left[\zeta(p + \epsilon \delta p)\right]_{\epsilon=0} \tag{6.27}$$

Taking the variation of both sides of Eq. (6.26), we write

$$a_p(y', \bar{y}) + a'_{\delta p}(y, \bar{y}) = \zeta' d_p(y, \bar{y}) + \zeta d_p(y', \bar{y}) + \zeta d'_{\delta_p}(y, \bar{y}) \tag{6.28}$$

This equation is an identity for any admissible function $\bar{y}$, so we can evaluate it at $\bar{y} = y$ to get

$$\zeta' d_p(y, y) = a'_{\delta p}(y, y) - \zeta d'_{\delta p}(y, y) - [a_p(y, y') - \zeta d_p(y, y')] \tag{6.29}$$

where we have taken advantage of the symmetry of a_p and d_p. The second term on the right-hand side must be zero for an eigensolution of Eq. (6.26), so that we can write

$$\zeta' = \frac{a'_{\delta p}(y, y) - \zeta d'_{\delta p}(y, y)}{d_p(y, y)} \tag{6.30}$$

which gives the intuitive result that, for a given design change (δp), the change in an eigenvalue (natural frequency) is proportional to the difference between the gain in strain energy and the gain in kinetic energy evaluated on the unperturbed eigenfunction (mode shape).

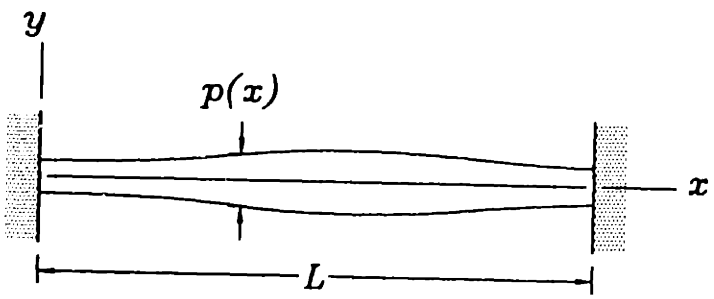

Figure 6.1 Clamped–clamped beam with varying thickness.

As an example, consider the clamped–clamped beam with rectangular cross-section of variable height $p(x)$ shown in Fig. 6.1. The well-known differential form of the equation for natural vibration of an Euler–Bernoulli beam is

$$\frac{\partial^2}{\partial x^2}\left(EI(p;x)\frac{\partial^2 y}{\partial x^2}\right) = \zeta \rho A(p;x) y \tag{6.31}$$

where ρ is the mass density of the beam, E is its Young's modulus, $A(p;x) = bp(x)$ is the cross-sectional area, and $I(h;x) = bp^3(x)/12$. If we multiply by the virtual displacement $\bar{y}$ and integrate the left-hand side by parts twice, we obtain the variational equation

$$\int_0^L EI(p;x)\frac{\partial^2 y}{\partial x^2}\frac{\partial^2 \bar{y}}{\partial x^2}\,dx = \zeta \int_0^L \rho A(p;x) y\bar{y}\,dx \tag{6.32}$$

Alternatively, this equation could have been derived directly from the principle of virtual work.

We note that in the notation of Eq. (6.26) we have

$$a_p(y,\bar{y}) = \int_0^L EI(p;x)\frac{\partial^2 y}{\partial x^2}\frac{\partial^2 \bar{y}}{\partial x^2}\,dx \tag{6.33}$$

and

$$d_p(y,\bar{y}) = \int_0^L \rho A(p;x) y\bar{y}\,dx \tag{6.34}$$

Taking the variations of these expression with respect to p, and substituting into Eq. (6.26), we obtain

$$\zeta' = \int_0^L E\frac{\partial I}{\partial p}\left(\frac{\partial^2 y}{\partial x^2}\right)^2 \delta p\,dx - \zeta \int_0^L \rho \frac{\partial A}{\partial p} y^2\,\delta p\,dx \tag{6.35}$$

where we have assumed that the eigenvectors have been mass normalized so that $d_p(y, y) = 1$. The partial derivatives of I and A can be evaluated to yield

$$\zeta' = \int_0^L \left[\frac{Ebp^2}{4} \left(\frac{\partial^2 y}{\partial x^2} \right)^2 - \zeta \rho b y^2 \right] \delta p \, dx \tag{6.36}$$

For a given eigenvalue ζ and its eigenfunction y, this formula can be used to compute the rate of change of ζ in any direction $\delta p(x)$. It shows that in order to raise the natural frequency of the beam, material should be added where the curvature is large and removed where the amplitude of motion is large.

6.3 Eigenvalue Sensitivities and the Finite Element Method

In this section, we illustrate the application of the various sensitivity methods in conjunction with the finite-element method. We consider planar vibration of the machine shown in Fig. 6.2. The machine structure consists of two box-section beams with wall thicknesses of 1 cm, height h and depth b. The beams are joined by a linear bearing with rotational compliance k_2 and the machine is mounted to a rigid base by a joint with rotational compliance k_1. We assume that the vertical actuation of the horizontal arm is effectively rigid for the first few modes.

6.3.1 Finite-Element Model

We construct a finite-element model of the structure from cubic beam elements by segmenting the column and bridge respectively into four and three elements. The stiffness relation of the beam element is given by

$$\begin{Bmatrix} F_1 \\ M_1 \\ F_2 \\ M_2 \end{Bmatrix} = \frac{EI}{\ell^3} \begin{bmatrix} 12 & 6\ell & -12 & 6\ell \\ 6\ell & 4\ell^2 & -6\ell & 2\ell^2 \\ -12 & -6\ell & 12 & -6\ell \\ 6\ell & 2\ell^2 & -6\ell & 4\ell^2 \end{bmatrix} \begin{Bmatrix} y_1 \\ \theta_1 \\ y_2 \\ \theta_2 \end{Bmatrix} \tag{6.37}$$

The deflection of the element is given by a cubic polynomial of the form

$$y(x) = p_1 + p_2\xi + p_3\xi^2 + p_4\xi^3 \tag{6.38}$$

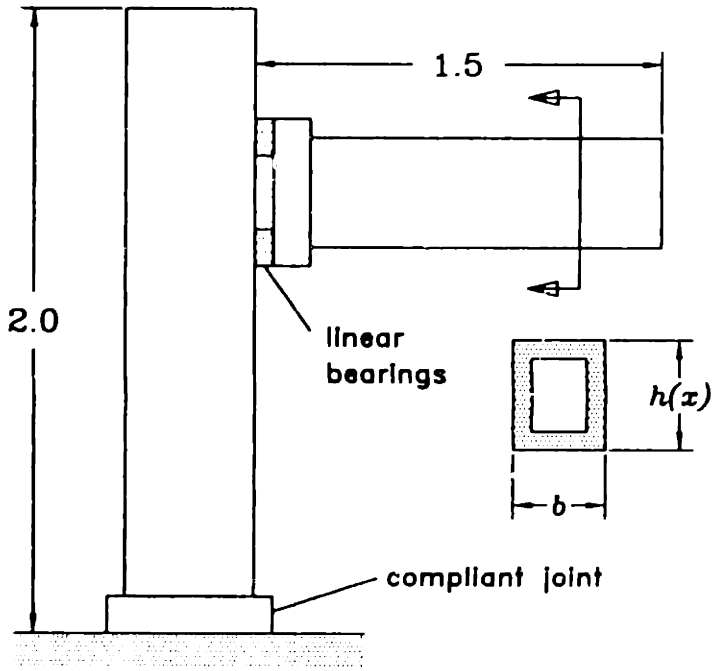

Figure 6.2 Layout of the example machine (dimensions given in meters).

where $\xi = x/\ell$. The coefficients p_i can be obtained from the coordinates of the element via the transformation

$$\begin{Bmatrix} p_1 \\ p_2 \\ p_3 \\ p_4 \end{Bmatrix} = \begin{bmatrix} 1 & 0 & 0 & 0 \\ 0 & 1 & 0 & 0 \\ -3 & -2 & 3 & -1 \\ 2 & 1 & -2 & 1 \end{bmatrix} \begin{Bmatrix} y_1 \\ \theta_1 \\ y_2 \\ \theta_2 \end{Bmatrix} \tag{6.39}$$

and therefore the consistent mass matrix is given by

$$\frac{\rho A \ell}{420} \begin{bmatrix} 156 & 22\ell & 54 & -13\ell \\ 22\ell & 4\ell^2 & 13\ell & -3\ell^2 \\ 54 & 13\ell & 156 & -22\ell \\ -13\ell & -3\ell^2 & -22\ell & 4\ell^2 \end{bmatrix} \tag{6.40}$$

The finite-element program assembles these matrices by adding up the forces associated with each degree of freedom to form the system mass and stiffness matrices.

We consider a nominal design with section depth $b_i = 20$ cm for all seven elements, section heights $h_i = 20$ cm for the column, and section heights $h_i = 10$ cm for the arm. The compliance of the base is $k_1 = 20 \times 10^6$ N·m and the compliance of the bearing is $k_2 = 5 \times 10^6$ N·m. The wall thickness is fixed at 10 mm. The first four natural frequencies and mode shapes are shown in Fig. 6.3. Next, we give detailed descriptions of the computation of the sensitivities of the eigenvalues to changes in h_i, k_1, and k_2.

6.3.2 Direct Differentiation

We wish to implement the method described in Section 6.2.3 for the model developed in the previous section. As discussed in Section 6.2.3, it is easy to compute the sensitivity via Eq. (6.25) if we have evaluated $\partial K/\partial p$ and $\partial M/\partial p$.

Since we have generated the elements explicitly and we have written the finite element code, it is a simple matter to assemble the derivatives of the individual elements to form $\partial K/\partial p$. For example, if we want the sensitivity to changes in the height of the cross-section of the kth element, the derivative of its stiffness matrix is

$$\frac{\partial I}{\partial h_k} \frac{E}{\ell^3} \begin{bmatrix} 12 & 6\ell & -12 & 6\ell \\ 6\ell & 4\ell^2 & -6\ell & 2\ell^2 \\ -12 & -6\ell & 12 & -6\ell \\ 6\ell & 2\ell^2 & -6\ell & 4\ell^2 \end{bmatrix} \tag{6.41}$$

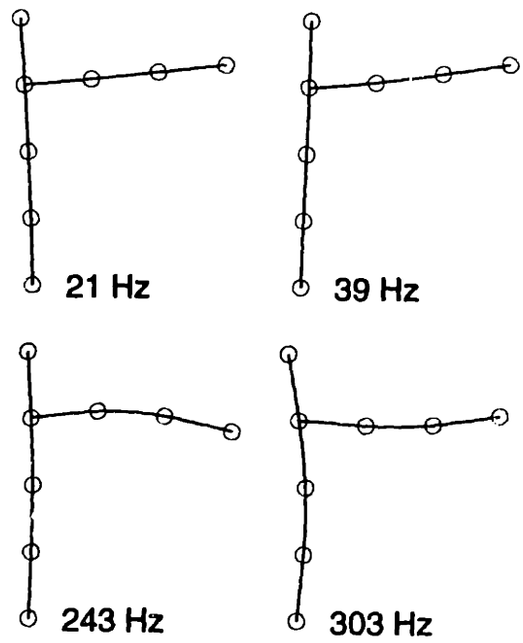

Figure 6.3 First four natural frequencies and mode shapes for the nominal design.

and the derivative of its mass matrix is

$$\frac{\partial A}{\partial h_k}\frac{\rho\ell}{420}\begin{bmatrix} 156 & 22\ell & 54 & -13\ell \\ 22\ell & 4\ell^2 & 13\ell & -3\ell^2 \\ 54 & 13\ell & 156 & -22\ell \\ -13\ell & -3\ell^2 & -22\ell & 4\ell^2 \end{bmatrix} \tag{6.42}$$

If any other elements of the system matrices depend on h_k, their derivatives can likewise be computed and assembled with the above expressions to form $\partial K/\partial h_k$ and $\partial M/\partial h_k$. The assembly procedure here is precisely the same as it was for assembling the matrices K and M.

Application of this procedure for each of the h_k and substitution into Eq. (6.25) yields the results shown in Fig. 6.4.

6.3.3 Variational Method

If we are using a commercial software package or numerically generated elements, calculation of the derivatives of the system matrices as demonstrated in the foregoing is impractical. In this case, we find it considerably simpler to apply the variational method for determination of the sensitivities. As shown in Section 6.2.3, the eigenvalue sensitivity can be determined from the partial derivatives of the strain and kinetic energies with respect to design parameters.

The strain energy of our machine is the sum of the strain energy in each of the seven elements of our model. Using the expression for strain energy of a beam derived in Section 6.2.3, we write

$$a_p(y,y) = \sum_{k=1}^{7} EI(h_k)\left[\int_0^\ell \left(\frac{\partial^2 y}{\partial x^2}\right)^2 dx\right]_k + k_1\theta_1^2 + k_2(\theta_6-\theta_4)^2 \tag{6.43}$$

where the last two terms account for the strain energy in the joint and bearing. Similarly, the inertia form can be written as

$$d_p(y,\bar{y}) = \sum_{k=1}^{7} \rho A(h_k)\left[\int_0^\ell (\hat{x}^2+y^2)\,dx\right]_k \tag{6.44}$$

where $\hat{x}$ is the axial displacement, which is nonzero along the horizontal arm. The integrals of the functions $\hat{x}$, y, and $\partial^2 y/\partial x^2$ are usually readily available from commercial software packages so that these expressions can be easily evaluated.

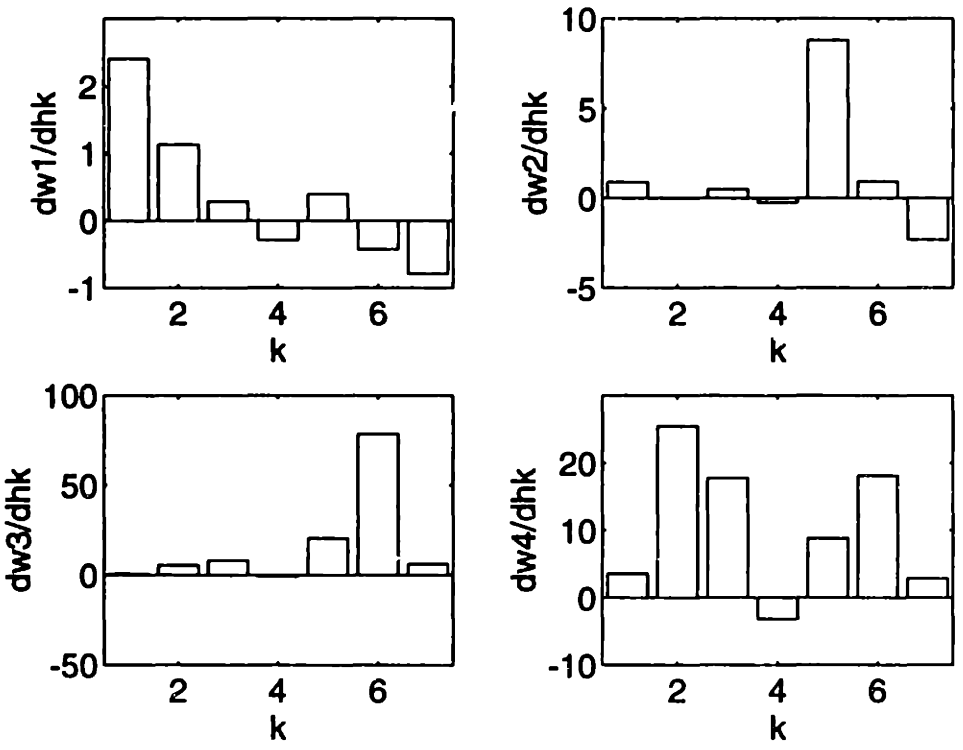

Figure 6.4 Sensitivities $\partial\omega_i/\partial h_k$ for the first four modes (rad/sec/cm).

In the case of our finite-element program, we use the transformation given by Eq. (6.39) along with Eq. (6.38) to evaluate $y(x)$ in terms of the y_i and θ_i and integrate in closed form to evaluate the necessary expressions. The derivative with respect to h_j can be written as

$$\frac{\partial \zeta}{\partial h_k} = E\frac{\partial I}{\partial h_k}\left[\int_0^\ell \left(\frac{\partial^2 y}{\partial x^2}\right)^2 dx\right]_k - \zeta\rho\frac{\partial A}{\partial h_k}\left[\int_0^\ell (\hat{x}^2 + y^2)\, dx\right]_k \tag{6.45}$$

This formula can be applied directly to our example problem yielding results identical to those obtained from the direct method, which is as expected because both methods are exact.

6.3.4 Overall Finite Differences

The simplest method for computation of the sensitivities is overall finite differences. Here, we simply vary the parameters of interest, recompute the eigenvalues, and estimate the derivatives. Our example problem is well suited to this approach because we do not have a large number of design variables and we do not need to re-mesh. Nonetheless, we find that significant errors can occur when finite differences are used.

In Fig. 6.5, we show the errors obtained for the derivatives of the natural frequencies with respect to h_i. Of course, the errors obtained are functions of the step size. We illustrate this in Fig. 6.6, where we show the finite-difference approximations for $\partial\omega_i/\partial k_2$ for the first four modes as a function of δk_2.

6.4 Applications

In this section, we apply the methods discussed in the foregoing to two problems that commonly arise in the machine-design process. First, the finite-element model of a machine seldom predicts the machine dynamics in satisfactory agreement with the measured response and hence methods are required for updating the model to give reasonable agreement. Second, once a satisfactory model is obtained, we wish to to improve performance by some design change, and we need some guidance in finding the "best" change for our particular objectives.

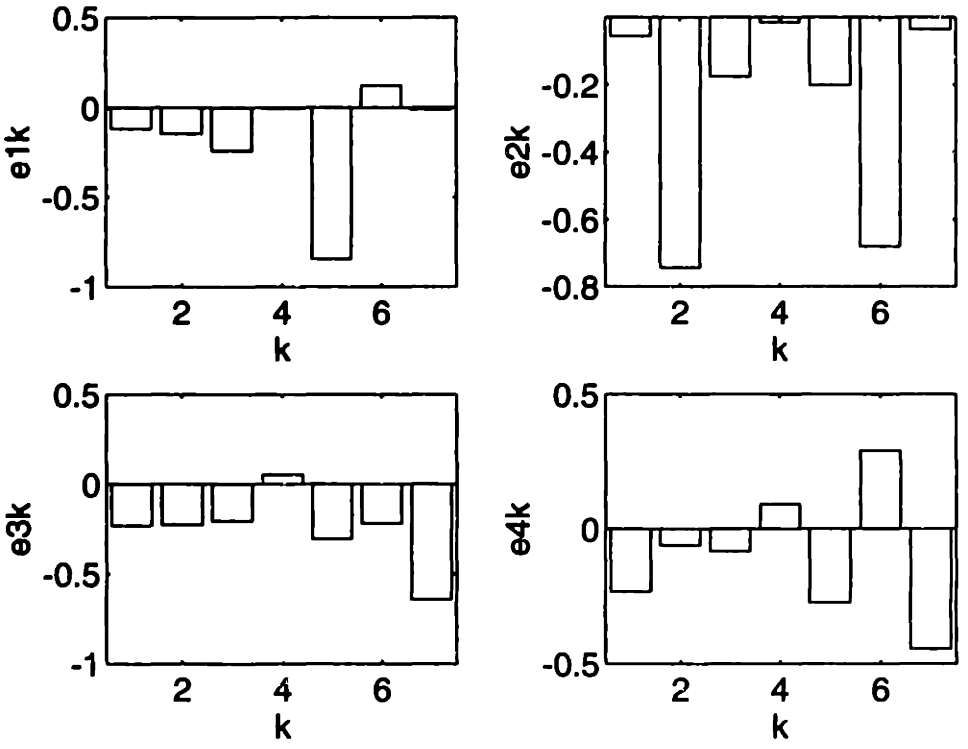

Figure 6.5 Per cent error e_{ik} in $\partial\omega_i/\partial h_k$ computed by finite differences with a step size of $\delta h = 0.5$ mm for the first four modes.

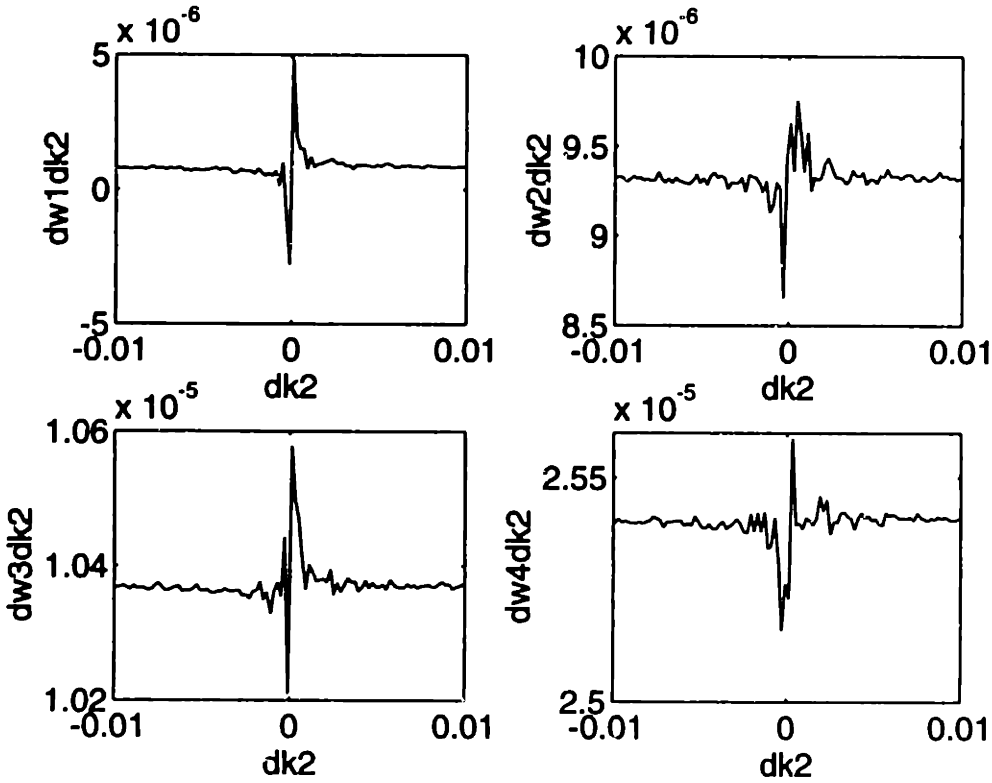

Figure 6.6 Finite-difference approximations to $\partial\omega_i/\partial k_2$ (rad/sec/N·m) as a function of δk_2 (N·m).

6.4.1 Model Update

In modeling the dynamics of a machine such as that shown in Fig. 6.2, it is not uncommon to have grossly mis-estimated the stiffnesses of the bearings and joints. These elements of a machine are inherently difficult to model, and empirical data is usually unreliable.

In a typical scenario, we will have a finite-element model with thousands of elements for the structure and a few uncertain parameters for the joint and bearing stiffnesses; and we need to reconcile the model with experimental data. Of the experimental results, the most reliable measurements are the natural frequencies, and so it is desirable to use the errors in predicted natural frequencies for identification of the uncertain parameters.

In this context, mode-shape measurements serve an important purpose: they allow us to match the natural frequencies of corresponding modes from the analytical and experimental models. If a machine possesses modes with closely-spaced frequencies, then moderate errors in the uncertain parameters may cause the ordering of modes to be reversed, so that we cannot simply match the nth mode of the analytical model to the nth mode of the experimental model. In our example, we will not have any problems of this nature. For a discussion of correlation methods, see Imregun and Visser (1989).

To illustrate the sensitivity approach to model update, we again consider the example machine of Fig. 6.2. Suppose that we have measured the first four natural frequencies from an experiment and found them to be equal to those shown in Fig. 6.3. Now further suppose that we have overestimated k_1 by a factor of two and underestimated k_2 by a factor of two, but have correctly characterized the remaining components of the structure.

Using the "incorrect" parameter values, we find that the percentage errors in the first four modes are 4.6, -8.5, -2.3, and 1.5. The sensitivities of the natural frequencies to changes in k_1 and k_2 can be used to write

$$\Delta\vec{\omega} = S\Delta\vec{k} \tag{6.46}$$

where $\vec{\omega} = [\omega_1, \omega_2, \omega_3, \omega_4]^T$, $\vec{k} = [k_1, k_2]^T$, and the elements of S are

$$s_{ij} = \frac{\partial \omega_i}{\partial k_j} \tag{6.47}$$

Given an error $(-\Delta\vec{\omega})$ that we wish to eliminate, a least-squares correction $\Delta\vec{k}$ is given by

$$\Delta\vec{k} = (S^T S)^{-1} S^T \Delta\vec{\omega} \tag{6.48}$$

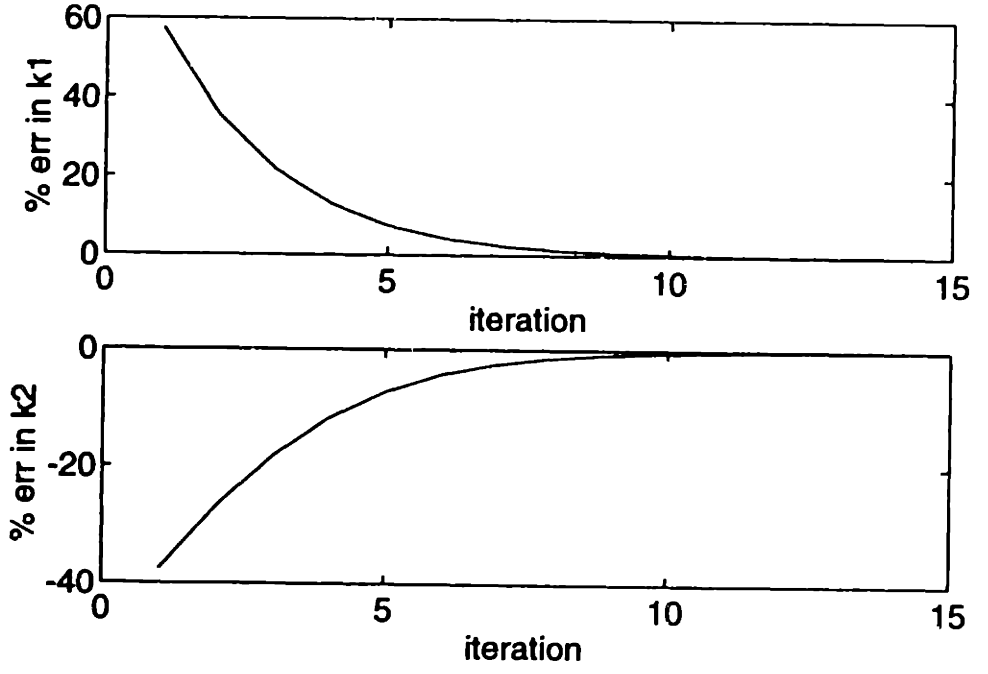

Figure 6.7 Convergence of parameters k_1 and k_2.

This forms the basis of an iterative procedure where the errors and sensitivities are evaluated, a small correction is made in the direction $\Delta\vec{k}$, and the process is repeated.

If we compute the sensitivity matrix via the direct method, and carry out this procedure for the example problem, and find that the parameter values quickly converged to their "true" values. Plots of the errors against iteration number are shown in Fig. 6.7. An important feature of this problem is that we have measured four independent values but only need to update two parameters. This gives us an important advantage when there are unexpected errors in the system.

To illustrate this point, we again consider our example machine with the same errors in k_1 and k_2, but now also introduce an "incorrect" element height vector $h = [0.3, 0.2, 0.2, 0.1, 0.1, 0.1, 0.1]^T$ m. (The "true" height vector is still $h = [0.2, 0.2, 0.2, 0.2, 0.1, 0.1, 0.1]^T$ m.) If we do not recognize that we have

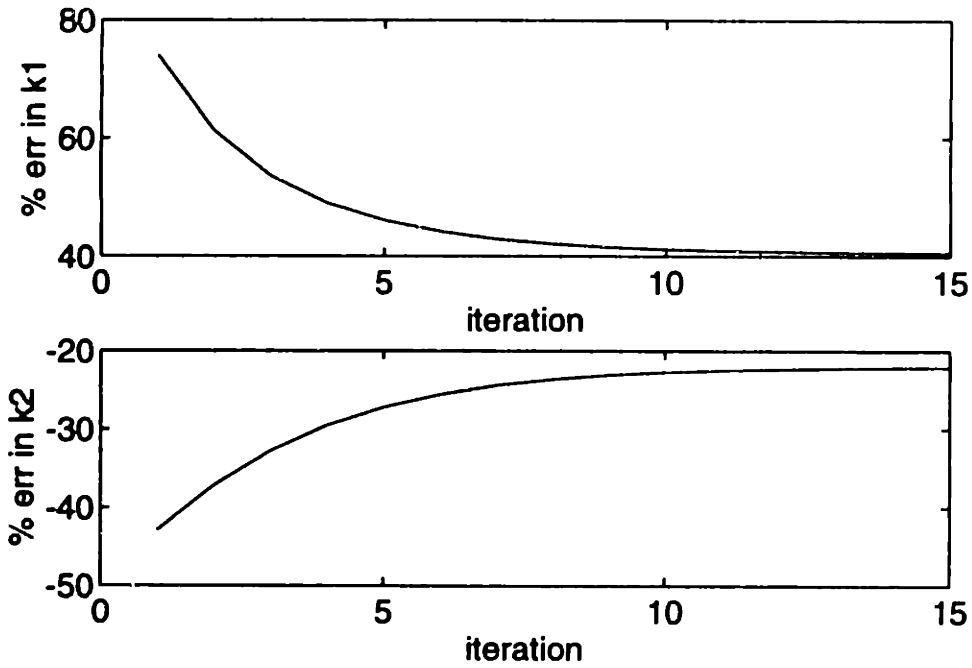

Figure 6.8 Convergence of k_1 and k_2 to incorrect values.

modeling errors in h and simply run our model-update program on k_1 and k_2, they converge to "incorrect" values as shown in Fig. 6.8. The final errors in the natural frequencies are found to be 17.6, 2.9, -0.32, and -0.2 percent.

If we had used only two measurements to correct our two unknown parameters, then the natural frequencies could still converge to the "true" values as k_1 and k_2 converge to incorrect values, and we would not realize that the update failed. However, when we use more measurements (e.g., four natural frequencies as opposed to two) the natural frequencies cannot converge to their true values unless k_1 and k_2 converge to correct values, which gives us a check on the validity of the model update.

6.4.2 Redesign

Having obtained a model of acceptable accuracy, we may wish to improve the performance by changing the design. In this exercise, we will consider the bearing and joint stiffnesses to be fixed and consider variations in the h_i to improve the first natural frequency. Any realistic design optimization must include constraints in order to obtain reasonable results. However, in cases where the designer is monitoring the progress of the iteration, manual intervention can guide the design towards reasonable results.

We can use the eigenvalue sensitivities to write an expression for the change in ω_1 for a small design change $\Delta\vec{h}$

$$\Delta\omega_1 = \left[\frac{\partial\omega_1}{\partial\vec{h}}\right]\Delta\vec{h} \tag{6.49}$$

If we constrain the magnitude of the design change so that $[\Delta\vec{h}]^T[\Delta\vec{h}] = \alpha^2$, then the largest $\Delta\omega_1$ will result when $\Delta\vec{h}$ is in the same direction as $\partial\omega_1/\partial\vec{h}$. This forms an iterative procedure to increase ω_1.

We use the direct method to compute the sensitivities and perform ten iterations of this procedure with $\alpha = 0.02$. The initial and final height vectors are shown in Fig. 6.9. The value of ω_1 increases steadily during the first ten iterations, as shown in Fig. 6.10. If the iteration is allowed to continue without constraints, it will eventually lead to negative values for h_7.

6.5 Application Notes

In this chapter, we have provided a review of powerful techniques for structural design sensitivity. These techniques form the basis for structural optimization or redesign as well as model-update methods.

We have attempted to present both a sound exposition of the theory behind the techniques and a tutorial enabling the reader to apply the methods in conjunction with the finite-element method for structural analysis. If the analyst has access to the inner workings of the finite-element code, the so-called direct methods are advantageous, otherwise it is most practical to apply variational methods. Of course, it is always possible but inefficient (and possibly inaccurate) to use finite differences.

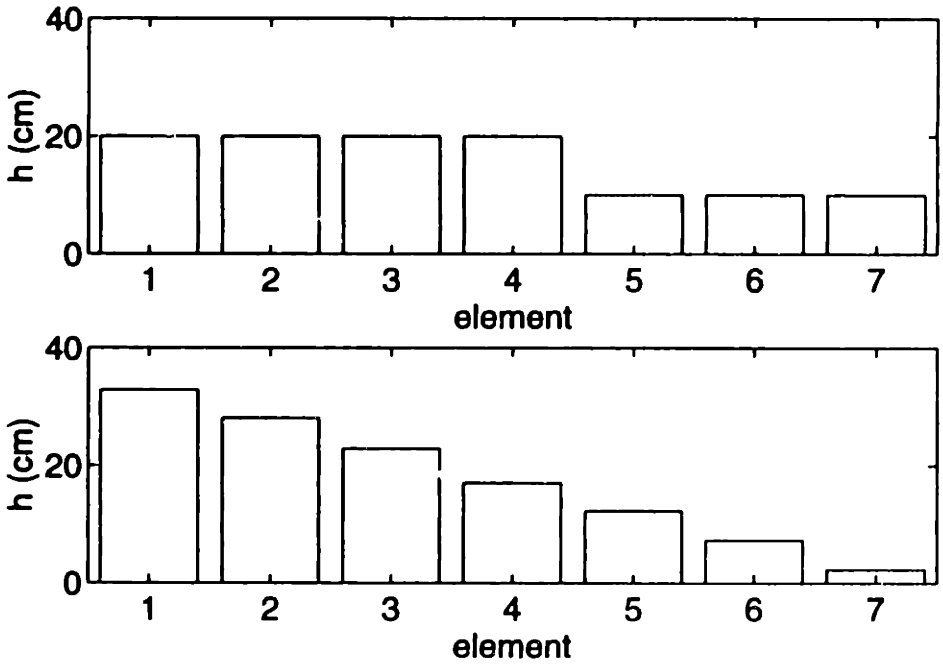

Figure 6.9 Nominal and redesigned height vectors.

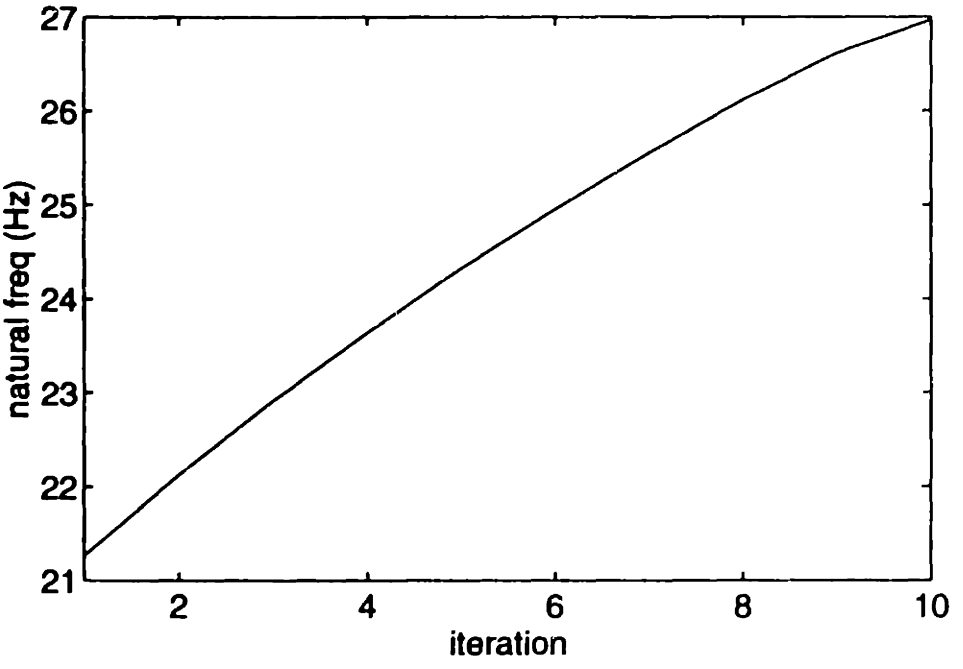

Figure 6.10 Improvement of ω_1 during iteration.

CHAPTER 7
Orthogonal Bases for Eigenvalue Sensitivies

7.1 Introduction

In this chapter, we investigate the possibility of finding a set of shape changes such that each member of the set modifies only a particular natural frequency of the structure. Such a set of shape changes can be treated as a basis for the design space. Such basis functions, if they exist, form an orthogonal set in the design space, and decompose it into subspaces corresponding to individual natural frequencies.

The analysis of the sensitivity of system response to parameter variations finds wide application in design optimization (Haftka et al., 1990) as well as in the analysis of systems with parameter uncertainties (Ibrahim, 1987). In the field of structural optimization, the sensitivities of objective functions to changes in design parameters play an integral role in iterative schemes as well as in the application of optimality criteria. In manual design, sensitivities can guide the designer in making decisions.

In the design of structures, buckling and vibration are often important considerations, and the eigenvalues generally appear in the constraints, the objectives, or both. In such cases, the sensitivities of the eigenvalues to design changes play a central role in the design process. Various approaches including perturbation methods (Courant and Hilbert, 1953) and differentiation schemes (e.g., Haug et al., 1986) have been used to compute the sensitivities of eigenvalues to changes in design for both lumped- and distributed-parameter

models, and a reasonably complete theory has been developed (see Chapter 6). Although a great deal of research has been devoted to the development and application of expressions for the eigenvalue sensitivities, very little discussion of the properties of these sensitivities has appeared in the literature.

In this chapter, we examine the sensitivity of the natural frequencies of of an initially uniform beam to nonuniform changes in its cross-sectional dimensions. We use perturbation results to obtain an expression for the change of an eigenvalue when a nonuniform small change is made to the shape of the bar. For some specific examples, we show that the eigenvalues can be changed independently, and that a simple relation exists between the corresponding eigenfunction and shape change. Next, we attempt to generalize these findings to torsional vibration problems with general boundary conditions and determine the conditions under which such a set of orthogonal shape changes exist.

7.2 Eigenvalue Perturbation

Perturbation methods for eigenvalue problems produce asymptotic approximations to the eigensolutions of a perturbed problem in terms of the eigensolution to the unperturbed problem. The first terms in these expansions are, in effect, the sensitivity of the eigensolution to the perturbation. A great number of researchers have treated this problem over the years. Rellich (1969) presents a detailed exposition of the theory of eigenvalue perturbation. Pierre (1987) treats the case where the boundary conditions are perturbed.

Here, we summarize the well known results for the case where the boundary conditions are not perturbed. Consider the unperturbed eigenvalue problem

$$L_0\phi(x) + \lambda\phi(x) = 0 \qquad x \in [0,1] \tag{7.1}$$

$$B_k\phi(x) = 0 \qquad x = 0,1 \tag{7.2}$$

where L_0 and B_k, are linear, homogeneous, self-adjoint operators and the B_k do not depend explicitly on the eigenvalues. We assume that this problem has distinct eigenvalues λ_n and eigenfunctions $\phi_n(x)$ orthonormalized so that

$$\int_0^1 \phi_n^2 \, dx = 1 \qquad \int_0^1 \phi_n\phi_m \, dx = 0 \tag{7.3}$$

for $n \neq m$.

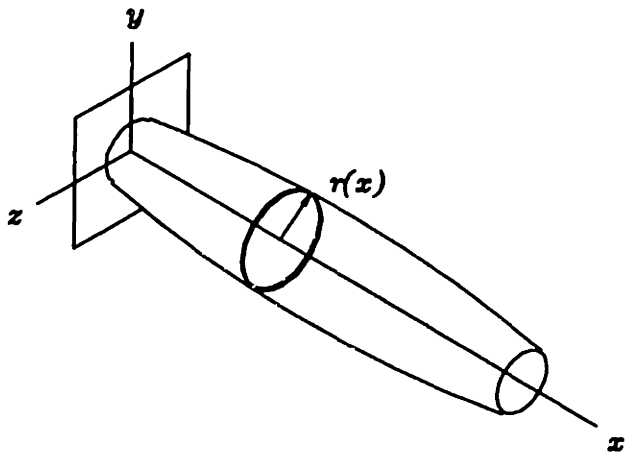

Figure 7.1 shaft with varying cross-sectional radius

Now, consider a small change ϵL_1 to the operator L_0 so that Eq. (7.1) becomes

$$(L_0 + \epsilon L_1)\phi(x) + \lambda\phi(x) = 0 \tag{7.4}$$

where ϵ is a small dimensionless parameter. To first order, the change in the nth natural frequency is

$$\delta\lambda_n = -\epsilon \int_0^1 \phi_n L_1 \phi_n \, dx \tag{7.5}$$

and the change in the nth eigenfunction is

$$\delta\phi_n = \epsilon \sum_{m \neq n} \frac{\int_0^1 \phi_m L_1 \phi_n \, dx}{\lambda_m - \lambda_n} \phi_m \tag{7.6}$$

7.3 Examples

7.3.1 Torsional Vibration of a Shaft With Fixed Ends

We consider a shaft with circular cross section and nonuniform radius as shown in Fig. 7.1. Torsional vibration of a shaft with fixed ends is governed by an equation of the form

$$[GJ(x)\theta'(x,t)]' = I(x)\ddot{\theta}(x,t) \tag{7.7}$$

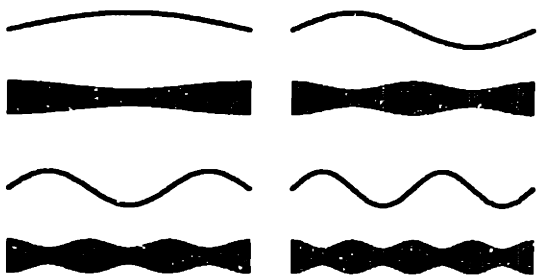

Figure 7.2 mode shapes and corresponding shape changes for a shaft with fixed ends

with boundary conditions

$$\theta(0,t) = \theta(1,t) = 0 \tag{7.8}$$

where $(\cdot)' = \partial(\cdot)/\partial x$ and G is the shear modulus. For a shaft with solid circular cross section, $J(x) = \pi r^4(x)/2$ and $I(x) = \rho\pi r^4(x)/2$ where ρ is the density of the material. We now consider perturbations to an initially uniform shaft so that $r(x) = r_0 + \epsilon r_1(x)$. In terms of the notation used in the previous section, we have

$$L_0 = \frac{\partial^2}{\partial x^2} \qquad L_1 = \frac{4}{r_0}\frac{\partial r_1}{\partial x}\frac{\partial}{\partial x} \tag{7.9}$$

and $\lambda = \omega^2\rho/G$ where ω is the natural frequency.

The eigensolution of the unperturbed ($\epsilon = 0$) problem is

$$\lambda_n = (n\pi)^2 \qquad \phi_n(x) = \sqrt{2}\sin n\pi x \tag{7.10}$$

According to Eq. (7.5), a small change $\epsilon r_1(x)$ perturbs the nth eigenvalue by

$$\delta\lambda_n = -\frac{4\epsilon}{r_0}\int_0^1 \phi_n r_1' \phi_n'\, dx = -\frac{4\epsilon n\pi}{r_0}\int_0^1 r_1' \sin 2n\pi x\, dx \tag{7.11}$$

from which it is clear that (to first order) choosing $r_1(x) = a\cos 2i\pi x$ (as illustrated in Fig. 7.2) will result in a change in only the ith eigenvalue:

$$\delta\lambda_i = \frac{4a\epsilon(i\pi)^2}{r_0} \qquad \delta\lambda_j = 0 \tag{7.12}$$

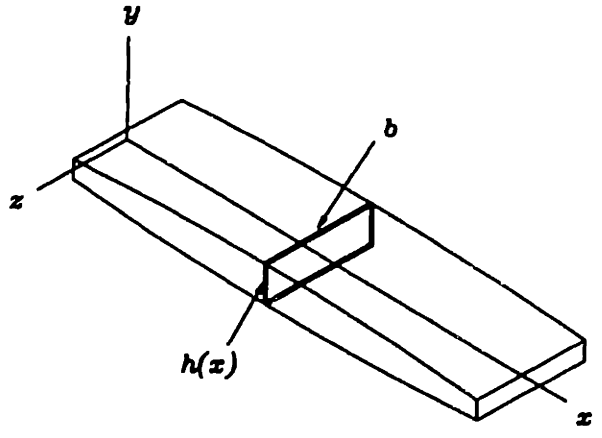

Figure 7.3 beam with varying thickness

Thus, corresponding to each eigenvalue, there is a shape change $r_1(x)$ that will result in a change to only that eigenvalue. These shape changes are mutually orthogonal, so that the eigenvalues can be changed independently. We also note that the shape change for the ith mode can be obtained from the ith mode shape according to the simple formula $r_1'(x) = -a(\phi_i^2(x))'/2i\pi$.

7.3.2 Flexural Vibration of a Beam on Simple Supports

The free vibration of an Euler-Bernoulli beam is governed by

$$\rho A(x)\ddot{w} + (EI(x)w'')'' = 0 \tag{7.13}$$

where, for vibration in the $y-$direction of the nonuniform beam shown in Fig. 7.3, the cross-sectional area and moment of inertia are given by $A(x) = bh(x)$ and $I(x) = \frac{1}{12}bh^3(x)$, respectively. For a simply supported beam, we have the boundary conditions

$$w(0) = w(1) = w''(0) = w''(1) = 0 \tag{7.14}$$

We consider perturbations to an initially uniform beam so that $h(x) = h_0 + \epsilon h_1(x)$ and in the notation of Section 7.2 we have

$$L_0 = \frac{\partial^4}{\partial x^4} \quad \text{and} \quad L_1 = \frac{1}{h_0}\left(3h_1''\frac{\partial^2}{\partial x^2} + 6h_1'\frac{\partial^3}{\partial x^3} + 2h_1\frac{\partial^4}{\partial x^4}\right) \tag{7.15}$$

and $\lambda = \omega^2 \rho A/EI$ where ω is the natural frequency.

The eigensolution for the unperturbed (uniform) beam is given by

$$\lambda_i = (i\pi)^4 \qquad \phi_i(x) = \sqrt{2}\sin i\pi x \tag{7.16}$$

Substituting this expression along with Eq. (7.15) into the expression for the eigenvalue sensitivity, Eq. (7.5), we obtain

$$\begin{aligned} \delta\lambda_n &= -\frac{\epsilon}{h_0}\int_0^1 \phi_n(3h_1''\phi_n'' + 6h_1'\phi_n''' + 2h_0h_1\phi_n^{\text{iv}})dx \qquad (7.17)\\ &= -\frac{2\epsilon}{h_0}\int_0^1 \left\{[2h_1(i\pi)^4 - 3h_1''(n\pi)^2]\sin^2 n\pi x - 3h_1'(n\pi)^3 \sin 2n\pi x\right\} dx \end{aligned}$$

So, to change only ω_i, choose $h_1(x) = a\cos 2i\pi x$. Then

$$\delta\lambda_i = -\frac{6a\epsilon(i\pi)^4}{h_0} \qquad \delta\lambda_j = 0 \tag{7.18}$$

Thus, we find again a set of simple shape changes $h_1(x)$ that changes a particular eigenvalue without changing any others. In the next section, we attempt to carry out the same procedure for torsional vibration with general boundary conditions.

7.4 Torsional Vibration with General Boundary Conditions

We now consider torsional vibration of an initially uniform shaft governed by Eq. (7.7) and the general boundary conditions Eq. (7.2). We assume that the unperturbed problem $L_0\phi + \lambda\phi = 0$ has been solved and that the eigenfunctions ϕ_n have been normalized according to Eq. (7.3).

7.4.1 Properties of the Sensitivity

To first order, the change in the nth eigenvalue is

$$\delta\lambda_n = -\frac{4\epsilon}{r_0}\int_0^1 r_1'\phi_n'\phi_n\, dx = -\frac{2\epsilon}{r_0}\int_0^1 r_1'(\phi_n^2)'\, dx = -\frac{2\epsilon}{r_0}\int_0^1 r_1' g_n\, dx \tag{7.19}$$

from which we see that the nth eigenvalue is perturbed in proportion to the projection of the derivative of the shape change onto the derivative of the

square of the nth mode shape. We denote the latter quantity $g_n(x)$ and refer to it as the sensitivity distribution. If we wish to change only the ith eigenvalue, we must find a shape change $r_1(x)$ whose slope projects onto $g_i(x)$ but is orthogonal to all $g_j(x)$ for $j \neq i$. Guided by the results from the fixed–fixed shaft, we choose

$$r_1'(x) = -ag_i(x) = -a\left(\phi_i^2(x)\right)' \tag{7.20}$$

where a is a constant and evaluate the changes in the eigenvalues. If this shape change, which is proportional to $g_i(x)$, has a nonzero projection onto $g_j(x)$, then we can construct an orthogonal set from a linear combination of such functions as discussed in Section 7.4.3.

Substituting Eq. (7.20) into Eq. (7.19) we find that the changes in the eigenvalues are given by

$$\delta\lambda_i = \frac{8\epsilon a}{r_0}\int_0^1 \phi_i^2\phi_i'^2\,dx \tag{7.21}$$

and

$$\delta\lambda_j = \frac{8\epsilon a}{r_0}\int_0^1 \phi_i\phi_j\phi_i'\phi_j'\,dx \tag{7.22}$$

for $j \neq i$. In the following, we evaluate these expressions for the eigenvalue perturbations.

Evaluation of $\delta\lambda_i$

Noting that ϕ_i must satisfy $L_0\phi_i = \phi_i'' = -\lambda_i\phi$, we write

$$-\lambda_i\int_0^1 \phi_i^4\,dx = \int_0^1 \phi_i^3\phi_i''\,dx \tag{7.23}$$

and integrate by parts to obtain

$$-\lambda_i\int_0^1 \phi_i^4\,dx = \left[\phi_i^3\phi_i'\right]_0^1 - 3\int_0^1 \phi_i^2\phi_i'^2\,dx \tag{7.24}$$

Next, we observe that an integral of $\phi_i'' + \lambda_i\phi_i = 0$ is given by

$$\phi_i'^2 + \lambda_i\phi_i^2 = 2E_i \tag{7.25}$$

where E_i is a constant. Taking the inner product with ϕ_i^2, we obtain

$$\int_0^1 \phi_i^2\phi_i'^2\,dx + \lambda_i\int_0^1 \phi_i^4\,dx = 2E_i \tag{7.26}$$

which combines with Eq. (7.24) to give

$$4\int_0^1 \phi_i^2\phi_i'^2\,dx = 2E_i + \left[\phi_i^3\phi_i'\right]_0^1 \tag{7.27}$$

Next, to evaluate E_i, we introduce the identity

$$(\phi_i\phi_i')' = \phi_i'^2 + \phi_i\phi_i'' = \phi_i'^2 - \lambda_i\phi_i^2 \tag{7.28}$$

which, along with Eq. (7.25), yields

$$2E_i = [\phi_i\phi_i']_0^1 + 2\lambda_i \tag{7.29}$$

Combining this equation with Eq. (7.27) and substituting into the expression for $\delta\lambda_i$ given in Eq. (7.21), we obtain

$$\delta\lambda_i = \frac{2\epsilon a}{r_0}\left\{2\lambda_i + \left[(1+\phi_i^2)\phi_i\phi_i'\right]_0^1\right\} \tag{7.30}$$

which gives the change in the ith eigenvalue in terms of the value and slope of its eigenfunction evaluated at the boundaries.

Evaluation of $\delta\lambda_j$

Noting again that the ith mode must satisfy $\phi_i'' + \lambda_i\phi_i = 0$, and taking the inner product with $\phi_j\phi_i'\phi_j'$, we obtain

$$\lambda_i\int_0^1 \phi_i\phi_j\phi_i'\phi_j'\,dx = -\int_0^1 \phi_i'\phi_i''\phi_j\phi_j'\,dx \tag{7.31}$$

Next, we interchange i and j and subtract to get

$$\begin{aligned}(\lambda_j - \lambda_i)\int_0^1 \phi_i\phi_i'\phi_j\phi_j'\,dx &= \int_0^1 \phi_i'\phi_j'(\phi_j\phi_i'' - \phi_i\phi_j'')dx \\ &= \int_0^1 \phi_i'\phi_j'(\phi_j\phi_i' - \phi_i\phi_j')'dx\end{aligned} \tag{7.32}$$

Integrating by parts, we have

$$\begin{aligned}&2(\lambda_j - \lambda_i)\int_0^1 \phi_i\phi_i'\phi_j\phi_j'\,dx = \\ &\int_0^1 (\lambda_j\phi_j^2\phi_i'^2 - \lambda_i\phi_i^2\phi_j'^2)\,dx + \left[\phi_i'\phi_j'\left(\phi_j\phi_i' - \phi_i\phi_j'\right)\right]_0^1\end{aligned} \tag{7.33}$$

But the second term on the right-hand side must vanish for a self-adjoint system with separable boundary conditions. The inner product of $\lambda_j \phi_j^2$ with the expression for E_i given by Eq. (7.25) is

$$\lambda_j \int_0^1 \phi_j^2 \phi_i'^2 \, dx + \lambda_i \lambda_j \int_0^1 \phi_i^2 \phi_j^2 \, dx = 2\lambda_j E_i \tag{7.34}$$

Interchanging i and j and subtracting, we have

$$\int_0^1 (\lambda_j \phi_j^2 \phi_i'^2 - \lambda_i \phi_i^2 \phi_j'^2) \, dx = 2\lambda_j E_i - 2\lambda_i E_j \tag{7.35}$$

This equation in conjunction with Eqs. (7.33), (7.29), and (7.22) gives

$$\delta\lambda_j = \frac{4\epsilon a}{r_0} \left\{ \lambda_j [\phi_i \phi_i']_0^1 - \lambda_i [\phi_j \phi_j']_0^1 \right\} \tag{7.36}$$

which gives the change in the jth eigenvalue in terms of the value and slope of the ith and jth eigenfunctions evaluated at the boundaries.

7.4.2 Discussion

Equations (7.30) and (7.36) give the changes in the eigenvalues when the shape change is chosen to project onto the ith sensitivity distribution. Examining Eq. (7.36), we see that the terms on the right-hand side do not vanish in general. Also, we see that these terms take on a different value for each value of the index j. We conclude that the sensitivity distributions are in general not orthogonal, and therefore that shape changes chosen proportional to the sensitivity distributions will not form an orthogonal set. It is clear, however, that for the particular cases of free-free, fixed-free, and fixed-fixed shafts, the sensitivity distributions are orthogonal.

7.4.3 Orthogonalization

We have shown that it in general shape changes chosen proportional to the sensitivity function will not result in an orthogonal set. In this section, we construct an orthogonal set of shape changes from a linear combination of sensitivity distributions. Consider a shape change with slope $h(x)$ composed of a linear combination of sensitivity distributions:

$$r_1'(x) = h(x) = -\sum_{i=1}^{N} a_i g_i(x) \tag{7.37}$$

where the distributions $g_i(x)$ are given by

$$g_i(x) = (\phi_i^2(x))' \tag{7.38}$$

and the constants a_i are to be determined. Then, using Eq. (7.19) we can write the change in the first N eigenvalues in the form

$$\begin{pmatrix} \delta\lambda_1 \\ \vdots \\ \delta\lambda_N \end{pmatrix} = -\frac{2\epsilon}{r_0} \begin{bmatrix} \langle g_1, g_1 \rangle & \cdots & \langle g_1, g_N \rangle \\ \vdots & & \vdots \\ \langle g_1, g_N \rangle & \cdots & \langle g_N, g_N \rangle \end{bmatrix} \begin{pmatrix} a_1 \\ \vdots \\ a_N \end{pmatrix} \tag{7.39}$$

where $\langle p(x), q(x) \rangle$ denotes the inner product $\int_0^1 p(x)q(x)\,dx$. We have seen in the last section that the functions $g_i(x)$ and $g_j(x)$ are not generally orthogonal and that therefore the matrix above will not be diagonal. But if it is of full rank, then we can always choose constants a_i to yield a desired vector $\delta\lambda_i$.

Consider a shaft clamped rigidly at one end and supported by a torsional spring at the other, so that the boundary conditions are given by

$$\phi(0) = 0 \text{ and } \phi(1) = -k_t\phi'(1) \tag{7.40}$$

We solve for the first twenty eigenvectors and eigenfunctions, and then use Eqs. (7.30) and (7.36) to evaluate the coefficients $\langle g_i, g_j \rangle$ in Eq. (7.39). Next, we solve for the values of the a_i that modify only the eigenvalue of interest and construct the corresponding shape change $h(x)$.

The result is shown Fig. 7.4.3 for the first mode. The plotted function $h(x)$ represents the slope of the shape change that modifies the first eigenvalue while holding the second through the twentieth eigenvalues constant. Similar plots are shown in Figs. 7.4.3 and 7.4.3 for modification of the second and third eigenvalues. Such a calculation could in principle be carried out for any number of modes, and an analytical solution could possibly be obtained for an infinite number of modes. But in practice, we are seldom concerned with more than the first few modes of a structure, and the series solutions for $h(x)$ are sufficient.

7.5 Discussion

In this chapter, we studied the sensitivity of the eigenvalues of torsional vibration of a uniform shaft to small nonuniform changes in its radius. In particular,

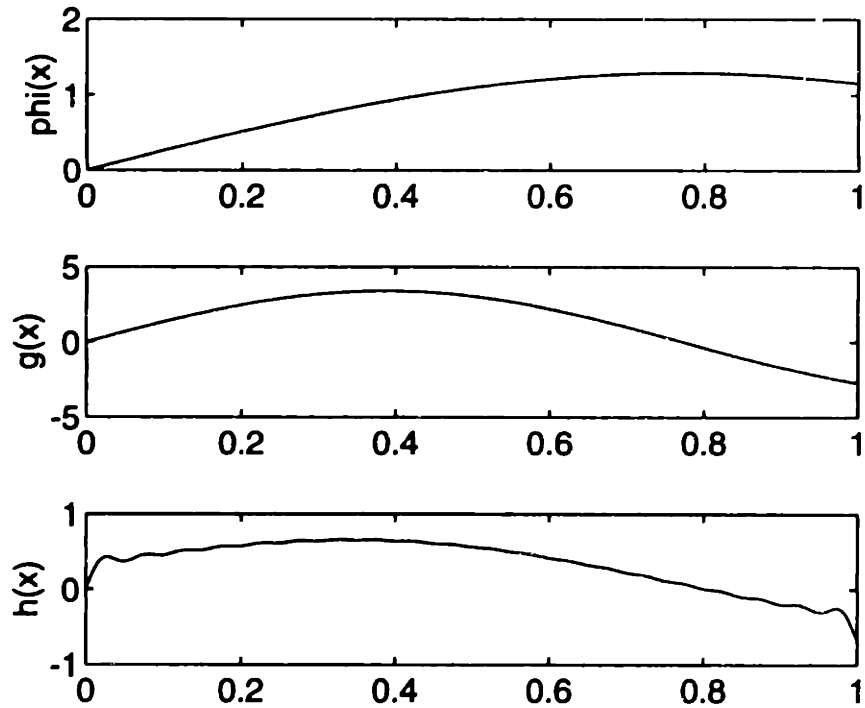

Figure 7.4 mode shape $\phi(x)$, sensitivity distribution $g(x)$, and shape change $h(x)$ for the first mode of a shaft with a compliantly restrained end

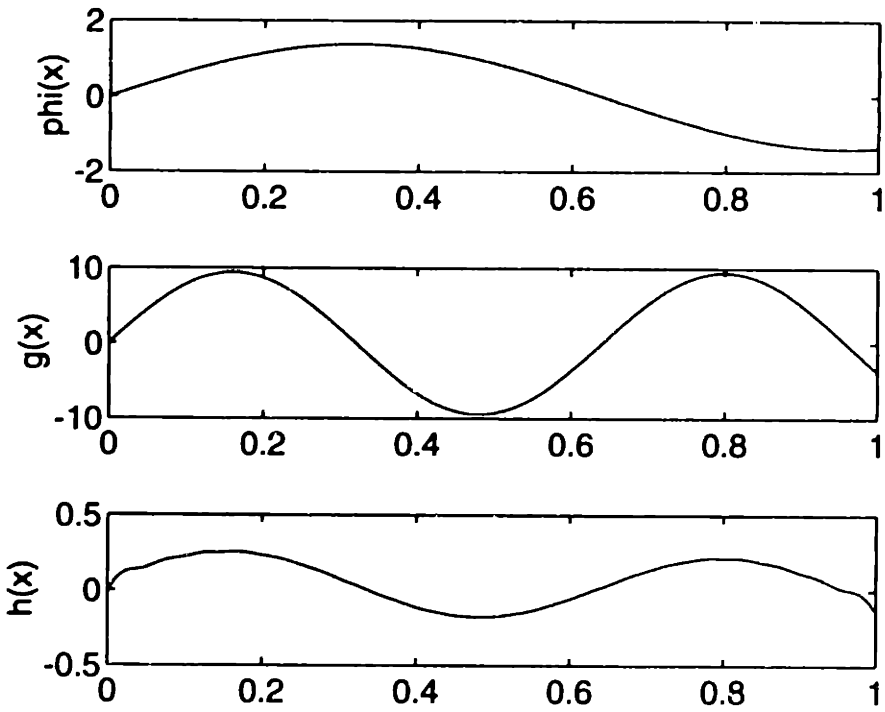

Figure 7.5 mode shape $\phi(x)$, sensitivity distribution $g(x)$, and shape change $h(x)$ for the second mode of a shaft with a compliantly restrained end

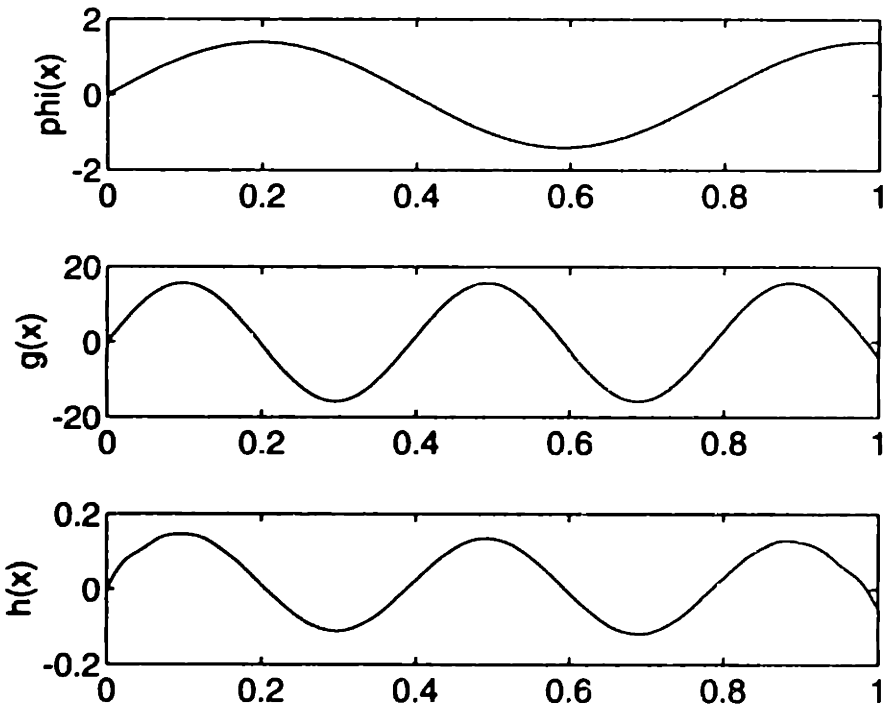

Figure 7.6 mode shape $\phi(x)$, sensitivity distribution $g(x)$, and shape change $h(x)$ for the third mode of a shaft with a compliantly restrained end

we investigated the possibility of finding changes in the radius that modify only one eigenvalue. We showed that this is possible as long as the matrix whose elements are formed from the inner product $\langle(\phi_i^2)', (\phi_j^2)'\rangle$, where the ϕ_i are the eigenfunctions of the uniform shaft, is of full rank.

Such findings may be useful in structural optimization problems where the eigenvalues appear in the constraints or objectives. Olhoff (1989) observed that when a constant volume beam is designed to maximize a particular eigenvalue of transverse vibration, all other eigenvalues are affected. Moreover, he found that if the objective eigenvalue is not the first eigenvalue then all lower-order eigenvalues decrease as the objective eigenvalue increases. Results of the type developed in this paper may be of some use in the development of efficient techniques for handling problems involving several eigenvalues.

The results presented here are restricted to initially uniform shafts whose boundary conditions do not depend explicitly on the eigenvalues. We hope to extend this work to deal with these cases in the near future.

CHAPTER 8

Design Example

8.1 Introduction

In this chapter, we consider design of the wafer-handling robot sketched in Fig. 1.3. The robot is designed to carry a 20 kg carriage over a 2.0 by 1.4 m workspace in the xz plane, and packaging constraints require that the base and column cross sections be no larger than 356 mm and 260 mm squares respectively. We choose to construct the base of steel and the column of aluminum with the cross sections shown in Fig. 8.1.

We are concerned with the first resonant frequency in each of the x and y directions. In the x direction, the lowest resonance corresponds to the "pitch" mode shown Fig. 1.4(b). This mode of vibration involves flexure of the column, transverse deformation of the linear bearings, longitudinal deformation of the leadscrew, and some bending of the base. The associated resonant frequency takes on its lowest value f_x when the column is positioned at the end of its travel furthest from the drive motor.

In the y direction, the resonant frequency associated with the "roll" mode shown in Fig. 1.4(b) reaches its minimum value f_y when the column is at the midpoint of its travel. This mode involves flexure of the column, transverse deformation of the linear bearings, and torsion and flexure of the base. In this chapter, we wish to maximize the "worst case" frequencies f_x and f_y and the associated loss factors.

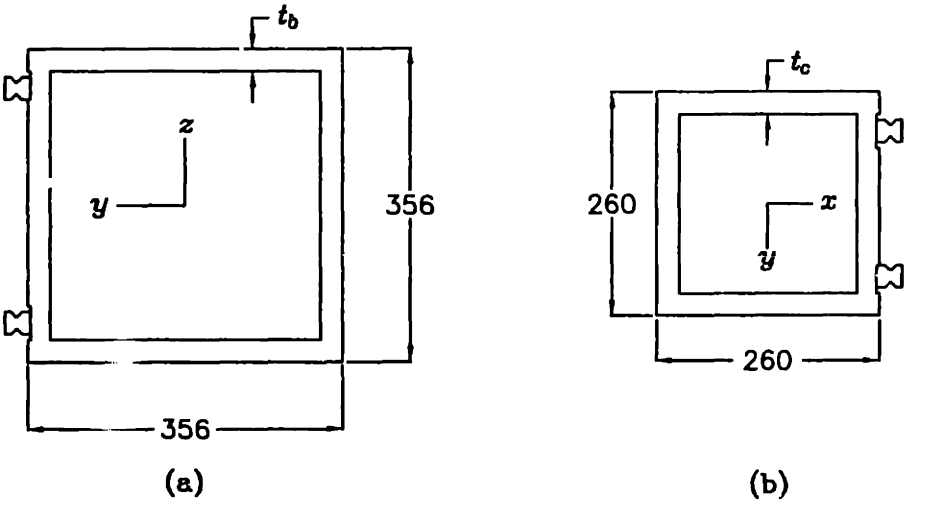

Figure 8.1 Cross section of the base (a) and column (b) of the machine of Fig. 1.3: A pair of size 25 linear guides is mounted to each of these members.

8.2 Design for Maximum Resonant Frequency

The overall dimensions of the machine are fixed by packaging constraints and there is little space to accommodate larger than size 25 linear guides. The rails can be set $d_r = 275$ mm apart, and each linear bearing has stiffness $k_b = 300$ N/μm. The parameters that we can adjust to maximize the resonant frequencies of the machine are the radius r_s of the ballscrew and the wall thicknesses t_b and t_c of the base and column.

Nominal Design

If the only compliance in the machine is that of the linear bearings, the stiffness at the endpoint is $k_b d_r^2/\ell_c^2$. The column is the major contributor to the effective mass of the principal modes so we set the wall thickness so that its bending deflection under an endpoint load matches that due to the linear bearings. That is,

$$\frac{3E_cI_c}{\ell_c^3} = \frac{k_b d_r^2}{\ell_c^2} \tag{8.1}$$

Table 8.1 Lowest resonant frequencies in the x and y directions for various (undamped) designs: r_s is radius of the leadscrew, t_b is the wall thickness of the base, and t_c is the wall thickness of the column.

	t_b (mm)	t_c (mm)	r_s (mm)	f_y (Hz)	f_x (Hz)
nominal	18.9	14.5	11.8	61.7	61.3
redesigned	25.9	12.1	13.7	63.0	63.0
inch plate	25.4	12.5	13.3	62.9	62.8
tube base	12.5	12.5	13.3	60.2	61.2

Because the base is stationary and mounted on rigid supports, there is little cost in choosing a large wall thickness; therefore, we set its torsional stiffness equal to four times that of the linear bearings:

$$\frac{4w_b h_b G_b t_b}{(w_b + w_h)\ell_1} = k_b d_r^2 \tag{8.2}$$

We set the leadscrew radius so that the frequency of the "dumbbell" mode involving the column and drive motor is roughly equal to that of the roll mode. If the effective motor inertia matches that of the payload, the frequencies match (very roughly) when

$$\frac{E_s \pi r_s^2}{\ell_b^2} = 2\frac{k_b d_r^2}{\ell_c^2} \tag{8.3}$$

These equations yield the nominal values of t_b, t_c and r_s given in the first row of Table 8.1.

Optimization

Starting with the nominal design, we use the approach of Section 6.4.2 to adjust the wall thicknesses t_b and t_c and the screw radius r_s to raise the lowest natural frequency of the structure. In ten iterations, this process converges to the design listed in the second row of Table 8.1. The redesign process raises the lowest resonant frequency by less than two per cent, so evidently the nominal design is quite good. Because the dimensions of the "redesigned" machine given in the Table 8.1 do not correspond to readily available stock

in the United States, we would actually build to the dimensions of the "inch plate" design listed in the third row of Table 8.1. If we wish to lower the cost of fabrication (and the weight of the machine), we could use a standard $14 \times 14 \times 0.5$ inch steel tube as listed under "tube base" for the base without lowering the resonant frequencies by more than five per cent.

8.3 Damping Augmentation

In this section, we begin with the "tube base" design listed in Table 8.1 and design dampers in turn for the linear bearings, base, leadscrew, and column. We design each of these elements to have a loss factor of at least seven per cent and then use the finite-element model to compute the damping in the machine with the various dampers applied separately and in combination.

Linear Bearings

As discussed in Section 2.2, we add an extra linear bearing on each rail and couple the additional bearings to the linear guides by means of a viscoelastic layer. If the only compliant elements in the machine are the linear bearings and the loss factor of the viscoelastic material is unity, then we can obtain the maximum loss factor of 0.084 by sizing the viscoelastic layer to have 0.58 of the stiffness of a linear bearing. Following this guideline, we set the coupling parameter g_b initially to 0.58.

Addition of this damper to the machine produces the resonant frequencies and loss factors listed in Column B of Table 8.2. The resonant frequency of the roll mode increases from 60.2 to 62.5 Hz and the associated loss factor is 2.9 per cent. Because the additional linear bearings are installed midway between the original linear bearings that support the column, such a damper has no appreciable effect on the pitch mode.

Base

We are concerned primarily with torsion of the base, so we attach identical constrained viscoelastic layers to each face as shown in Fig. 8.2. If the constraining layers are steel with thickness 12.5 mm, we find from Eq. (4.52) that $Y = 0.5$. From Fig. 4.7, we see that the loss factor of the tube in torsion

Table 8.2 Resonant frequencies (Hz) and loss factors (per cent) of the wafer handling robot with various dampers installed: A dash in place of a parameter value indicates that the associated damper is not present in the listed design.

		A	B	C	D	E	F
bearings	g_b	-	0.58	-	-	-	0.58
base	g_t	-	-	2.00	-	-	2.00
screw	Y	-	-	-	0.07	-	0.07
column	g_c	-	-	-	-	10.0	10.0
pitch	f_x	61.2	61.2	63.7	61.5	63.5	66.8
	η_x	0.0	0.0	2.1	1.4	2.3	8.9
roll	f_y	60.2	62.5	62.4	60.2	61.8	66.9
	η_y	0.0	2.9	4.0	0.0	2.7	7.1

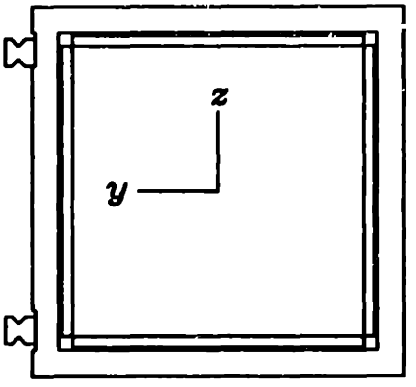

Figure 8.2 Cross section of the base with constrained viscoelastic layers mounted to its interior.

reaches a peak of about 10 per cent for $\mathrm{Re}(g_t) \approx 2.0$ if the viscoelastic material loss factor is unity.

Of secondary concern is flexure of the base. For the configuration in Fig. 8.2, the stiffness parameter Y for constrained-layer damping defined in Eq. (2 49) is 0.58. Treating the base as simply supported, we determine the coupling parameter g from Eq. (2.50) with the beam length L replaced by the effective length L/π. Combining this expression with the the definition of the torsional coupling parameter g_t given in Eq. (4.51), we find that $\mathrm{Re}(g) = 2.3$ when $\mathrm{Re}(g_t) = 2.0$. Referring to Fig. 2.2, we see that for this value of g the loss factor of the base in bending is approximately 0.035 and that the stiffness approaches that of the rigidly coupled beam.

Adding such a damper to the machine yields the resonant frequencies and loss factors shown in Column C of Table 8.2. The resonant frequency of the roll mode is in this case raised to 62.4 Hz, and the associated loss factor is 4.0 per cent. Because the constrained viscoelastic layers stiffen and damp flexural motion of the base, they produce a loss factor of 2.1 per cent for the pitch mode.

Leadscrew

The axial stiffness of the leadscrew is approximately 58 N/μm. For a leadscrew of this diameter, we can readily specify a ballnut and rotary bearings with stiffness on the order of 1000 N/μm and hence can safely ignore their compliance during our initial calculations. The lead per revolution is 6 mm, so for a screw of radius 13.3 mm, torsional wind up of the screw decreases the effective axial stiffness by less than one part in thirty and can be neglected.

Let us design for an average temperature rise of 15°C in the screw. For a viscoelastic material with a loss factor of one, we see from Eq. (5.5) that to obtain a loss factor of 0.07 when the carriage is at the far end of its travel, we must have $Y = 0.075$ and a preload force of 1500 N. If the ballscrew is supported 0.22 m from the neutral axis of the base, we expect the preload to cause a deflection on the order of 10 μm in the base.

The base itself weighs approximately 2.8 kN (620 lb) without constrained layer dampers. It therefore deflects under its own weight by an amount comparable to that caused by the preload. If such deflections are unacceptable, then one possibility is to mount the leadscrew below the base so that the preload force and the gravity sag partially cancel. Of course, the preload force will

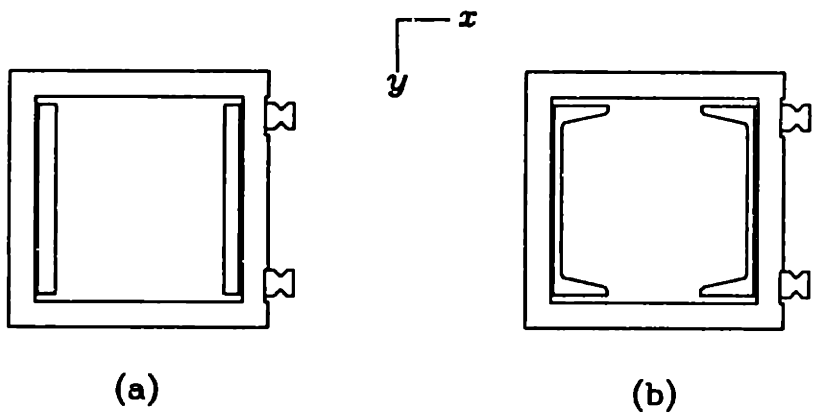

Figure 8.3 Cross section of the column with constrained viscoelastic layers:

drop as the leadscrew temperature rises and some of the cancellation will be lost.

Addition of a damped leadscrew support with $Y = 0.075$ to the undamped machine produces the resonant frequencies and loss factors shown in Column D of Table 8.2. The leadscrew damper has no effect on the roll mode, but it produces a loss factor of 1.4 per cent in the pitch mode.

Column

In order to minimize the mass added to the column, we add constrained viscoelastic layers along only the quarter of its length closest to the base. To further reduce the weight of the column, we laminate constrained viscoelastic layers only to the portions of the wall facing in the x direction and rely on damping due to relative vibration in the plane of lamination to damp vibration in the y direction. For the purposes of the nominal design, we model the column as a cantilever beam.

A first attempt at such a design is sketched in Fig. 8.3(a), where the constraining layers are aluminum plate with thickness of 12.5 mm. In Fig. 8.4, the loss factor of the first mode in each of the x and y directions is plotted as a function of the real part of the shear parameter g_c associated with constrained layer damping of the column as defined in Eq. (2.50). We see that while loss factors as high as 0.05 can be obtained in the x direction, the highest loss

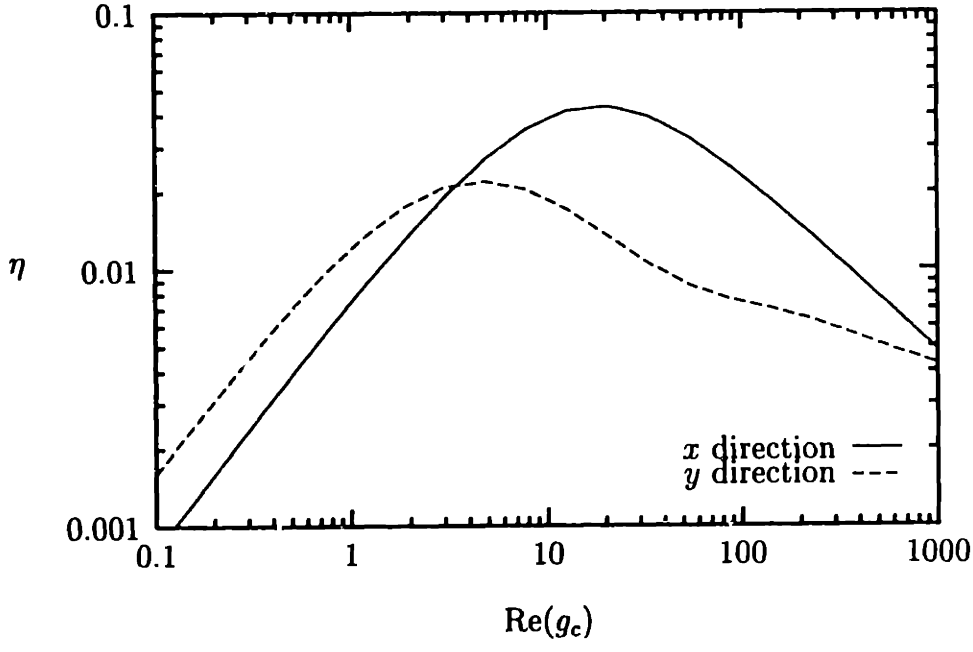

Figure 8.4 Loss factor of the first mode in the x and y directions of the partially covered cantilever with cross section shown in Fig. 8.3(a) as a function of the real part of the coupling parameter g_c.

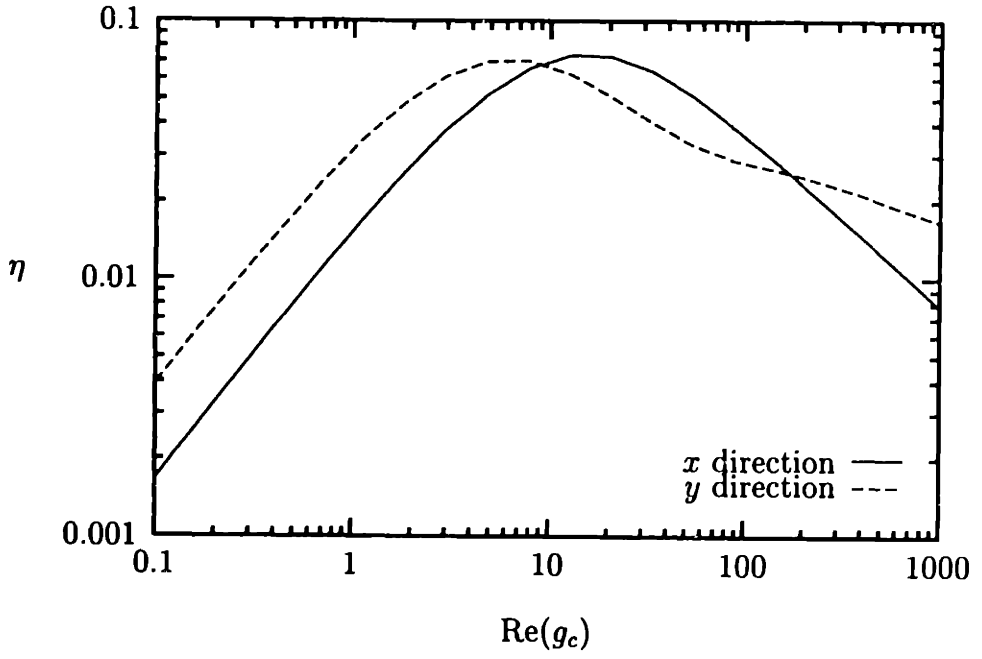

Figure 8.5 Loss factor of the first mode in the x and y directions of the partially covered cantilever with cross section shown in Fig. 8.3(b) as a function of the real part of the coupling parameter g_c.

factor in the y direction is 0.02. Moreover, these maximum loss factors occur at different values of g_c, so we can't simultaneously damp vibration in both directions. This damper performs so poorly because the constraining layers stiffen the beam only slightly in the y direction.

Let us consider as an alternative the use of standard steel channels (C9 $\times$ 13.4) for the constraining layers as shown in Fig. 8.3(b). We obtain in this case the the damping behavior shown in Fig. 8.5 with loss factors in both directions of about 0.07 for $\mathrm{Re}(g_c) = 10$. Addition of constrained viscoelastic layers of the type shown in Fig. 8.3(b) with $g_c = 10$ to the undamped machine produces loss factors of 2.3 and 2.7 per cent, respectively, in the pitch and roll modes as tabulated in Column E of Table 8.2.

Combined Damping

So far we have computed the loss factors and resonant frequencies for each of the dampers alone. If we run the finite-element calculation for a machine with all of these dampers installed, we obtain the results given in Column F of Table 8.2.

8.4 Discussion

In this chapter, we have seen how many of the results obtained in Chapters 2–6 can be used to quickly design a damping treatment for a built-up machine structure. For the wafer-handling robot discussed here, we obtained loss factors of better than seven per cent for the principal modes while raising their resonant frequencies by nearly ten per cent while increasing the mass of the column (without the carriage) by roughly 17 per cent.

CHAPTER 9
Conclusion

9.1 Findings

We set out in this work to develop tools for damping vibration in machines such as the one sketched in Fig. 1.3. In so doing, we have discovered some new methods for damping vibration and developed improved models for others as listed in the "Summary of Contributions" given in Section 1.3. We have also touched on the topic of design sensitivities as a tool for manipulating the eigenvalues of a structure during iterative design.

Though we have sought throughout this work to develop the simplest mathematical models capable of describing the phenomena of interest, we have often found it necessary to solve an eigenvalue problem in the form of a set of coupled ordinary-differential equations with boundary and matching conditions. Whenever possible, we have provided closed-form solutions for important results. In cases where we have had to resort to numerical methods, we have given results in terms of the minimum number of non-dimensional parameters.

We have also seen that almost any damper that we can implement in hardware can be modeled (at least approximately) as the parallel-stack damper shown in Fig. 2.1(c). If we are able to set forth approximations for the effective spring constants in this model, we can readily size components to maximize the loss factor of a given damper. The maximum loss factor attainable using a parallel-stack damper is a function of the fractional stiffening of a structure as the viscoelastic material is varied from perfectly compliant to perfectly rigid.

The fractional stiffening is characterized by the stiffness ratio Y, which is defined as

$$Y = \frac{k_\infty - k_0}{k_0} \tag{9.1}$$

where k_∞ and k_0 are, respectively, the stiffness of the system at the perfectly rigid and perfectly compliant limits. From the plot of the maximum loss factor as a function of Y in Fig. 2.3, we see that to obtain a loss factor of, say, five per cent, we need to have a stiffness ratio of at least three tenths.

A notable exception to this rule occurs when the inertia of the damping treatment leads to something of a tuned-mass effect as can occur in the vibration of elastic-viscoelastic beams in the plane of lamination. When the damping treatment is itself resonant, we can no longer simply write an equivalent stiffness for the system but must actually solve the complex eigenvalue problem.

9.2 Future Work

Though we have performed a number of experiments to guide in the development and verification of the models presented in this thesis, We have not yet fabricated "from the ground up" a machine which uses the new methods developed in this thesis. This work is underway at present.

For the damping techniques developed in this thesis to find wide application in the equipment industry, the important results must be reduced to simple formulaeΦe or (at worst) software. We have succeeded in obtaining simple design formulae for important cases of torsion of thin-walled beams and longitudinal vibration of leadscrew drives. But so far we have (for most boundary conditions) required numerical methods to obtain solutions for beam flexure. Approximate solutions for flexure of damped beams would be of great utility.

In the course of this work, we have developed a finite-element code for analysis of threc-dimensional motion of framed structures incorporating viscoelastic laminae. Over the coming months, we hope to build a user interface for this software and make it available to the design community.

REFERENCES

Bishop, R. E. D., and Johnson, D. C., 1960, *The Mechanics of Vibration*, Cambridge University Press, London.

Book, W. J., 1993, "Controlled Motion in an Elastic World," *Journal of Dynamic Systems, Measurement, and Control*, Vol. 115, pp. 252–261.

Chandrasekharan, M. P., and Ghosh, A., 1974, "Damping Characteristics of Elastic-Viscoelastic Composite Shafts," *Journal of Sound and Vibration*, Vol. 37, No. 1, pp. 1–15.

Chen, Q., and Levy, C., 1996, "Vibration Characteristics of Partially Covered Double-Sandwich Beam," *AIAA Journal*, Vol. 34, No. 12, pp. 2622–2626.

Chen, Y., and Tlusty, J., 1995, "Effect of Low-Friction Guideways and Leadscrew Flexibility on Dynamics of High-Speed Machines," *Annals of the CIRP*, Vol. 44, pp. 353–356.

Courant, R., and Hilbert, D., 1953, *Methods of Mathematical Physics*, Volume I, Wiley Interscience, New York.

Crandall, S. H., 1991, "The Hysteretic Damping Model in Vibration Theory," *Journal of Mechanical Engineering Science*, Vol. 25, pp. 23–28.

Crawley, E. F., Sigler, J. L., and van Schoor, M. C., 1988, *Prediction and Measurement of Damping in Hybrid Scaled Space Structure Models*, Space Systems Laboratory, Departement of Aeronautics and Astronautics, Massachusetts Institute of Technology.

Dewa, H., 1989, "Torsional Stress Analysis and Vibration Damping of Three-Layered Rods," *JSME International Journal*, Series I, Vol. 33, No. 2, pp. 152–159.

DiTarantino, R. A., 1965, "Theory of Vibratory Bending for Elastic and

Viscoelastic Layered Finite-Length Beams," *Journal of Applied Mechanics*, Vol. 87, pp. 881–886.

Douglas, B. E., and Yang, J. C. S., 1978, "Transverse Compressional Damping in the Vibratory Response of Elastic-Viscoelastic-Elastic Beams," *AIAA Journal*, Vol. 16, No. 9, pp. 925–930.

Haftka, R. T., Gurdal, Z., and Kamat, M. P., 1990, *Elements of Structural Optimization*, Kluwer, Boston.

Haug, E. J., Choi, K. K., and Komkov, V., 1986, *Design Sensitivity Analysis of Structural Systems*, Academic Press, Orlando.

Ibrahim, R. A., 1987, "Structural Dynamics with Parameter Uncertainties," *ASME Applied Mechanics Reviews*, Vol. 40, No. 3, pp. 309–328.

Imregun, M., and Visser, W. J., 1989, "A Review of Model Updating Techniques," *Proceedings of the International Seminar on Modal Analysis.*

Johnson, A. F., and Woolf, A., 1976, "Dynamic Torsion of a Two-Layer Viscoelastic Beam," *Journal of Sound and Vibration*, Vol. 48, No. 2, pp. 251–263.

Kerwin, E. M., 1959, "Damping of Flexural Waves by a Constrained Viscoelastic Layer," *Journal of the Acoustical Society of America*, Vol. 31, No. 7, pp. 952–962.

Koenigsberger, F., and Tlusty, J., 1970, *Machine Tool Structures*, Pergammon Press, London.

Kollbrunner, C. F., and Basler, K., 1969, *Torsion in Structures*, Springer-Verlag, New York.

Lazan, B. J., 1968, *Damping of Materials and Members in Structural Mechanics*, Pergammon Press, London.

Lowenfeld, K., 1959, "Zusatzdämpfung von Werkzeugmaschinen durch Lamellenpakete," *Maschinenmarkt*, No. 19.

Markus, S., and Valaskova, O., 1972, "On Eigenvalue Problems Boundary Problems of Transversely Vibrating Sandwich Beams," *Journal of Sound and Vibration*, Vol. 23, pp. 423–432.

Marsh, E. R., and Slocum, A. H., 1996, "An Integrated Approach to Structural Damping," *Precision Engineering*, Vol. 18, No. 3, pp. 103–109.

Marsh, E. R., and Hale, L. M., 1997, "Damping of Flexural Waves with Embedded Viscoelastic Materials," *Journal of Vibration and Control*, accepted for publication.

Mead, D. J., and Markus, S., 1969, "The Forced Vibration of a Three-Layer, Damped Sandwich Beam with Arbitrary Boundary Conditions," *Journal of*

Sound and Vibration, Vol. 10, No. 2, pp. 163–175.

Nanda Kishore, N., and Gosh, A., 1975, "Damping Characteristics of Elastic-Viscoelastic Composite Curved Bars and Helical Springs," *Journal of Sound and Vibration*, Vol. 43, No. 4, pp. 621–632.

Olhoff, N., 1989, "Optimal Design of Conservative Mechanical Systems," *Structural Optimization Under Stability and Vibration Constraints*, Zyczkowski, M., ed., Springer–Verlag, New York.

Oravsky, V., Markus, S., and Simkova, O., 1974, "A New Approximate Method of Finding the Loss Factors of a Sandwich Cantilever," *Journal of Sound and Vibration*, Vol. 33, No. 3, pp. 335–352.

Pierre, C., 1987, "Eigensolution Perturbation for Systems with Perturbed Boundary Conditions," *Journal of Sound and Vibration*, Vol. 112, No. 1, pp. 167–172.

Plass, H. J., Jr., 1957, "Damping Vibrations in Elastic Rods and Sandwich Structures by Incorporation of Additional Viscoelastic Material," *Proceedings of the Third Midwestern Conference on Solid Mechanics*, pp. 48–71.

Plunkett, R., and Lee, C. T., 1970, "Length Optimization for Constrained Viscoelastic Layer Damping," *Journal of the Acoustical Society of America*, Vol. 48, No. 1, pp. 150–161.

Rao, D. K., 1977, "Vibration of Short Sandwich Beams," *Journal of Sound and Vibration*, Vol. 52, No. 2, pp. 253–263.

Rao, D. K., 1978, "Frequency and Loss Factors of Sandwich Beams Under Various Boundary Conditions," *Journal of Mechanical Engineering Science*, Vol. 20, No. 5, pp. 271–282.

Rao, M. D., and He, S., 1993, "Dynamic Analysis and Design of Laminated Composite Beams with Multiple Damping Layers," *AIAA Journal*, Vol. 31, No. 4, pp. 736–745.

Rellich, F., 1969, *Perturbation Theory of Eigenvalue Problems*, Gordon and Breach, New York.

Ross, D., Ungar, E., and Kerwin, E. M., 1959, "Damping of Plate Flexural Vibrations by Means of Viscoelastic Laminae," *Structural Damping*, ed. by Ruzicka, J. E., ASME, New York.

Ruzicka, J. E., 1961, "Damping Structural Resonances Using Viscoelastic Shear-Damping Mechanisms," *Journal of Engineering for Industry*, Series B, Vol. 83, No. 4, pp. 414–424.

Sokolnikoff, I. S., 1956, *Mathematical Theory of Elasticity*, McGraw-Hill, New York.

Thomson, W. T., 1988, *Theory of Vibration with Applications, Third Edition*, Prentice Hall, New Jersey.

Timoshenko, S. P., and Goodier, J. N., 1970, *Theory of Elasticity*, Third Edition, McGraw-Hill, New York.

Torvik, P. J., 1980, "The Analysis and Design of Constrained Layer Damping Treatments," *Damping Applications for Vibration Control*, AMD-Vol. 38, ASME.

Trompette, F., Boillot, D., and Ravanel, M. A., "The Effect of Boundary Conditions on the Vibration of Viscoelastically Damped Cantilever Beam," *Journal of Sound and Vibration*, Vol. 60, No. 3, pp. 345–350.

Yang, R. J., and Botkin, M. E., 1986, "The Relationship Between the Variational Approach and the Implicit Differentiation Approach to Shape Design Sensitivities," *The Optimum Shape*, General Motors Symposium, Plenum Press.

Zapfe, J. A., and Lesieutre, G. A., 1996, "Broadband Vibration Damping in Beams Using Distributed Viscoelastic Tuned Mass Absorbers," AIAA paper 96-1595.